

CMUT ARRAY DESIGN AND FABRICATION FOR HIGH FREQUENCY ULTRASOUND IMAGING

A Dissertation
Presented to
The Academic Faculty

by

Evren Fatih Arkan

In Partial Fulfillment
of the Requirements for the Degree
Doctor of Philosophy in the
School of Mechanical Engineering

Georgia Institute of Technology
May 2020

COPYRIGHT © 2020 BY EVREN ARKAN

CMUT ARRAY DESIGN AND FABRICATION FOR HIGH FREQUENCY ULTRASOUND IMAGING

Approved by:

Dr. F. Levent Degertekin, Advisor
School of Mechanical Engineering
Georgia Institute of Technology

Dr. Costas D. Arvanitis
School of Mechanical Engineering
Georgia Institute of Technology

Dr. Karim Sabra
School of Mechanical Engineering
Georgia Institute of Technology

Dr. Brooks Lindsey
School of Biomedical Engineering
Georgia Institute of Technology

Dr. Peter Hesketh
School of Mechanical Engineering
Georgia Institute of Technology

Date Approved: [March 13, 2020]

*Bu tezi ömrüm boyunca benden desteđini, teşviđini, ve sevgisini esirgemeyen canım
aileme ithaf ediyorum.*

*Dedicated to my family for their never-ending encouragement, love, and support
throughout my life.*

ACKNOWLEDGEMENTS

I wish to thank my advisor Dr. Levent Degertekin for his support and guidance throughout my research. I am especially grateful for his considerate and understanding attitude which helped me traverse this arduous academic journey. I would also like to thank my committee members Dr. Costas Arvanitis, Dr. Peter Hesketh, Dr. Karim Sabra, and Dr. Brooks Lindsey for taking the time and effort to serve on my defense committee.

This work was made possible through the financial support of the Fulbright Scholar Program and National Institute of Health (NIH). I would particularly like to thank the Fulbright Scholar Program for not only starting this incredible chapter of my life but enriching it with multitude of amazing people and enlightening and entertaining events.

This dissertation is the result of years of collaborative teamwork of former and present members of Dr. Degertekin's Micromachined Sensors & Transducers group and the GT-Bionics lab and would not have otherwise been possible. I would like to thank Dr. Coskun Tekes, Dr. Sarp Satir, Dr. Jaime Zahorian, Dr. Toby Xu, Dr. Amirabbas Pirouz, Dr. Shane Lani, Dr. Bernie Shieh, Dr. Muhammad Wasequr Rashid, Dr. Serife Tol, Dr. David Torello, Dr. Gwangrok Jung, Dr. Jaemyung Lim, Yusuf Samet Yaras, Sushruta Surappa, Sait Kilinc, Ahmad Rezvanitabar, Dylan Fife, Charles Wei, and Brian Chen for their aid in simulation, fabrication, testing, image processing and overall making my time in Georgia Tech significantly more pleasant and enjoyable. I would also like to thank the IEN and clean room staff for their processing support and dedication to running a world class research cleanroom facility, which has enabled numerous novel research including this one.

Finally, I would like to thank my parents, my sister, my brother-in-law and the many intelligent and interesting people I am proud to call my friends for their unconditional support and encouragement. You have helped me through my hardest times, and I cannot express my gratitude enough for all of you.

TABLE OF CONTENTS

	Page
ACKNOWLEDGEMENTS.....	iv
LIST OF TABLES.....	xi
LIST OF FIGURES.....	xii
LIST OF SYMBOLS AND ABBREVIATIONS.....	xix
SUMMARY.....	xxiv
CHAPTER 1. BACKGROUND AND MOTIVATION.....	1
1.1. High Frequency Ultrasound Imaging.....	1
1.1.1. High Frequency Ultrasound Applications.....	3
1.1.2. Array vs Single Element Imaging.....	4
1.1.3. High Frequency Imaging and Array Requirements.....	6
1.2. Piezoelectric vs CMUT High Frequency Arrays.....	7
1.2.1. Transducer Operation Comparison.....	7
1.2.2. Array Fabrication Comparison.....	12
1.2.3. Electronics Integration Comparison.....	17
1.3. High Frequency CMUT Arrays in Literature.....	21
1.4. Objectives of This Work.....	21
CHAPTER 2. CMUT MODELING AND ANALYSIS FRAMEWORK.....	23
2.1. CMUT Modeling.....	23
2.1.1. Parallel Plate Modeling.....	23

2.1.2. Small Signal Analysis	26
2.1.3. Finite Element Modeling	29
2.1.4. Nonlinear Lumped Large Signal CMUT Model.....	30
2.2. Analysis Methodology	42
2.2.1. Receiver Analysis Methodology.....	42
2.2.2. Transmitter Analysis Methodology	46
2.2.3. Pulse-Echo Analysis Methodology.....	47
2.3. Case Study: Guidewire IVUS Array.....	47
2.3.1. Guidewire IVUS System.....	48
2.3.2. Design Constraints	49
2.3.3. Receiver Analysis: Guidewire IVUS Array.....	51
2.3.4. Pulse-Echo Analysis: Guidewire IVUS Array.....	58
2.3.5. Transmitter Analysis: Guidewire IVUS Array	64
2.3.6. Fill Factor Analysis: Guidewire IVUS Array	68
2.4. Conclusion	72
CHAPTER 3. FREQUENCY RESPONSE LIMITING MECHANISMS AND DESIGN PROCESS.....	74
3.1. Frequency Limiting Factors	75
3.1.1. Bragg Scattering.....	75
3.1.2. Crosstalk Induced Array Modes	76

3.2.	Operation Frequency Band	76
3.2.1.	Impact of Membrane Thickness.....	78
3.2.2.	Impact of Membrane Aspect Ratio	80
3.2.3.	Impact of Membrane Shape and Array Lattice.....	81
3.3.	High Frequency CMUT Array Design Strategy	84
3.3.1.	Design Process Algorithm	86
3.3.2.	Design Process Example.....	88
3.3.3.	Design Process Limitations.....	89
3.3.4.	Design Strategy Extension to Broader Frequency Range.....	91
3.4.	Case Study: Passive Acoustic Imaging Array	93
3.4.1.	Design Constraints	95
3.4.2.	Array Design.....	95
CHAPTER 4. DEVICE FABRICATION AND EXPERIMENTAL VALIDATION.		98
4.1.	Arrays Limited by Single Membrane Dynamics	99
4.1.1.	Low Frequency CMUT Array Fabrication	101
4.2.	Arrays Limited by Bragg Scattering.....	105
4.2.1.	High Frequency CMUT Array Fabrication.....	106
4.3.	Experimental Validation	111
4.3.1.	Pressure Measurements.....	111
4.3.2.	Admittance Measurements.....	113

4.3.3.	Water vs FC-70	115
4.4.	Integrated Guidewire IVUS Imaging System	117
4.4.1.	Ultrasound Imaging System Characterization	118
4.4.2.	System Imaging Measurement.....	121
CHAPTER 5.	RECEIVER ELECTRONICS INTEGRATION ANALYSIS	123
5.1.	Receive Mode Termination Schemes	124
5.1.1.	Power Matching	124
5.1.2.	Acoustic Matching	125
5.2.	Impedance Matching Schemes	126
5.3.	Analysis Methodology	129
5.4.	Case Study: 1D ICE Array.....	130
5.4.1.	Power Transfer and Reflectivity Analysis	134
CHAPTER 6.	CONCLUSIONS AND FUTURE WORK	137
6.1.	Conclusions.....	137
6.2.	Contributions.....	137
6.2.1.	Frequency Band Limitations and Design Methodology	137
6.2.2.	Experimental Validation and Imaging System Construction.....	138
6.2.3.	Receiver Electronics Analysis	138
6.3.	Future Work	139
APPENDIX A.	SAMPLE MATLAB CODES FOR RECEIVER ANALYSIS.....	141

A.1.	Impedance and Thermal Mechanical Current Noise Calculation	141
A.2.	Plane Wave Pressure Sensitivity and Transformer Ratio Calculation....	142
A.3.	Pressure Noise Spectrum Calculation.....	145
A.4.	Ideal Piston Radiation Impedance Calculation.....	146
A.5.	Ideal Piston Pressure Noise Spectrum Calculation.....	147
APPENDIX B. BATCH SIMULATION OF THE NONLINEAR LUMPED LARGE SIGNAL CMUT MODEL		148
REFERENCES		159

LIST OF TABLES

	Page
Table 2.1. Analyzed CMUT membrane geometries.	51
Table 2.2. Characteristic of reflection currents and pulse-echo SNR of different membrane geometries in water	60
Table 2.3. Characteristic of reflection currents and pulse-echo SNR of different membrane geometries in blood.....	62
Table 2.4. Characteristics of reflection currents and pulse-echo SNR of 10 μm membrane geometry under different operation voltages	63
Table 2.5. Characteristics of reflection currents and pulse-echo SNR of 15 μm membrane geometry under different operation voltages	64
Table 2.6. Characteristics of reflection currents and pulse-echo SNR of 20 μm membrane geometry under different operation voltages	64
Table 2.7. Analyzed CMUT membrane geometries	69
Table 2.8. Characteristic of reflection currents and pulse-echo SNR of 10 μm arrays of constant element pitch and varying FF	71
Table 2.9. Characteristic of reflection currents and pulse-echo SNR of 10 μm arrays of varying element pitch and varying FF	72
Table 3.1. Characteristic of reflection currents and pulse-echo SNR of additional simulated arrays of varying element pitch and varying FF	85
Table 3.2. Analyzed CMUT membrane geometries.	96
Table 4.1. f_{ares} limited array properties and limiting factor frequencies.....	100
Table 4.2. f_{Bragg} limited array properties and limiting factor frequencies	105
Table 4.3. f_{Bragg} limited limiting factor frequencies in FC-70.....	116

LIST OF FIGURES

	Page
Figure 1.1: Illustration of (a) axial and (b) lateral resolution.	2
Figure 1.2: Bulk piezoelectric transducer operation.	8
Figure 1.3: CMUT transducer operation.	9
Figure 1.4: Bulk piezoelectric device fabrication using the dice-and-fill technique [29].	13
Figure 1.5: Process flow for a wafer-bonded CMUT. (a) Starting prime wafer. (b) Thermal oxidation. (c) Etch to form cavity. (d) Thermal oxidation. (e) Silicon on insulator (SOI) wafer bonding. (f) SOI handle. (g) Removing buried oxide. (h) Sputtering metallization. (i) Metal pattern and device isolation. [36].....	14
Figure 1.6: Process flow for CMUT fabrication with sacrificial release. (a) Sacrificial polysilicon deposition and patterning on silicon nitride deposited wafer. (b) Sacrificial polysilicon deposition for etch channels into the cells. (c) Silicon nitride top plate layer deposition and patterning. (d) Sacrificial polysilicon layer etching. (e) Silicon nitride deposition to seal the cells. (f) Aluminum deposition and patterning for electrodes and interconnects. [36].....	16
Figure 1.7: Cross section of CMOS integrated bulk piezoelectric ICE device [39].	18
Figure 1.8: Flip-chip bonded volumetric CMUT array. a) Top view of individual element. b) Close-up to CMUT cells. c) Cross section of flip-chip bonded device. d) Close-up of the through wafer via. [36].....	19
Figure 1.9: a) Micrograph of CMOS circuitry before (left) and after (right) monolithic integration of CMUT arrays [50]. b) Cross sectional schematic of the interconnections between monolithically integrated CMUT and CMOS [53].....	20
Figure 2.1: Parallel plate mass-spring-damper CMUT model. [36]	24
Figure 2.2: Mason equivalent circuit for linearized parallel plate CMUT.	28

Figure 2.3: Calculated and measured electromechanical coupling factor of a CMUT as a function of V_{DC} normalized to V_{col} [61].	29
Figure 2.4: Block diagram of model developed by Satir and Degertekin [63].	31
Figure 2.5: A CMUT membrane meshed into 5×5 matrix of nodes, $N=25$, with corresponding areas $d_x \times d_y$ [64].	32
Figure 2.6: SIMULINK block diagram with input vector of voltage signals applied to array electrode patches and output force vector [64].	36
Figure 2.7: Comparison of pressure field simulated with models developed by (a) Boulme <i>et al</i> [65] and Satir [62].	37
Figure 2.8: Pulse-echo operation.	38
Figure 2.9: Geometry used for derivation of the modified fluid loading component of force balance equation via method of images [66].	39
Figure 2.10: Electrical circuit for receive operation employing the CMUT as a variable capacitor [66].	40
Figure 2.11: SIMULINK model with integrated receiver electronics [66].	41
Figure 2.12: SIMULINK model with integrated transmitter and receiver electronics [66].	41
Figure 2.13: Impedance calculation through transient simulation.	43
Figure 2.14: Conceptual schematic of the guidewire IVUS system.	48
Figure 2.15: Schematic of full cross section image formation from four sectors obtained from the four 1D CMUT arrays [55].	49
Figure 2.16: 2D representation of CMUT array. Cross section of a single membrane is seen in the inset.	50
Figure 2.17: V_{DC} effect as percentage of V_{col} on current noise (I_{noise}), pressure sensitivity (PS) and pressure noise spectrum (p_{min}) of $20 \mu\text{m}$ membrane array elements.	52
Figure 2.18: Gap thickness (g) effect on current noise (I_{noise}), pressure sensitivity (PS) and pressure noise spectrum (p_{min}) of $20 \mu\text{m}$ membrane array elements.	53

Figure 2.19: a) Current noise (I_{noise}) and b) pressure sensitivity (PS) spectra of SEs (dashed line) and imaging AEs (solid line) of different membrane geometries.	56
Figure 2.20: Pressure noise spectrum (p_{min}) of single elements (SE) and array elements (AE) with different membrane geometries.	58
Figure 2.21: Membrane geometry effect on the reflection current of imaging AEs.....	61
Figure 2.22: Membrane geometry effect on the reflection current of imaging AEs.....	63
Figure 2.23: Beam pattern of array elements with different membrane geometries	65
Figure 2.24: Comparison of single element actuation and beam focused pressure output for a) 10, b) 15, and c) 20 μm arrays	66
Figure 2.25: Narrowing of pressure output bandwidth with increasing angle. The angle dependent f_{Bragg} is plotted as dashed line	68
Figure 2.26: Receiver characteristics of single elements (SE) and array elements (AE) of different fill factors (FF)	70
Figure 2.27: Fill factor (FF) effect on reflection current of 10 μm membrane array elements	71
Figure 3.1: Normalized frequency response comparison of individual membranes and arrays of 600 and 800 nm thickness. Zoomed in sections of the pressure output -3 dB frequency span are visible on the right. The light shaded area illustrates operation band estimation and the dark shaded area illustrates -3dB frequency band of the pressure output.	78
Figure 3.2: Frequency limits of 15 μm square membrane array geometries of varying thickness. The light shaded area illustrates operation band estimation for array geometries of 70% FF and the dark shaded area illustrates -3dB frequency band of the same array geometries of 250 μm x 250 μm size.....	79
Figure 3.3: Pressure output characteristics of 250 μm x 250 μm sized 15 μm square membrane array geometries of varying thickness.	80

Figure 3.4: Frequency limits of square membrane array geometries of varying width and aspect ratio. The colored arrows denote the single membrane limiting frequencies and their band for different aspect ratios. The black arrow denotes the f_{Bragg}	81
Figure 3.5: Frequency limits for a) square, and b) circular membranes of varying width. The shaded area illustrates operation band estimation for array geometries of 70% FF . An example of array geometries can be seen in the inset.	83
Figure 3.6: -6-dB frequency span (BW) relation with f_{Bragg_ave}	85
Figure 3.7: Design algorithm for 1D high frequency imaging array of $f_{center} = 60$ MHz and $FBW = 50\%$	87
Figure 3.8: Reflection current of imaging array element determined from the design process.....	88
Figure 3.9: Pulse-echo characteristics of f_{Bragg} and f_{ares} limited arrays. The element pitch varies between 15.6 μm and 25 μm and SNR is normalized to element area.....	90
Figure 3.10: -3dB frequency span (BW) relation with $(f_{high} - f_{low})$	91
Figure 3.11: Dual HIFU transducer and diagnostic imaging array geometry [92]......	94
Figure 3.12: Power spectra of cavitation activity during two sonifications [93]......	95
Figure 3.13: a) Plane wave pressure sensitivity (PS) and b) pressure noise spectrum (p_{min}) of designed array elements	97
Figure 4.1: a) Cross section of a conventional surface micromachined CMUT with thin isolation layer over TE-BE overlap area. b) Cross section of CMUT with the extra layer of dielectric deposited over TE-BE overlap area.	101
Figure 4.2: Sacrificial layer patterning with a) wet etching and over etching and b) lift-off without over etching.	102
Figure 4.3: Schematic of fabrication process flow of f_{ares} limited CMUT arrays.....	104
Figure 4.4: Catastrophic peel-off of CMUT membrane due to thermal stress in hafnium oxide isolation layer.....	108
Figure 4.5: Schematic of fabrication process flow of f_{Bragg} limited CMUT arrays.....	110

Figure 4.6: Comparison of simulated and measured pressure signals of f_{ares} limited arrays in time domain.....	112
Figure 4.7: Comparison of simulated and measured pressure signals of f_{ares} limited arrays in frequency domain. The blue and red arrows denote the limiting frequencies of the crosstalk induced array modes and the black arrow denotes the dip in the frequency response due to wafer ringing	113
Figure 4.8: Comparison of simulated and measured conductance of 78 μm array. The colored arrows denote the limiting frequency of the crosstalk induced array modes and the black arrow denotes the limiting frequency due to Bragg scattering.....	114
Figure 4.9: Comparison of simulated and measured conductance of f_{Bragg} limited arrays of 36% and 49% FF in water. The colored arrows denote the frequencies of Bragg scattering and the black arrow denotes the frequency of the crosstalk induced array modes in the vicinity of f_{single}	115
Figure 4.10: Comparison of simulated and measured conductance of f_{Bragg} limited arrays of 36% and 49% FF in FC-70. The colored arrows denote the frequencies of Bragg scattering and the black arrow denotes the frequency of the crosstalk induced array modes in the vicinity of f_{single}	117
Figure 4.11: Micrograph of fabricated IVUS CMUT array [55]......	118
Figure 4.12: Measured f_{center} of each CMUT array element [55]......	118
Figure 4.13: Measurement setup for a) transmitter, b) receiver, and c) pulse-echo characterization of SoC [97].	119
Figure 4.14: Transient pulse-echo signal of pulse-echo characterization [97].	120
Figure 4.15: Transmitter, receiver and pulse-echo spectrums of the SoC [97].	121
Figure 4.16: Imaging test setup of the ultrasonic imaging system [97]......	121
Figure 4.17: Constructed image of metal wires with 35 dB grey scale dynamic range [97].	122

Figure 5.1: Conceptual view of a) impedance matching network at the interface of the CMUT and electronics, b) narrowband $R L$ impedance matching, and c) broadband $R - C$ impedance matching.	126
Figure 5.2: a) Analyzed CMUT array geometry. b) Analyzed CMUT array impedance.	127
Figure 5.3: Comparison of CMUT array impedance with a) $R L$ and b) $R - C$ matching receive circuitry.	128
Figure 5.4: Power reflection coefficient comparison of different terminations.....	129
Figure 5.5: Time domain multiple reflection output utilized in acoustic reflectivity analysis.....	130
Figure 5.6: a) Analyzed 1D CMUT array geometry. b) Output impedance of the center element of the designed CMUT array biased at 36 V and the equivalent $R C$ circuit. .	131
Figure 5.7: The simulated CMUT response at the presence of: (a) a SC with 0.1Ω termination, (b) an OC with $1 \text{ G}\Omega$ termination, (c) a narrowband matching circuit with $R L$ ($16\text{k}\Omega 45\mu\text{H}$) termination, and (d) a broadband matching circuit with $R - C$ ($87\text{k}\Omega - 7.31\text{pF}$) termination.	132
Figure 5.8: The simulated output acoustic pressure output of the CMUT for different terminations.....	133
Figure 5.9: Frequency spectrum of the CMUT voltage output for different terminations.	134
Figure 5.10: Normalized RMS power for different terminations vs. resistive load.	135
Figure 5.11: Acoustic reflectivity for different terminations vs. resistive load.	135
Figure 5.12: The overall SNR for different negative capacitances.....	136
Figure B.1: Transient CMUT array modeling flow chart. Different calculation domains are highlighted in different shading. Batch simulation can be conducted on blocks with red outline.	149

Figure B.2: Step-by-step run-through of the CMUT array modeling process with PACE clusters. 158

LIST OF SYMBOLS AND ABBREVIATIONS

List of Abbreviations

AE	Array Element
ALD	Atomic Layer Deposition
A-mode	Amplitude Mode
ASIC	Application-Specific Integrated Circuit
BE	Bottom Electrode
BEM	Boundary Element Model
B-mode	Brightness Mode
BOX	Buried Oxide
BW	Bandwidth
CHF ₃	Fluoroform
CMOS	Complementary Metal–Oxide–Semiconductor
CMP	Chemical-Mechanical Polishing
CMUT	Capacitive Micromachined Ultrasonic Transducer
CT	Computed Tomography
DC	Direct Current
DRIE	Deep Reactive Ion Etching
FBW	Fractional Bandwidth
FEA	Finite Element Analysis
FEM	Finite Element Method
FF	Fill Factor
FFR	Fractional Flow Reserve
FIR	Finite Impulse Response
HfO ₂	Hafnium Oxide
HIFU	High Intensity Focused Ultrasound
ICE	Intracardiac Echocardiography
IPA	Isopropyl Alcohol
IVPA	Intravascular Photoacoustic

IVUS	Intravascular Ultrasound
LDMOS	Laterally-Diffused Metal-Oxide-Semiconductor
LNA	Low-Noise Amplifier
LOCOS	Local Oxidation of Silicon
LPCVD	Low Pressure Silicon Nitride
MIMO	Multiple-Input Multiple-Output
MISO	Multiple-Input Single-Output
M-mode	Motion Mode
MRI	Magnetic Resonance Imaging
OC	Open circuit
PACE	Partnership for an Advanced Computing Environment
PECVD	Plasma Enhanced Chemical Vapor Deposition
PS	Plane Wave Pressure Sensitivity
PSD	Power Spectral Density
PVDF	Polyvinylidene Difluoride
PZT	Ferroelectric Lead Zirconate Titanate
RIE	Reactive Ion Etching
RMS	Root mean square
Rx	Receiver
SC	Short circuit
SE	Single Element
SF ₆	Sulfur Hexafluoride
SFTP	Secure File Transfer Protocol
SNR	Signal-to-Noise Ratio
SoC	System-on-a-Chip
SOI	Silicon on Insulator
SPL	Spatial Pulse Length
SSH	Secure Shell
TE	Top Electrode
TIA	Trans-Impedance Amplifier
Tx	Transmitter

List of Symbols

α	Attenuation Coefficient
c_0	Speed of Sound of Medium
ϵ_0	Permittivity of Vacuum
ϵ_r	Relative Permittivity
λ	Wavelength
ω	Angular Frequency
φ	Transformer Ratio
ρ	Density
ρ_0	Density of Medium
A	Area
a	Membrane Width
C	Capacitance
C_0	Capacitance at Operating Bias Voltage
C_{free}	Free Capacitance
C_p	Parasitic Capacitance
d	Membrane Pitch
d_{el}	Element Pitch
d_p	Periodic Spacing
d_x	Elevation Membrane Pitch
d_y	Azimuthal Membrane Pitch
E	Young's Modulus
E_{BD}	Dielectric Breakdown Strength
f	Focal Length
f_{ares}	Single Membrane Antiresonance
f_{Bragg}	Bragg's Resonance
f_{Bragg_ave}	Average Bragg's Resonance
f_{center}	Center Frequency
f_{high}	Higher Frequency Limit

f_{low}	Lower Frequency Limit
f_{single}	Single Membrane Resonance
F_{es}	Electrostatic Force
g	Gap Thickness
g_0	Initial Vacuum Gap Thickness
g_{eff}	Effective Gap Thickness
h	Membrane Thickness
h/a	Aspect Ratio
i	Current
i_{noise}	Current Noise
i_{TM_noise}	Thermal Mechanical Current Noise
Im	Imaginary
k	Boltzmann's Constant
k_T	Electromechanical Coupling Coefficient
Mag	Magnitude
P	Pressure
p_{min}	Pressure Noise Spectrum
Q	Charge
$R -C$	Negative Capacitance Based Impedance Matching
$R L$	Inductor Based Impedance Matching
Re	Real
s	Power Reflection Coefficient
S	Aperture Size
T	Temperature
t_{iso}	Isolation Thickness
V	Voltage
V_{AC}	Alternating Current Voltage
V_{col}	Collapse Voltage
V_{DC}	Direct Current Bias
V_{DS}	Drain-to-Source Voltage

x	Membrane Displacement
Y_{CMUT}	CMUT Element Admittance
Z_{CMUT}	CMUT Element Impedance
Z_L	Load Impedance
Z_r	Radiation Impedance
Z_R	Receiver Electronics Impedance
Z_S	Source Impedance

SUMMARY

High frequency ultrasound imaging is utilized in a broad range of applications from intravascular imaging to small animal imaging for preclinical studies. Capacitive micromachined ultrasonic transducers (CMUTs) possess multiple preferable characteristics for high frequency imaging systems, such as simpler fabrication methods, simpler integration to electronics, and greater variety of array geometries. Adequate performance and optimization of CMUT based systems require a comprehensive analysis of multiple design parameters. This research utilizes a nonlinear lumped model, capable of simulating the pressure output, electrical input-output, and echo response to a planar reflector of CMUT arrays with arbitrary membrane shape and array geometry, to determine the performance limitations of high frequency CMUT arrays and the effect of different design parameters on its performance. Receiver performance is analyzed through parameters extracted from simulations, namely, thermal mechanical current noise, plane wave pressure sensitivity, and pressure noise spectrum. Transmitter performance is analyzed through pressure output simulation, and the overall performance is analyzed through the simulated pulse-echo response from a perfect planar reflector and the thermal mechanical current noise limited SNR. It is observed that the frequency response is dominated by two vibroacoustic limiting mechanisms: Bragg's scattering, determined by array lateral dimensions, and crosstalk actuated fundamental and antisymmetric array modes, determined by individual membrane dynamics. Based on the limiting mechanism frequencies, a simplified design methodology is developed and used to design two CMUT array sets covering 1-80MHz frequency range. These CMUT arrays are fabricated and their

limiting mechanisms are experimentally verified through pressure and admittance measurement and simulation comparison. CMUT arrays for guidewire IVUS application are implemented and successfully interfaced with ASICs to demonstrate imaging at 40MHz. Considering that CMUT array performance is also susceptible to the electrical termination conditions, the simulation model is utilized to investigate the effect of different impedance matching scenarios. Receiver performance of the integrated CMUT array and termination circuitry is analyzed through the system's SNR and acoustic reflectivity.

CHAPTER 1. BACKGROUND AND MOTIVATION

1.1. High Frequency Ultrasound Imaging

Beginning with the first transcranial image developed by Dr. Karl Dussik in 1942, ultrasound imaging has emerged into a staple in medical diagnostics [1]. The prevalence of ultrasound imaging in medicine can be attributed to multiple reasons. Ultrasound imaging systems are comparatively low cost, efficient and safe. In addition to these aspects, ultrasound imaging systems can utilize characteristics that cannot be supported by other imaging modalities. One such characteristic is related to the feasible resolution of the image. Other conventional imaging modalities, such as computed tomography (CT) and magnetic resonance imaging (MRI), have a constant spatial resolution in the order of millimeters, whereas ultrasound imaging has a spatially variant resolution. This enables ultrasound imaging with microscopic spatial resolution.

The resolution of an ultrasound imaging system is dependent on the size of the active aperture of the transducer, the center frequency (f_{center}) and bandwidth (BW). The axial spatial resolution, which determines the ability to resolve discrete structures along the beam axis, is determined by the spatial pulse length (SPL). The SPL of a transducer defines the space occupied by the pulse, and is inversely proportional to f_{center} and BW , as seen in Figure 1.1. As a result, axial resolution improves with higher f_{center} and BW . The lateral spatial resolution, which determines the ability to resolve discrete structures perpendicular to the beam axis, is determined by the beam width at the focal length. The beam width of a transducer is directly proportional to the focal length (f) and wavelength (λ), and

inversely proportional to the aperture size (S), as seen in Figure 1.1. Resultantly, lateral resolution improves with higher f_{center} and S , and lower f .

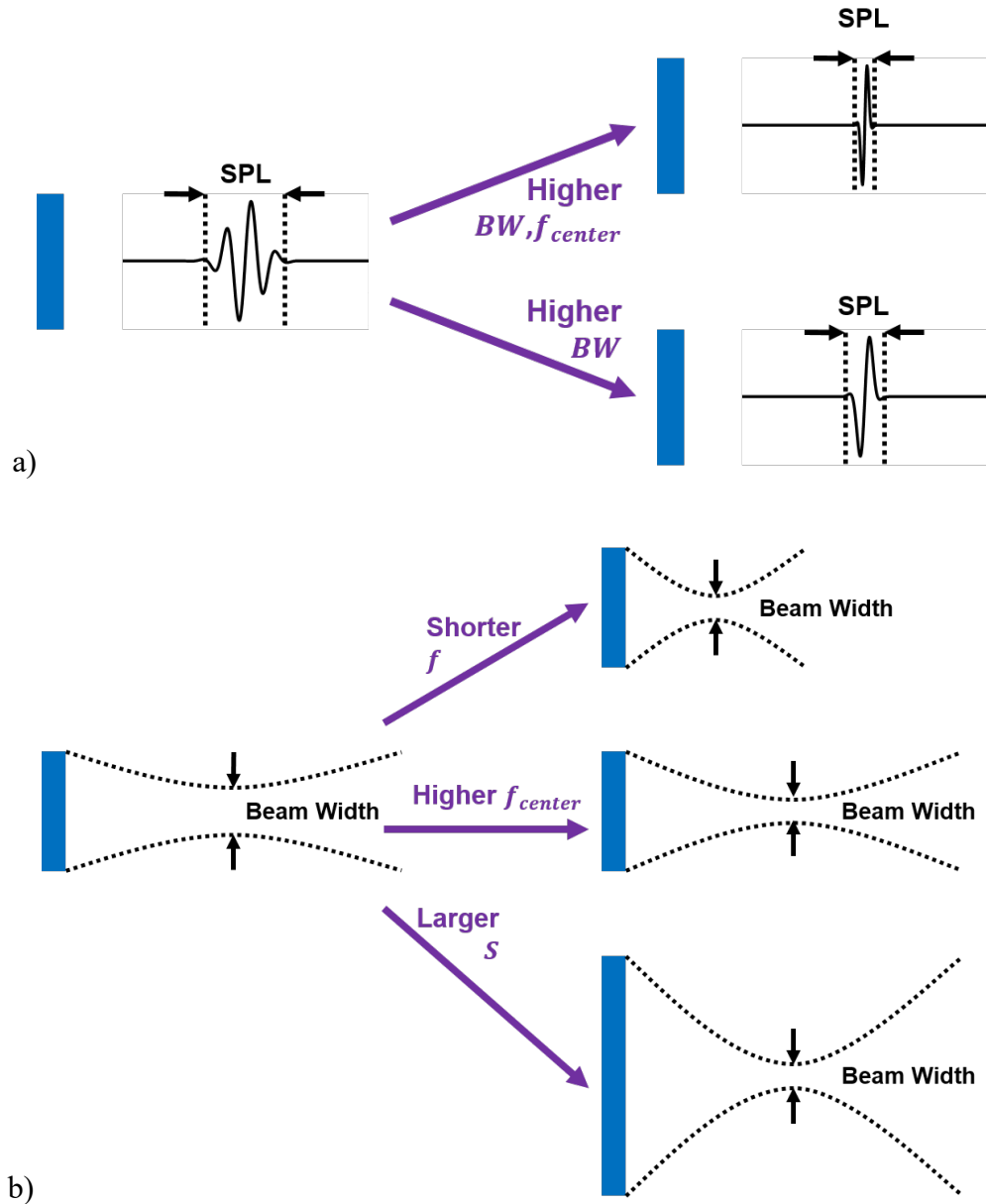


Figure 1.1: Illustration of (a) axial and (b) lateral resolution.

An additional factor affecting the resolution is acoustic attenuation. Acoustic attenuation manifests itself as exponential decay in amplitude, which can be formulated as:

$$P(x + \Delta x) = P(x)e^{-\alpha(\omega)\Delta x} \quad (1.1)$$

$$\alpha(\omega) = \alpha_0\omega^\eta \quad (1.2)$$

where ω is the angular frequency, P is the pressure, Δx the wave propagation distance, $\alpha(\omega)$ the attenuation coefficient, α_0 and frequency dependent η are real non-negative material properties. The frequency dependent attenuation of pressure waves limits the amount of energy that can be propagated and lowers the center frequency of the signals, effectively limiting penetration and reducing resolution. As the amount of attenuation increases with f_{center} , there exists a tradeoff between depth of field and resolution. Therefore, microscopic resolution with ultrasound imaging is feasible for small depth of field with high f_{center} . Correspondingly, the term “High Frequency Ultrasound Imaging” is used for such imaging processes.

1.1.1. High Frequency Ultrasound Applications

There are a number of clinical problems that require microscopic resolution and have a small depth of field. Ophthalmology and dermatology both require imaging of thin tissue layers, in which the structures of critical importance are relatively small and located in a few millimeters depth. The microscopic resolution supplied by high frequency ultrasound devices make them ideal for imaging anterior and posterior tissues of the eye in ophthalmology [2-4] and skin layers and tumors in dermatology [5-7].

A common disease that requires high resolution in small depth of field is atherosclerosis, in which the inside of an artery narrows due to plaque build-up. Rupturing

of these plaques may lead to total blockage of blood flow, resulting in a heart attack. High frequency ultrasound devices integrated to catheter probes enable atherosclerotic plaque characterization and guidance of stents for coronary intervention through intravascular ultrasound (IVUS) imaging [8-10], with commercial devices operating in frequencies above 30 MHz available. IVUS imaging systems can be further enhanced by integration of intravascular photoacoustic (IVPA) imaging systems [11-13], in which a low energy short laser pulse is emitted and the photoacoustic waves generated by the tissue is received. IVPA imaging is especially useful in determining the chemical composition of the tissue, allowing more acute characterization [14].

Another application that require similar resolution and depth of field is small animal imaging. Small animal models are an integral part of studying human diseases, such as cancer and cardiovascular disorders, along with pharmaceutical agent testing. In comparison to postmortem analysis, noninvasive imaging methods enable longitudinal analysis on the animal in an elegant and cost effective manner [15]. High frequency ultrasound devices allow high resolution *in vivo* imaging which can be further coupled with Doppler ultrasonography and subharmonic imaging, with commercial probes operating up to 70 MHz available [16-18].

1.1.2. Array vs Single Element Imaging

Medical ultrasonic imaging can be carried out in several modes. A single transducer can be used to obtain a 1-D analysis of the echoes generated from the discontinuities along the beam axis, defined as amplitude mode (A-mode) imaging. A-mode imaging procedure can then be repeated on an axis perpendicular to the beam axis to obtain a 2D analysis of a

plane through the body, defined as brightness mode (B-mode) imaging. Similarly, if the A-mode imaging procedure is repeated across a plane perpendicular to the beam axis, 3D B-mode images can be constructed. A section of the 3D B-Mode image can be then extracted to obtain a 2D analysis of a plane perpendicular to the 2D B-mode image, defined as C-mode image. If the previous imaging procedures are done in quick succession, the movement of the reflections can be analyzed, forming motion mode (M-mode) imaging.

The most common form of ultrasound imaging is the B-Mode imaging. B-mode images can be obtained by either mechanically scanning a single ultrasonic element, or by electronically scanning ultrasonic elements arranged in an array that is fixed in space. By eliminating the mechanical motion, array based systems can supply increased frame rate, reliability, and resolution. In addition to these benefits, array-based systems allow imaging methods unattainable with a single element system. Array-based systems are capable of dynamic focusing, which allows ultrasound beams to be electronically focused at different depths by controlling the strength and delay of the transmitted pressure pulse from each element of an array. Similarly, electronic control of each element allows focusing the beam at different angles, *i.e.* electronic beam steering. The ultrasonic beam can also be altered through aperture apodization, in which the active aperture of the array is changed by adjusting the number of active elements. These additional imaging methods allow array-based systems to supply increased signal-to-noise ratio (SNR), better lateral and axial resolution, and nearly perfect focusing throughout the scan depth, making them desirable for high frequency ultrasound imaging [19].

1.1.3. High Frequency Imaging and Array Requirements

Regarding the functionality and design of high frequency imaging systems, the two most important characteristics are depth of field and resolution. High frequency ultrasound imaging applications typically require a system that can differentiate between features in the order of 10-100 microns at a depth of couple millimeters. In ultrasonic imaging, reflections can only be generated if the acoustical wavelength of the pressure pulse is smaller than the feature. Therefore, to image features smaller than 100 μm , a center frequency higher than 30 MHz is required. Resolution of the imaging system improves as the operation frequency band is increased, but due to the increased attenuation, depth of field decreases. Therefore, any increase in operation frequency band has to be accompanied by improvement in transmitter (Tx) and/or receiver (Rx) characteristics of the system to ensure that SNR of echo signals generated at the desired depth of field is kept above the minimum required value. Obtaining sufficient depth of field can be especially difficult for applications that require small transducer area, such as IVUS imaging.

Additional consideration is required for array-based high frequency imaging systems. Array-based systems require the total transducer area to be populated by multiple elements at a certain pitch. The pitch between two array elements is determined by the operation frequency and must be smaller than half of the ultrasound wavelength to avoid grating lobes. The required pitch value for high frequency ultrasonic imaging arrays is therefore quite small, *e.g.* 25 μm for 30 MHz and 18.75 μm for 40 MHz operation. The small element size makes fabrication of such arrays difficult, and leads to a decrease in the Tx and Rx characteristics, reducing the obtainable depth of field. Furthermore, the presence

of multiple elements increases cross-coupling between resulting in a decrease in the operation frequency band.

1.2. Piezoelectric vs CMUT High Frequency Arrays

Multiple transducer types and transduction methods have been used to convert the acoustic pressure waves to electrical signals in ultrasonic imaging arrays. Considering high frequency imaging arrays, the two main transducer types that have been utilized are: bulk piezoelectric transducers and capacitive micromachined ultrasonic transducers (CMUTs). These two transducers differ from each other in multiple aspects, including transduction method, fabrication requirements, and system integration compatibility.

1.2.1. Transducer Operation Comparison

Bulk piezoelectric and CMUT devices have the same operation modus in medical ultrasonic imaging. Essentially, acoustic pressure waves cause the transducer to deform mechanically, which is then translated into electrical signals, and vice versa. The defining difference between the two devices is the transduction method between mechanical deformation and electrical signals. This difference in transduction methods is coupled with the acoustic domain, resulting in transducer operations with very different advantages and limitations.

Bulk piezoelectric devices utilize the piezoelectric effect as their transduction method. Piezoelectric effect is the ability to generate an electrical charge in response to applied mechanical stress observed in crystalline materials with no inversion symmetry. Each element in a bulk piezoelectric device is composed of a piezoelectric material

sandwiched between two electrodes, which is generally accompanied by matching layers. During device operation, acoustic pressure waves generate compression and tension on the piezoelectric material, resulting in an electric potential signal across the electrodes. An illustration of the transducer operation of bulk piezoelectric devices can be seen in Figure 1.2.

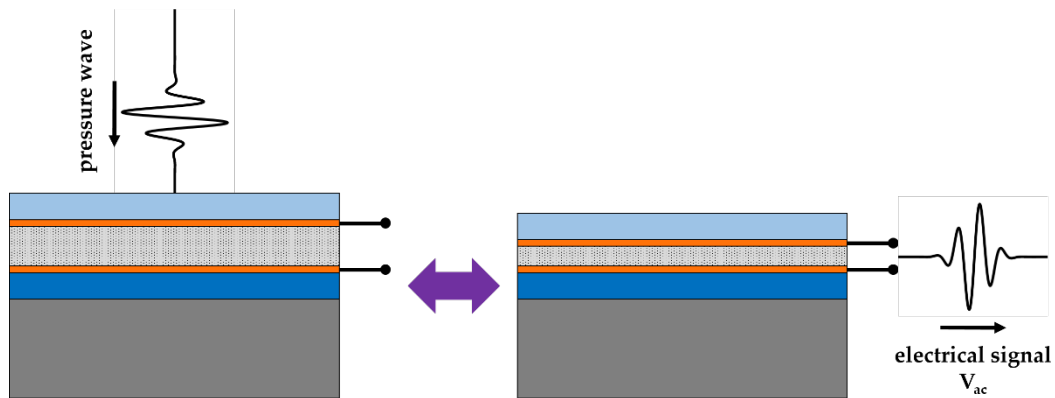


Figure 1.2: Bulk piezoelectric transducer operation.

CMUT devices operate using electrostatic transduction. Each element in a CMUT device is composed of multiple cells connected in parallel. These cells are comprised of a flexible top plate, a fixed bottom plate and a shallow vacuum gap in between these two plates. The plates are made electrically conductive by electrodes embedded within them, forming a variable capacitor with the vacuum gap. In CMUT device operation, acoustic pressure waves deform the flexible top plate, changing the vacuum gap height which result in a change in the capacitance of the element. By applying a direct current (DC) bias across the electrodes, the change in capacitance is converted into a change in charge, resulting in an electric current signal. An illustration of the transducer operation of CMUT devices can be seen in Figure 1.3.

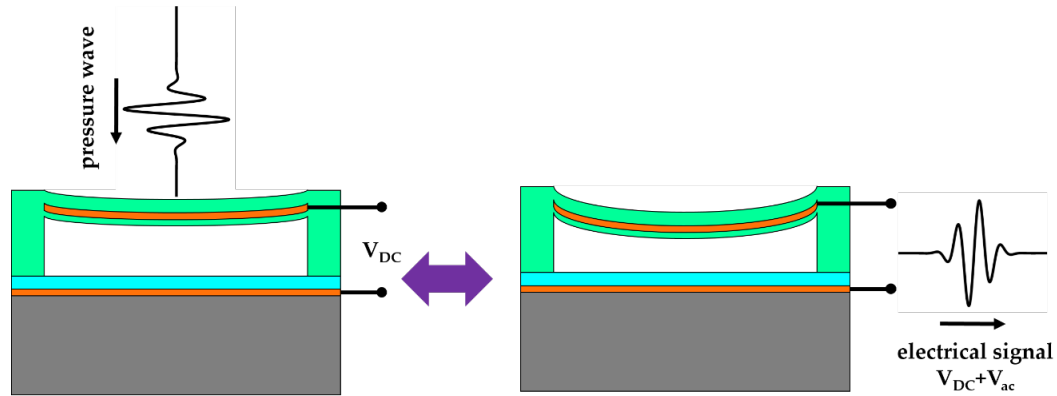


Figure 1.3: CMUT transducer operation.

The overall transduction effectiveness of an ultrasonic device is governed by two principal factors: the electromechanical coupling factor and the acoustic impedance mismatch. The electromechanical coupling factor defines how much of an input electrical energy is converted into mechanical energy, and the acoustic impedance mismatch defines how much of the mechanical energy of the transducer is transferred into the medium. An ideal ultrasonic device would demonstrate high electromechanical coupling factor and low acoustic mismatch, ensuring sufficient transduction between the three domains.

Electromechanical transduction is determined by piezoelectric equations in piezoelectric devices, resulting in an electromechanical coupling factor (k_T) dependent on the operating vibration mode and piezoelectric material constants, primarily the piezoelectric constant [20]. As a result, k_T of bulk piezoelectric devices is limited by the material properties, with most devices demonstrating k_T^2 below 50%. However, as electromechanical transduction is determined by change in charge in CMUT devices, k_T is dependent on the capacitance and the voltage across the electrodes and is not limited by its material properties. k_T^2 of a CMUT devices increases with the applied DC bias. However,

after a certain bias point, defined as collapse voltage, electrostatic forces on the CMUT cell cannot be balanced by the mechanical forces, resulting in the collapse of the top plate onto the bottom plate. As a result, standard CMUT operation is limited by the collapse voltage, with k_T^2 approaching 100% as the CMUT approaches collapse. However, CMUT operation past the collapse voltage, defined as collapse mode operation, is still possible [21-23]. In a CMUT cell in collapsed state, the top plate is only partially in contact with the bottom plate in its center, allowing electromechanical transduction from the edges. Operation in collapse mode can provide improvement in efficiency and bandwidth [24], but results in a large shift to higher operation frequency. This is especially relevant when the lateral dimensions of high frequency phased array elements are considered which need to be close to the half wavelength of operation frequency. Arrays operating in collapse-mode generally require larger membrane dimensions than arrays operating in conventional mode [25, 26]. Consequently, the membrane dimensions operated in collapse-mode in literature are generally above 25 μm , half wavelength at 30 MHz [27]. The constraint on membrane dimensions coupled with the thin membrane requirements may lead to prohibitively large voltages and reliability issues in collapsed mode.

Similar to electromechanical coupling factor, the acoustic impedance mismatch of a bulk piezoelectric devices is determined by its material properties, specifically its acoustic impedance. Most piezoelectric materials have significantly higher acoustic impedance than the medium, and therefore require additional acoustic passive materials as matching layers to increase the transmission efficiency. Ferroelectric lead zirconate titanate (PZT), currently the most commonly used piezoelectric ceramic in biomedical imaging has an acoustic impedance of $\sim 35 \text{ MRayl}$ which is approximately 23 times higher than the

acoustic impedance of tissue (~ 1.5 MRayl) [28]. Various piezoelectric materials with lower acoustic impedance have been developed to overcome the issue of the large acoustic mismatch. Polyvinylidene difluoride (PVDF), a commonly used piezo-polymer, has significantly lower acoustic impedance than PZT (~ 3.5 MRayl) but suffers from lower electromechanical coupling factor (~ 0.2) [28]. On the other hand, acoustic impedance mismatch is not an issue for CMUT device operation. Unlike bulk piezoelectric devices, acoustic waves are not generated within the transducer material, but rather via the continuity of motion between the flexible top plate and the fluid medium. As a result, CMUT devices have an acoustic impedance naturally matched to the medium and do not require additional matching layers to increase the transmission efficiency.

A frequency based analysis of the energy transmitted to the medium from the transducers can be carried out by approximating the transducers as mass-spring-damper systems. In its most elementary form, the mechanical domain of the transducer is modeled as mass-spring resonators and the acoustic domain is modeled as a mass and damper. Bulk piezoelectric transducers form a system of a single mass-spring-damper, in which the vibration is dominated by the density and mechanical stiffness of the piezoelectric material. This results in a narrowband operation frequency range around the resonance frequency of the transducer. The frequency range can be broadened by adding matching layers, which exhibits itself as increase in the damping of the system. In comparison, CMUTs form a system composed of a multitude of single mass-spring-dampers of very low mass, in which vibration is dominated by the mechanical stiffness of CMUT membrane and the mass of displaced fluid. As a result, CMUTs display a mechanical impedance naturally matched with the medium and an operation range not limited by the membrane resonance frequency.

This enables a broader design and fabrication space for CMUTs than bulk piezoelectric devices, especially for high frequency operation.

1.2.2. Array Fabrication Comparison

1.1.1.1 Piezoelectric Array Fabrication

Piezoelectric transducer elements are most commonly fabricated through dice-and-fill method, in which a bulk piezoelectric material undergoes a series of perpendicular parallel cuts using a mechanical dicing saw. The diced sample is then backfilled with a polymer and thinned down by polishing [29]. An illustration of the dice-and-fill method can be seen in Figure 1.4. This method allows simple and low-cost fabrication, but is limited in the size and geometry of the transducer elements that can be produced. Bulk piezoelectric devices operate in thickness mode, resulting in a resonance frequency inversely proportional to the material thickness. As a result, for high frequency operation the piezoelectric material must be thinned down to thickness values below 50 μm . The increased brittleness of the material at such thicknesses and the small pitch required for high frequency array operation, make mechanical dicing of the piezoelectric material a technical challenge. Piezoelectric arrays that overcome this limitation employ different fabrication methods such as deep reactive ion etching (DRIE) [30-32], partial dicing [33], laser micromachining [34], and kerfless arrays [35].

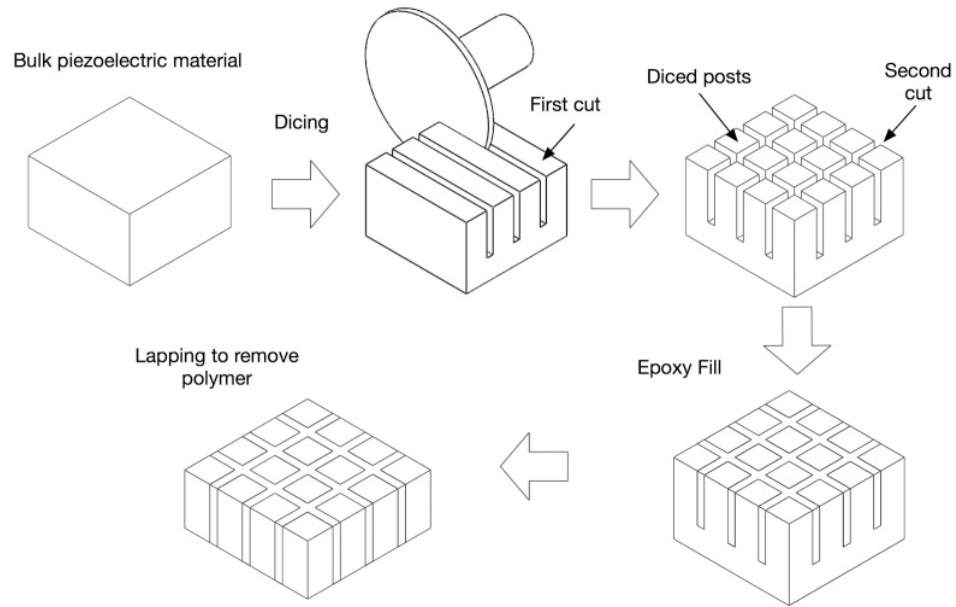


Figure 1.4: Bulk piezoelectric device fabrication using the dice-and-fill technique [29].

1.1.1.2 CMUT Array Fabrication

In comparison, CMUTs are fabricated using microfabrication techniques from the semiconductor industry, which allow for high yield batch fabrication of features of several micron size. As a result, CMUT fabrication technology can produce arrays with variable array geometries and small pitch sizes with relative ease. The two most commonly used CMUT fabrication techniques are wafer-bonding and sacrificial release.

The wafer bonding technique utilizes a combination of surface micromachining and silicon on insulator (SOI) technologies to fabricate the CMUTs. A sample fabrication process flow can be seen in Figure 1.5 [36]. Thermal oxidation is carried out on a heavily doped, low resistance Si wafer to define the CMUT gap height. The lateral geometry of the gap is defined lithographically, and the oxide is etched down to the Si. After the growth of a second oxidation layer to define the isolation, an SOI wafer is directly bonded onto the

wafer followed by an additional thermal oxidation step to increase the strength of bonding between the two wafers. The handle and buried oxide (BOX) of the SOI is then removed through mechanical grinding and etching, forming the CMUT top plates composed of the Si device layer. Contact to the bottom electrode is obtained by etching the oxide is etched down to the Si layer, followed by metallization via sputtering. The electrodes are then defined and isolated by lithography and etching through the Si plate. The gap thicknesses of the CMUT cells fabricated using wafer bonding can be controlled reasonably well within $\sim 100\text{nm}$, with further reduction possible through LOCOS (local oxidation of silicon) process [37].

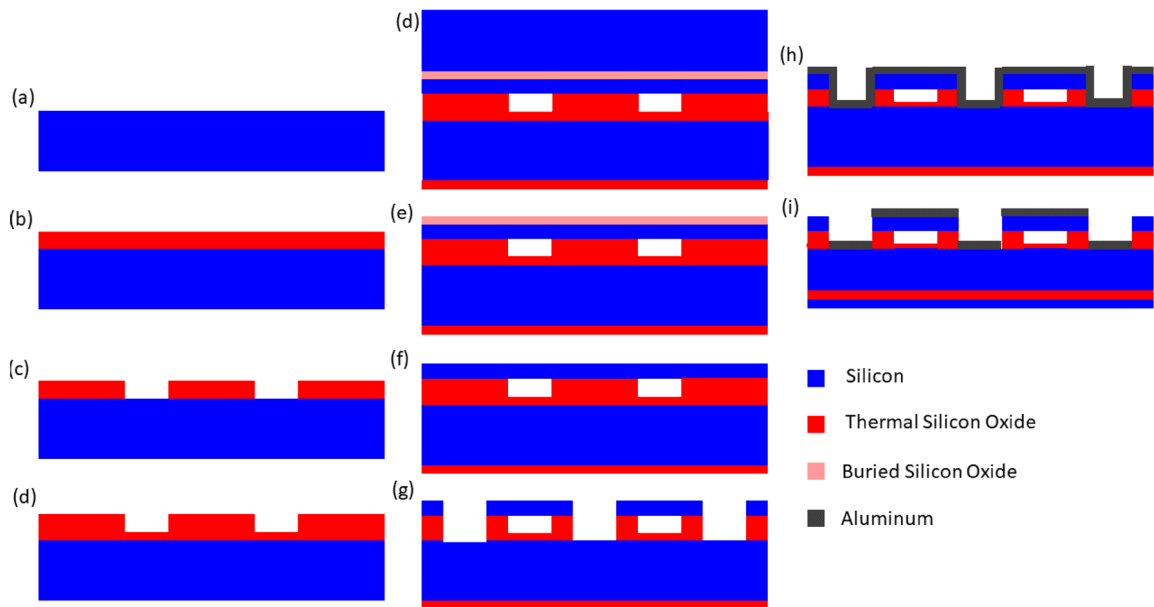


Figure 1.5: Process flow for a wafer-bonded CMUT. (a) Starting prime wafer. (b) Thermal oxidation. (c) Etch to form cavity. (d) Thermal oxidation. (e) Silicon on insulator (SOI) wafer bonding. (f) SOI handle. (g) Removing buried oxide. (h) Sputtering metallization. (i) Metal pattern and device isolation. [36]

As the wafer bonding technique does not require sacrificial layers, issues that might arise from wet etching of the sacrificial layer, such as chemical selectivity and stiction, are

avoided. Lack of sacrificial layers also allow greater flexibility in membrane geometry design. Utilization of SOI wafers and thermal oxide in fabrication enable CMUT cells of good membrane thickness uniformity and lower residual stress, but significantly increases the cost and required process temperatures. Moreover, the wafer bonding step of the fabrication process is very sensitive to cleanliness and surface roughness of the bonded wafers, which can result in low fabrication yield.

The sacrificial layer technique utilizes surface micromachining processes to create a sacrificial layer which is then etched to create the vacuum gap. A sample fabrication process flow can be seen in Figure 1.6 [36]. A silicon nitride insulator layer is deposited on the wafer, followed by a sacrificial polysilicon layer. The sacrificial layer is patterned to define the individual CMUT cells. A second sacrificial layer is deposited to allow access to the etchant during sacrificial etch. The top plate is formed by silicon nitride deposition. Etch holes are patterned on the top plate and a potassium hydroxide wet etch is used to remove the sacrificial polysilicon. The resultant gap is vented to atmosphere and sealed using low pressure chemical vapor deposition (LPCVD) of silicon nitride. As the LPCVD is performed at very low pressure, the gap is effectively in vacuum after the sealing process. Aluminum is then deposited and patterned to form the electrodes and interconnects. The materials that can be utilized in sacrificial release technique are not limited by the ones described in the sample fabrication process flow, but special concern should be given to chemical selectivity between device and sacrificial layers.

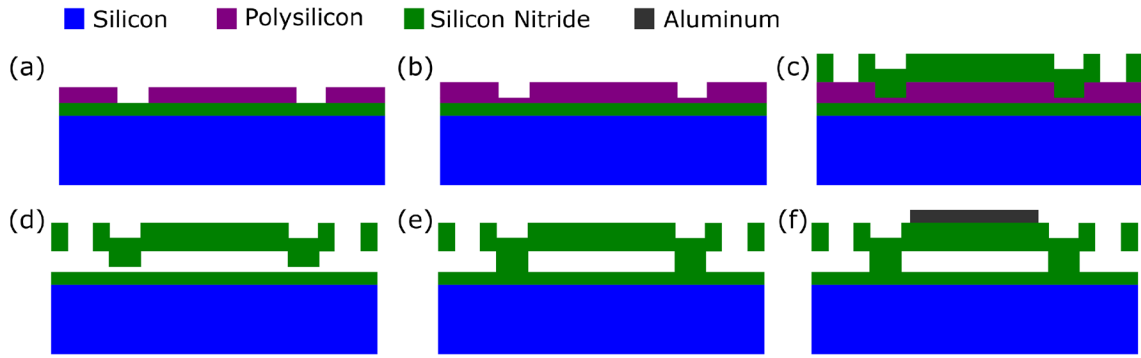


Figure 1.6: Process flow for CMUT fabrication with sacrificial release. (a) Sacrificial polysilicon deposition and patterning on silicon nitride deposited wafer. (b) Sacrificial polysilicon deposition for etch channels into the cells. (c) Silicon nitride top plate layer deposition and patterning. (d) Sacrificial polysilicon layer etching. (e) Silicon nitride deposition to seal the cells. (f) Aluminum deposition and patterning for electrodes and interconnects. [36]

The sacrificial layer technique utilizes relatively simple and reliable surface micromachining processes, eliminating the need for expensive SOI wafers and the precise and extremely clean surface conditions required during the wafer bonding step. A complete fabrication flow can be designed below the complementary metal–oxide–semiconductor (CMOS) substrate maximum processing temperature of 400°C [38], allowing postprocess CMOS integration. However, deposition conditions of the device layers can cause intrinsic stress in the membrane resulting in the deformation of the membrane, and wet etching of the sacrificial layer can cause stiction, in which the capillary forces of the liquid prevent the total release of the membrane. These fabrication issues and the need for sacrificial etch holes limit the membrane geometry and gap thicknesses that can be fabricated through sacrificial layer technique.

1.2.3. Electronics Integration Comparison

The transducer needs to be complemented with front-end electronics to translate the received echoes into a digital image in ultrasonic imaging systems. The front-end electronics can be connected to the transducer array via cables or positioned in the ultrasound probe as active electronics. There are several advantages in utilizing active front-end electronics. Active electronics reduce the parasitic circuit elements that arise from the long cables, specifically the parasitic capacitance, improving the bandwidth and SNR of the system. Active electronics are also required to reduce the number of transducer channels to the number of channels in the imaging system in cases where the number of array elements are high.

Connection cables do not generate considerable loss in bulk piezoelectric devices due to their low electrical input impedance. Therefore, active electronics integration has been focused on devices with large number of transducer elements. Fabrication of piezoelectric materials with high electromechanical factor require temperatures exceeding the CMOS processing temperature. Therefore, the transducer and CMOS chips are fabricated separately and then electrically connected using multi-chip integration. Wire bonding can be used if the number of individual connections is low, whereas flip-chip bonding is required for large number of connections. Flip-chip bonding has been used to successfully fabricate CMOS integrated bulk piezoelectric devices for intracardiac echocardiography (ICE) [39] and transesophageal [40] echocardiography. However, as seen from the cross section of the device in Figure 1.7, the requirement of matching layers complicates the multi-chip integration and makes fabrication difficult.

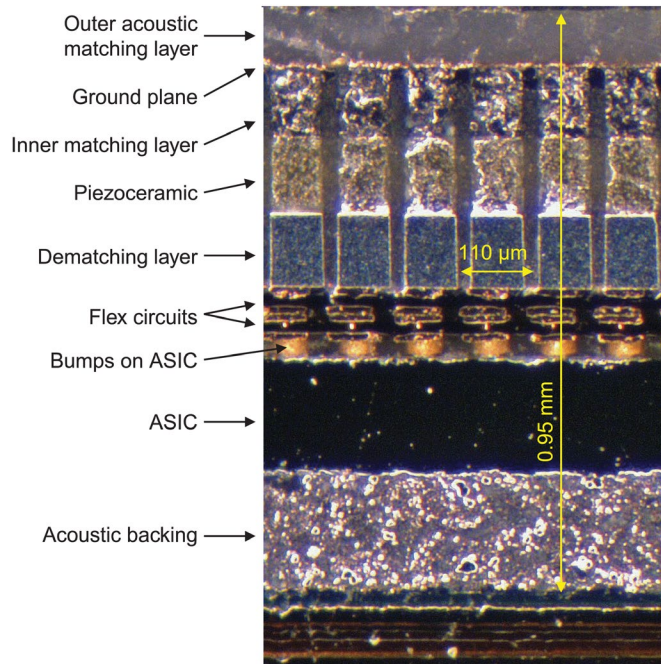


Figure 1.7: Cross section of CMOS integrated bulk piezoelectric ICE device [39].

Unlike bulk piezoelectric devices, CMUT arrays demonstrate high electrical input impedance and are therefore more sensitive to the parasitic elements of the long connection cables. As a result, active electronics are crucial to obtain adequate SNR. Similar to piezoelectric devices, multi-chip integration can be utilized to electrically connect CMUT transducers and CMOS chips. As multi-chip integration uses separately fabricated, the CMUT fabrication processes are not limited by temperature or CMOS-compatibility, allowing more flexibility in CMUT design. Flip-chip bonding have been utilized to integrate CMUT arrays with electronics for a variety of applications, such as volumetric imaging [41-45], ICE [46], high intensity focused ultrasound (HIFU) [47], photoacoustic imaging [48]. Although the lack of matching layers makes flip-chip bonding simpler for CMUT arrays, the process still requires additional fabrication steps to connect the electrodes to the bottom side of the wafer, as seen in the cross section of the integrated

system in Figure 1.8. Moreover, for high frequency CMUT arrays the minimum solder bump pitch ($\sim 20 \mu\text{m}$) limits the element pitch that can be used.

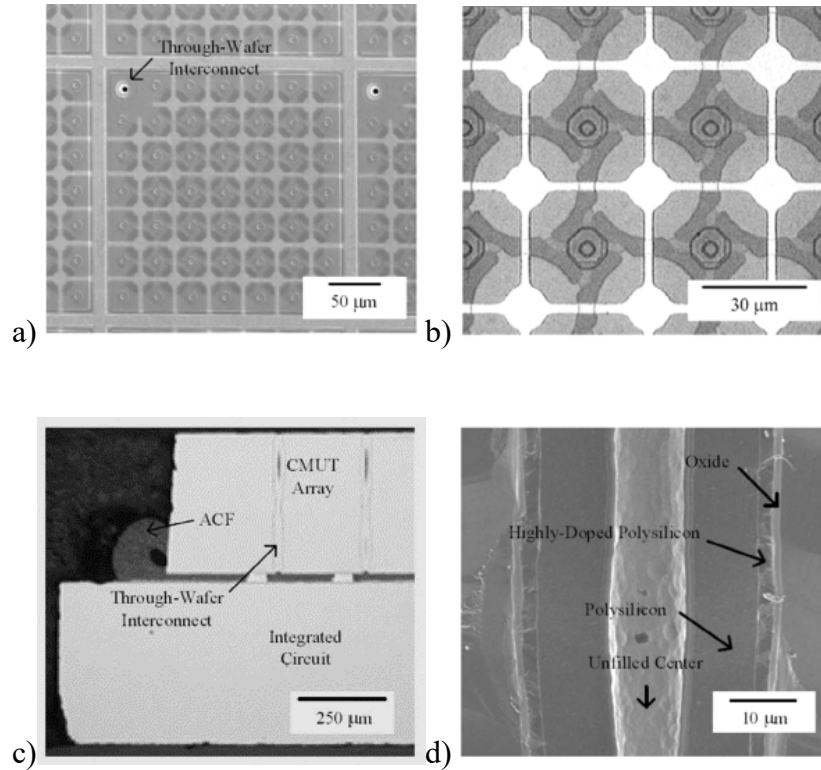


Figure 1.8: Flip-chip bonded volumetric CMUT array. a) Top view of individual element. b) Close-up to CMUT cells. c) Cross section of flip-chip bonded device. d) Close-up of the through wafer via. [36]

Compatibility of micromachining processes with CMOS processes enable monolithic integration of CMUT arrays with electronics. In monolithic integration, fabricated CMOS wafers are planarized using low temperature deposition and chemical-mechanical polishing (CMP) and followed by CMUT fabrication with sacrificial layer technique. The main drawback of this method is the imperfect surface topography after planarization and temperature limitation of the total fabrication processes required for CMOS compatibility. Monolithic integration supplies compact integration minimizing

parasitic elements associated with the connections while removing the additional fabrication steps required in flip-chip bonding, as seen in Figure 1.9. The minimization of the interconnect area is especially crucial for high frequency arrays that require small element pitch. Monolithic integration have been utilized to successfully fabricate CMUT arrays integrated with electronics for ICE [49, 50], and IVUS [51-53].

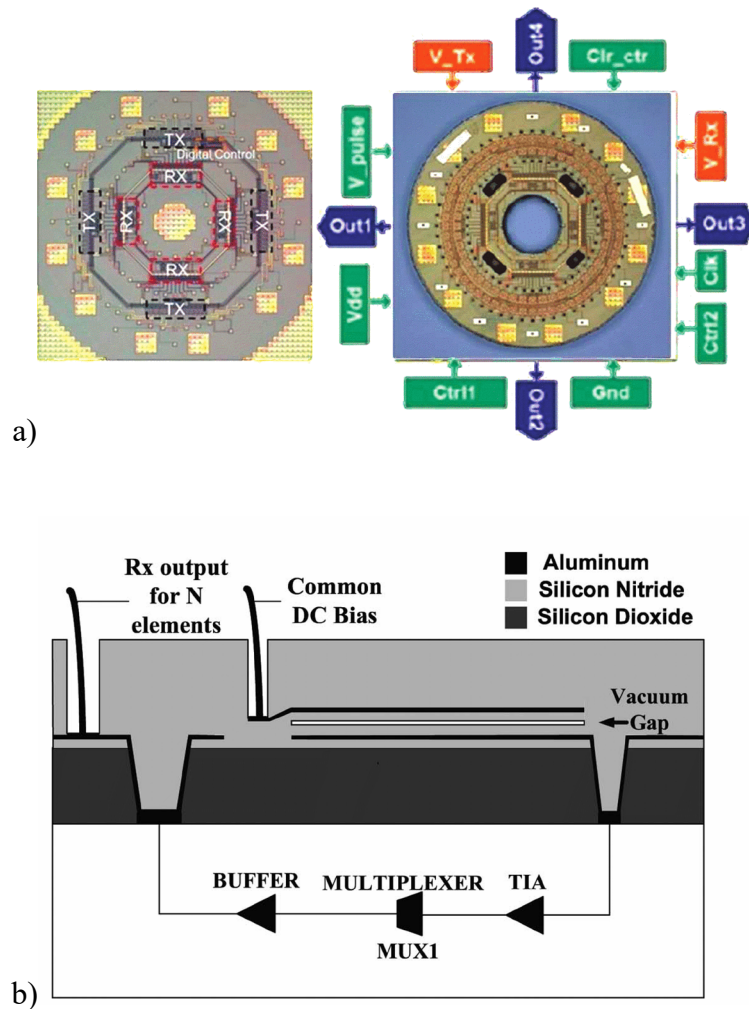


Figure 1.9: a) Micrograph of CMOS circuitry before (left) and after (right) monolithic integration of CMUT arrays [50]. b) Cross sectional schematic of the interconnections between monolithically integrated CMUT and CMOS [53].

1.3. High Frequency CMUT Arrays in Literature

Considering the operation and fabrication advantages CMUTs exhibit, CMUT arrays are particularly promising for high frequency ultrasound imaging systems. As a result, high frequency CMUT transducer arrays has been substantially demonstrated in literature, with operation frequencies ranging from 20 MHz up to 50 MHz [54]. The fabricated arrays possessed diverse membrane geometries, from 20 μm squares [55] to circles of varying diameters [27, 56-58]. Similarly, these arrays possessed diverse array geometries, with element pitches smaller or in the order of the ultrasound wavelength, ranging from 25 μm [55] to 65 μm [57]. The high frequency CMUT transducer arrays in literature exhibited a large variation of -6 dB fractional bandwidth (*FBW*) ranging between 28% [55] up to 100% [57]. However, the high *FBW* measurements are performed in highly attenuating media which can skew the results [54]. It is clear from these results high frequency CMUT transducer array performance depends on membrane and array geometry and applied DC bias among others. However, a thorough analysis of the array behavior and performance limitations is absent.

1.4. Objectives of This Work

The aim of this research is to determine and verify the performance limitations of high frequency CMUT arrays and develop a design methodology for specific operation requirements. This primary goal is divided into three research objectives. First an analysis framework that can examine the receiver and transmitter performance in a compact manner is developed. The effect of different design parameters is analyzed with particular focus on the frequency response and the SNR. Second, using the results obtained, a design

methodology for specific frequency band and SNR is determined. The design methodology is expanded further to encompass a broader frequency range and other applications. Third, the design methodology is used to design and fabricate two CMUT array sets of different operation frequency and characteristics. The specifications of array performance are verified through hydrophone and admittance measurement and simulation comparison. With the results in mind, a high frequency 1D CMUT array for IVUS imaging is fabricated and integrated to electronics, forming an imaging system. Performance of the ultrasonic imaging system is analyzed through pressure output, pitch-catch, and pulse-echo measurements. Finally, considering that CMUT array performance is also susceptible to the electrical termination conditions, the effect of different impedance matching scenarios is investigated.

CHAPTER 2. CMUT MODELING AND ANALYSIS

FRAMEWORK

CMUT design space includes, but is not limited to, bulk membrane material, membrane geometry, the vacuum gap thickness, array configuration, and electrical termination. A thorough analysis of the multiple design parameters of this expansive design space requires modeling a wide variety of CMUT array geometries. Ideally modeling and simulation capabilities need to be robust in membrane and array geometry, as well as small signal and large signal operation, all the while being computationally efficient. The modeling capabilities then need to be complemented with analysis methodology based on figures of merit pertinent to the CMUT array operation.

In this chapter different CMUT modeling approaches and their capabilities are reviewed, with detailed explanation of the nonlinear lumped model utilized in this research. Figures of merit of interest are determined and compiled into three different analysis methodologies focusing on receiver, pulse-echo and transmitter performance. The analysis methodologies are used to analyze the performance of a case study of guidewire IVUS imaging system.

2.1. CMUT Modeling

2.1.1. Parallel Plate Modeling

The simplest representation of a CMUT dynamics is a lumped parallel plate capacitor and a piston radiator to the first order, as seen in Figure 2.1. The parallel plate capacitor's mechanics can be modeled as a mass-spring-damper system of spring constant

k_p , mass constant m_p , and damping constant r_p , and the piston radiator's acoustic impedance as a mass-damper system of mass constant m_m , and damping constant r_m .

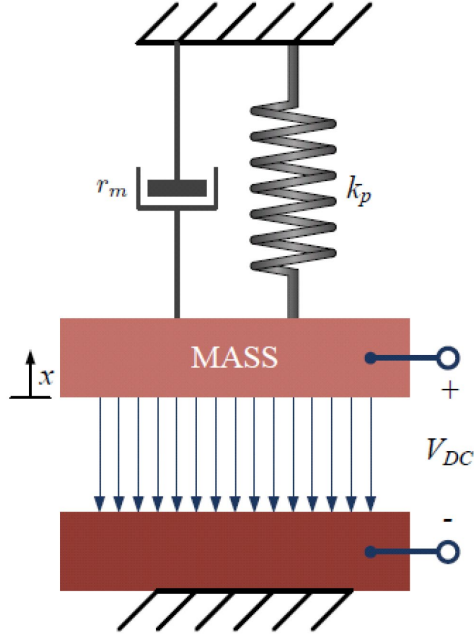


Figure 2.1: Parallel plate mass-spring-damper CMUT model. [36]

Considering static operation, applying a DC bias V_{DC} creates an electrostatic force F_{es} which is counterbalanced by the mechanical spring restoring force F_s , resulting in an equilibrium displacement x . Considering CMUT cells with an initial vacuum gap of g_0 and an isolation layer of thickness t_{iso} and relative permittivity of ϵ_r , the capacitance of the parallel plate capacitor, and the forces at equilibrium can be written as:

$$C(x) = \frac{A\varepsilon_0}{g_{eff} - x} \quad (2.1)$$

$$F_{es} = \frac{d(C(x)V_{DC}^2)}{dx} = -\frac{A\varepsilon_0V_{DC}^2}{2(g_{eff} - x)^2} \quad (2.2)$$

$$F_s = k_p x \quad (2.3)$$

where A is the area covered by the electrodes, ε_0 is the permittivity of the vacuum, and g_{eff} is the effective gap of the CMUT g_{eff} , which is defined as $g_{eff} = g_0 + t_{iso}/\varepsilon_r$. As mentioned in Chapter 1, above a bias point, $V_{DC} = V_{col}$, F_{es} cannot be balanced by F_s , resulting in the collapse of the flexible plate onto the rigid plate. From the force balance of F_{es} and F_s , the collapse voltage V_{col} and maximum achievable displacement x_{col} can be calculated as:

$$V_{col} = \sqrt{\frac{8k_p g_{eff}^3}{27\varepsilon_0 A}} \quad (2.4)$$

$$x_{col} = \frac{g_{eff}}{3} \quad (2.5)$$

The dynamic analysis of the CMUT can be carried out through the governing differential equations of the mass-spring-damper systems given as:

$$m_p \frac{d^2 x}{dt^2} + r_p \frac{dx}{dt} + k_p x = F_{es} - F_L - p_{atm} A \quad (2.6)$$

$$m_m \frac{d^2 x}{dt^2} + r_m \frac{dx}{dt} = F_L \quad (2.7)$$

where p_{atm} is atmospheric pressure, and F_L is the acoustic loading force on the piston. The constants m_m and r_m are defined by the radiation impedance Z_r of the piston. If the CMUT cell is significantly large in comparison to wavelength, the plane wave impedance $Z_0 = \rho_0 c_0$, where ρ_0 is the density and c_0 is the speed of sound of the medium, can be used, resulting in $m_m = 0$ and $r_m = Z_0 A$. However, CMUT cells are generally too small for plane wave impedance assumption, resulting in frequency dependent constants of $m_m = Im\{Z_r\}A/\omega$ and $r_m = Re\{Z_r\}A$.

2.1.2. Small Signal Analysis

As F_{es} is nonlinear, the system of equations obtained from parallel plate modeling are difficult to solve. The nonlinear differential equations can be linearized around an operating point if the time dependent alternating current voltage $V_{AC} \ll V_{DC}$ and the time dependent displacement $x_{AC} \ll x_{DC}$, where x_{DC} is the operating point displacement corresponding to V_{DC} [59]. By applying Taylor series expansion to the equations around V_{DC} and x_{DC} and dropping the second harmonic terms, the system of equations is simplified to:

$$\begin{aligned}
(m_p + m_m) \frac{d^2 x_{AC}}{dt^2} + r_m \frac{dx_{AC}}{dt} + \left(k_p - \frac{A \varepsilon_0 V_{DC}^2}{(g_{eff} - x_{DC})^2} \right) x_{AC} \\
= - \frac{A \varepsilon_0 V_{DC} V_{AC}(t)}{(g_{eff} - x_{DC})^2}
\end{aligned} \tag{2.8}$$

It can be observed that as the applied V_{DC} increases, the systems effective spring constant decreases. This reduction is due to the spring softening effect and results in a decrease in the resonance frequency of the transducer.

The linearized equation can be analogously described by the Mason equivalent circuit seen in Figure 2.3 [60]. In the figure, Z_{eq} is the total electrical input impedance of the CMUT device, Z_m is the mechanical impedance of the mass-spring-damper system, C_p is the parasitic capacitance, C_0 is the parallel plate capacitance at the operating point for V_{DC} , and φ is the transformer ratio between the applied voltage and F_{es} such that:

$$\varphi = \frac{A \varepsilon_0 V_{DC}}{(g_{eff} - x_{DC})^2} \tag{2.9}$$

From the equivalent circuit it can be directly observed that a higher transformer ratio φ would result in better electromechanical transduction. As a result, as V_{DC} is increased, the electromechanical coupling factor k_T is increased.

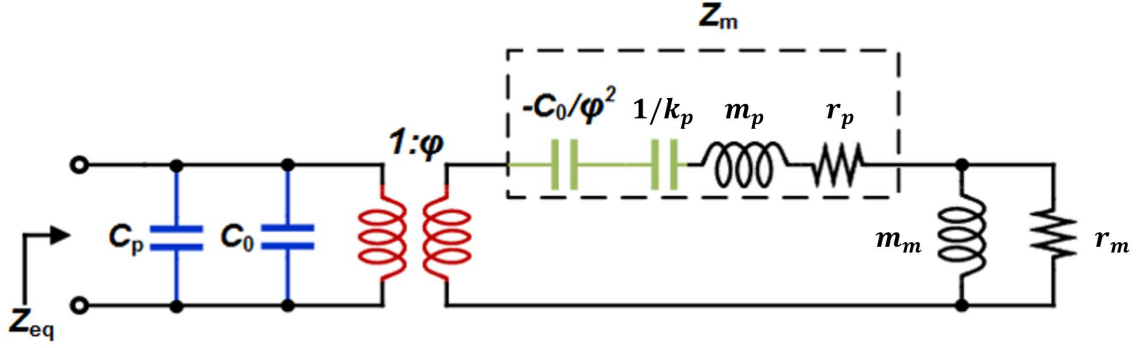


Figure 2.2: Mason equivalent circuit for linearized parallel plate CMUT.

Small signal operation assumption also allows direct calculation of k_T [61]. Using the operating point capacitance C_0 , and the slope of the charge voltage curve, defined as free capacitance C_{free} , the transducer's k_T^2 can be calculated as:

$$C_0 = \frac{Q(x)}{V} \Big|_{x_{DC}, V_{DC}} = C(x) \Big|_{x_{DC}, V_{DC}} \quad (2.10)$$

$$C_{free} = \frac{dQ(x)}{dV} \Big|_{x_{DC}, V_{DC}} = \frac{dVC_0}{dV} \Big|_{x_{DC}, V_{DC}} \quad (2.11)$$

$$k_T^2 = 1 - \frac{C_0}{C_{free}} \quad (2.12)$$

As mentioned in Chapter 1, k_T^2 increases with V_{DC} , approaching 100% at values close to V_{col} . The effect of V_{DC} on the k_T^2 of a CMUT can be seen in Figure 2.3.

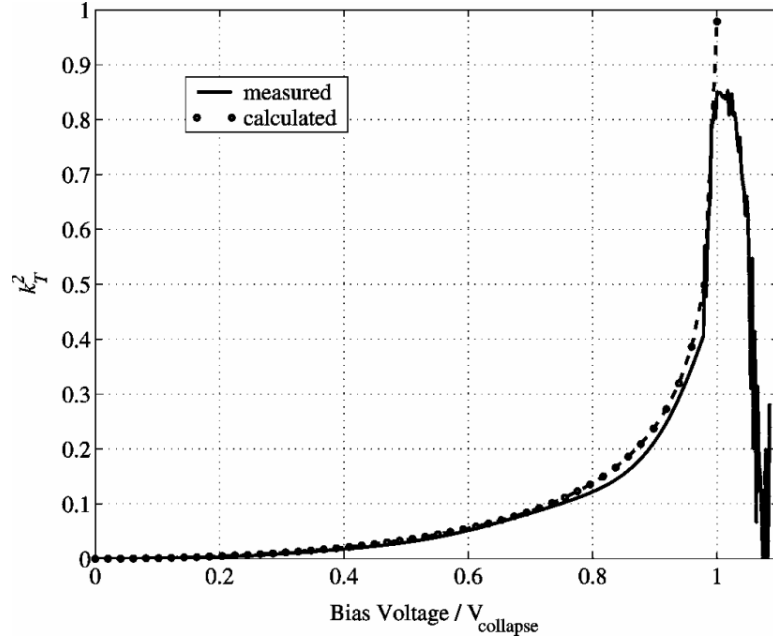


Figure 2.3: Calculated and measured electromechanical coupling factor of a CMUT as a function of V_{DC} normalized to V_{col} [61].

2.1.3. Finite Element Modeling

The described parallel plate model assumes that only the first vibration mode of the membrane is excited with electrical excitation. Therefore, higher order modes and other nonlinearities, such as stress stiffening and charge distribution variation for large deformations, are neglected. Finite element analysis (FEA) is ideal in capturing all underlying physics in multi-physics systems such as CMUTs. In finite element method (FEM), the CMUT operation is described as partial differential equations and boundary conditions. The simulation domain is divided into multiple small elements, called finite elements, over which simple equations are used to approximate the original complex partial differential equations. The set of simple equations of the finite elements are then assembled into a larger system to model the entire domain. The true solution is obtained by minimizing the error using calculus of variations. FEA is especially beneficial for analysis of complex

CMUT shapes and arbitrary configurations. However, the need to mesh the fluid medium significantly increases the number of nodes resulting in computationally expensive simulations.

2.1.4. Nonlinear Lumped Large Signal CMUT Model

To overcome the limitations observed in both parallel plate and finite element modeling, a nonlinear lumped large signal CMUT model has been developed by Satir [62]. The developed model is comprised of three main sections visualized as blocks in Figure 2.4. Block A calculates the electrostatic force on each electrode and accounts for the nonlinearity observed in large-signal CMUT modeling. Block B evaluates the vibroacoustic behavior of the CMUT array as a linear multiple-input multiple-output (MIMO) system incorporating forces on the electrodes to average displacements. It should be noted that Block B only considers the effect of fluid-solid interface waves and does not include mechanical coupling between CMUT membranes through the substrate, such as Lamb waves in the silicon wafer. These two blocks together define the electromechanical behavior of the CMUT array. Block C is a multiple-input single-output system that evaluates pressure at the desired point in the immersion fluid from the forces acting on the electrode patches. The effect of flat reflectors can be incorporated into the model by modifying Green's function utilized in blocks B and C. The analysis can be expanded by considering the CMUT array as a linear time varying capacitor in the electrical domain. This forms a two-port network with four degrees of freedom for each element: input electrical current I_i , applied electrical voltage V_i , mean membrane velocity v_i , and external acoustic force F_i , enabling the extraction of small signal equivalent circuit parameters, as well as integration of transmit/receive electronics.

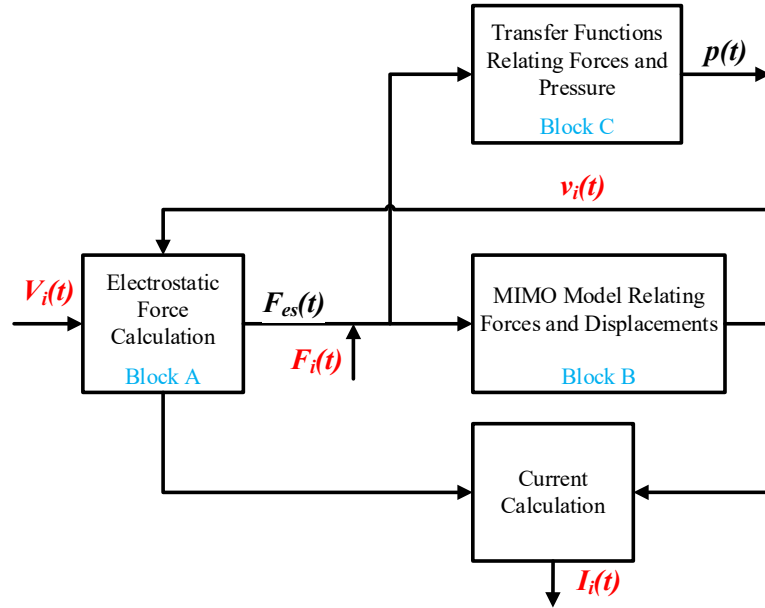


Figure 2.4: Block diagram of model developed by Satir and Degertekin [63].

2.1.4.1 Transmit Mode

For transmit mode analysis, modeling of the CMUT array's vibroacoustic response to an input electrical signal and the resultant pressure output is required. Boundary element model (BEM) is utilized to derive the vibroacoustic behavior in CMUT arrays. Utilization of BEM only requires 2D meshing of the CMUT array's vibrating surface area, reducing the computational load significantly as compared to 3D FEA. Meshing should be carried out such that every node can be considered as a baffled acoustic point source with uniform radiation pattern in the frequency range of interest. An example of a discretized transducer surface with a total of N nodes each with an associated $d_x \times d_y$ nodal area can be seen in Figure 2.5.

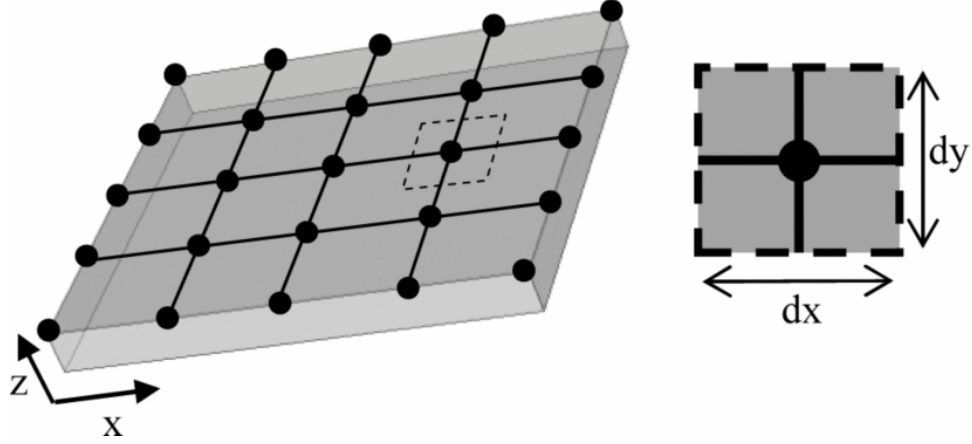


Figure 2.5: A CMUT membrane meshed into 5×5 matrix of nodes, $N=25$, with corresponding areas $d_x \times d_y$ [64].

Vibroacoustic behavior of the meshed system is defined by the surface area normalized force balance equation:

$$p_{ext} = m\ddot{u} + ku + p_{fluid} \quad (2.13)$$

where p_{ext} is the externally applied pressure vector, electrostatic pressure for transmit mode, p_{fluid} is the fluid loading pressure vector, m is the mass matrix, k is the stiffness matrix, and u is the displacement vector. Considering harmonic excitation at frequency ω , the nodal response of the array can be described in the frequency domain as:

$$\mathbf{u}(\omega) = \mathbf{G}^{-1}(\omega)\mathbf{p}_{app} \quad (2.14)$$

$$\mathbf{G}(\omega) = \mathbf{K} - \omega^2\mathbf{M} + j\omega\mathbf{Z}_r(\omega) \quad (2.15)$$

where \mathbf{p}_{app} is the nodal external pressure vector, $\mathbf{u}(\omega)$ is the nodal displacement vector, $\mathbf{G}(\omega)$ is the force balance matrix, which is calculated through the stiffness matrix \mathbf{K} , mass matrix \mathbf{M} , and mutual impedance matrix $\mathbf{Z}_r(\omega)$.

The stiffness matrix \mathbf{K} describes how nodal normal forces influence the displacement across the total membrane surface. For membranes of lateral dimensions much larger than the thickness under quasistatic operation, the stiffness can be approximated by Kirchhoff-Love thin plate equations. However, if membranes cannot be approximated as thin plates, either due to high aspect ratio, non-uniform cross section, or differing boundary conditions, static FEA can be utilized to obtain an equivalent \mathbf{K} . The nodal locations of the BEM mesh are implemented onto FEA, in which a uniform pressure of 1 Pa is applied to the finite area centered on each node, and the resulting displacement for each nodal location is calculated. This analysis is carried out for each node, forming N number of displacement vectors of N length. The equivalent stiffness matrix \mathbf{K} can then be obtained by concatenating these vectors and taking the resultant matrix's inverse. This approach enables removal of thin plate approximations, application of realistic edge boundary conditions, and evaluation of membrane geometries of arbitrary shape and cross section [64].

The mass matrix \mathbf{M} describes the inertia of each nodal area. For an array with arbitrary membrane geometries, the mass matrix is a diagonal $N \times N$ matrix with each term dependent on the local density and membrane thickness of each node.

The mutual impedance matrix $\mathbf{Z}_r(\omega)$ describes the fluid coupling of nodal displacements through acoustic propagation. Assuming each node as a baffled point radiator in semi-infinite fluid, Green's function can be utilized to calculate the fluid loading. Fluid loading of node q due to the displacement of node p can be expressed as $j\omega Z_r^{pq}(\omega)u_p$, where:

$$Z_r^{pq}(\omega) = \frac{j\rho_0\omega S}{2\pi} \frac{e^{-jr_{pq}k}}{r_{pq}} 10^{-\alpha(\omega)r_{pq}/20} \quad (2.16)$$

in which k is the wave number, ρ_0 is the fluid density, S is the nodal area $d_x \times d_y$, $\alpha(\omega)$ is the attenuation coefficient of the fluid as a function of frequency in decibels per meter, and r_{pq} is the distance between node q and node p . For the diagonal elements of $\mathbf{Z}_r(\omega)$ where $r_{pp} = 0$, fluid loading of an infinitesimally small circular piston with an effective radius of $a_{eff} = \sqrt{S/\pi}$ is utilized to obtain:

$$Z_r^{pp}(\omega) = \rho_0 c_0 \left[\frac{1}{2} (ka_{eff})^2 + j \frac{8}{3} (ka_{eff}) \right] \quad (2.17)$$

where c_0 is the speed of sound of the fluid. As the Green's function accounts for the radiation boundary conditions of the acoustic domain, no meshing of the fluid is required.

With all its terms calculated the force balance matrix $\mathbf{G}(\omega)$ can be formed and the nodal displacements can be solved for a harmonic load $p_{app}e^{j\omega t}$. To translate the vibroacoustic behavior of the CMUT array to time domain, the frequency dependent force balance matrix is converted into the MIMO finite impulse response (FIR) filter block B in Figure 2.4. To incorporate the electrostatic loading on the nodes the SIMULINK model shown in Figure 2.6 is utilized, in which the electrical drive signal vector $\mathbf{V}(t)$ is the input, and the electrostatic force vector $\mathbf{F}(t)$ is the output. To avoid neglecting the effect of higher order modes and non-uniform charge distribution in large displacement operation, each nodal area can be modeled as a separate parallel plate device that is mechanically coupled to other nodes. However, such a system would result in a large system of equations. Instead, the membrane electrode is divided into patches with coupled dynamics, of which the position and shape are chosen through modal analysis of the membrane. For thin symmetric membranes, electrode patches chosen to capture the first and second symmetric modes, with the second symmetric mode corresponding to the sixth vibration mode of the CMUT membrane results in an accurate prediction of nonlinear behavior in full swing [64]. The relationship between the average gap under an electrode patch and the total electrostatic force is determined from static analysis of the membrane. Assuming non-collapsed operation, the total electrostatic force on the patch corresponding to its average displacement is calculated considering the deflection profile of the membrane and patch.

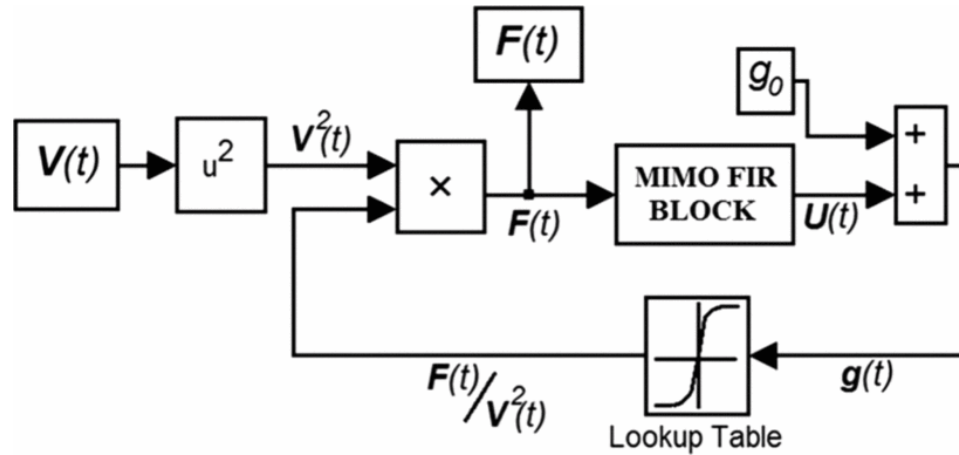


Figure 2.6: SIMULINK block diagram with input vector of voltage signals applied to array electrode patches and output force vector [64].

The pressure at an arbitrary point in the immersion fluid can be obtained from the calculated forces on the electrode patches. Using the baffled point radiator model, a frequency dependent pressure transfer function matrix can be formed between nodal displacements and pressure at the point of interest. Similar to the force balance matrix, this matrix is lumped for each patch and using the superposition principle, contribution of each excited electrode is summed to obtain the total pressure, forming a multiple-input single-output (MISO) system.

As comparison, the output pressure fields obtained with the models developed by Boulme *et al* [65] and Satir are plotted in Figure 2.7. The model developed by Boulme *et al* utilizes BEM with normal mode theory to form an admittance matrix between input voltage and mean velocities, with infinite periodic boundary conditions in the elevation direction. Modal decomposition of this admittance matrix is then carried out to determine the modes of the array that determine the frequency response. This model was capable of analyzing the CMUT response in a large frequency range, but the infinite periodic

boundary assumption could not handle realistic limited size effects and essentially this approach was limited to a single CMUT element of an imaging array with an “array” of membranes. In the figure, it can be clearly seen that the model developed by Satir can characterize effects on the frequency response that is ultimately ignored by the other model.

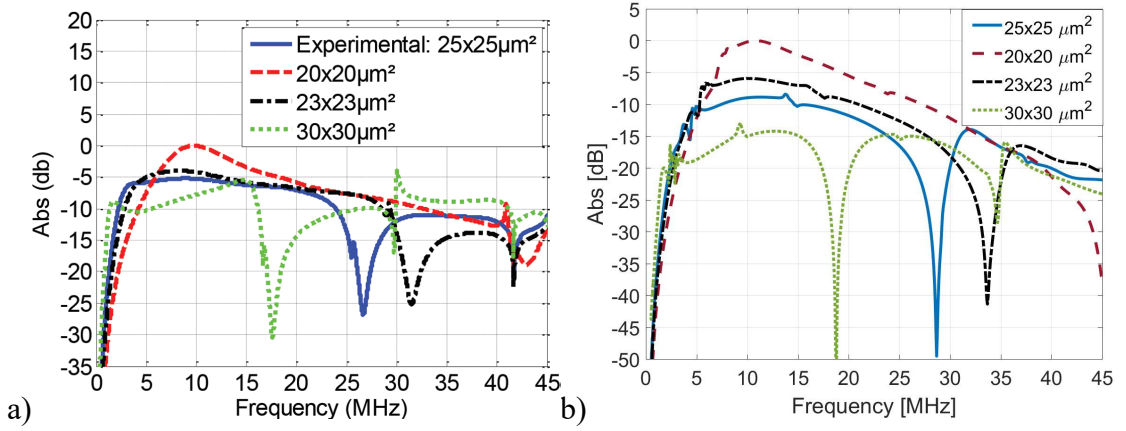


Figure 2.7: Comparison of pressure field simulated with models developed by (a) Boulme *et al* [65] and Satir [62].

2.1.4.2 Receive Mode

For receiver mode analysis, modeling of the CMUT array’s vibroacoustic response to an input pressure field and the resultant electrical output is required. Considering the force balance equation, incident pressure field p_{in} could be integrated to the externally applied pressure vector p_{ext} as:

$$p_{ext} = p_{ES} + 2p_{in} \quad (2.18)$$

where p_{ES} is the electrostatic pressure vector as calculated in transmit mode analysis. As a result, incident pressure can be directly added into the SIMULINK model as an input vector $F_{in}(t)$ for each electrode patch. Considering the CMUT array as a linear time varying

capacitor, the electrical output of the CMUT array can be obtained as an output current $i(t)$ as:

$$i(t) = \frac{dQ(t)}{dt} = \frac{d(V(t)C(t))}{dt} \quad (2.19)$$

where $V(t)$ and $C(t)$ are the instantaneous voltage and capacitance of the CMUT element. $C(t)$ is dependent on the average electrode patch displacement calculated in the SIMULINK model, and $V(t)$ is dependent on the integrated electronics impedance. For short circuit termination, $V(t)$ becomes simply the voltage input of the CMUT element.

2.1.4.3 Pulse-Echo Mode

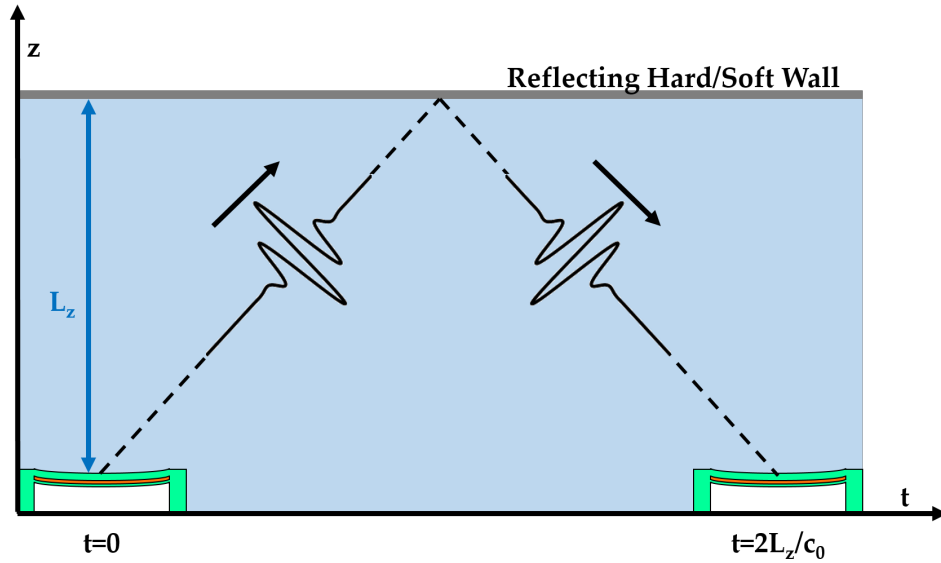


Figure 2.8: Pulse-echo operation.

Ultrasonic imaging is established on pulse-echo mode operation. As such, ultrasonic transducers are commonly characterized with pulse-echo experiments. During

pulse-echo experiments, the CMUT array operates as both a transmitter and a receiver, generating the pressure pulse and receiving the echo generated by a hard wall, such as a metal block, or a soft wall, such as the fluid-air, as seen in Figure 2.8. For pulse-echo mode analysis, the reflector needs to be incorporated into the CMUT array's vibroacoustic response. Assuming a flat reflector, method of images can be utilized to obtain the modified fluid loading component of the force balance equation, as seen in Figure 2.9 [66]. Using the modified fluid loading component to form Block B and Block C in the SIMULINK model, pulse-echo mode operation can be simulated for hard and soft walls of variable angles. Moreover, by investigating the time domain pressure fields propagating back and forth between the array and hard wall, acoustic reflectivity of the CMUT array can be evaluated.

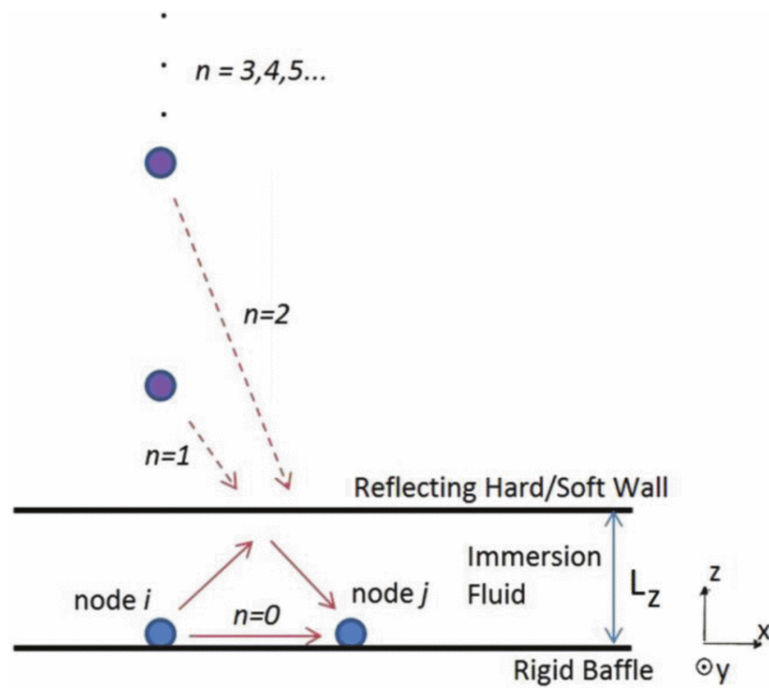


Figure 2.9: Geometry used for derivation of the modified fluid loading component of force balance equation via method of images [66].

2.1.4.4 Integration of Electronics

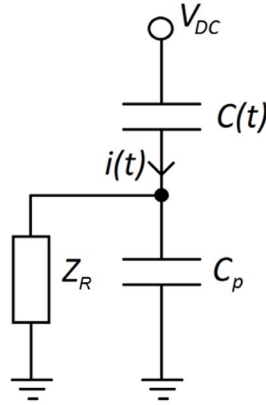


Figure 2.10: Electrical circuit for receive operation employing the CMUT as a variable capacitor [66].

As described in receive mode analysis, the electrical output of the CMUT array can be obtained as an output current dependent on the integrated electronics impedance. Considering receive operation, the integrated CMUT array and active electronics form a circuit as shown in Figure 2.10, where V_{DC} is the applied bias voltage, $C(t)$ is the CMUT array capacitance, $i(t)$ is the output current, Z_R is the receiver electronics impedance, and C_P is the parasitic capacitance. Assuming the receiver circuitry is linear in the operation frequency range, the instantaneous voltage on the CMUT array $V(t)$ is calculated as:

$$V(t) = V_{DC} - i(t) * \{Z_R || C_P\} \quad (2.20)$$

The effect of the receiver electronics on the instantaneous voltage of the CMUT can be incorporated into the SIMULINK model as an additional loop, as seen in Figure 2.11.

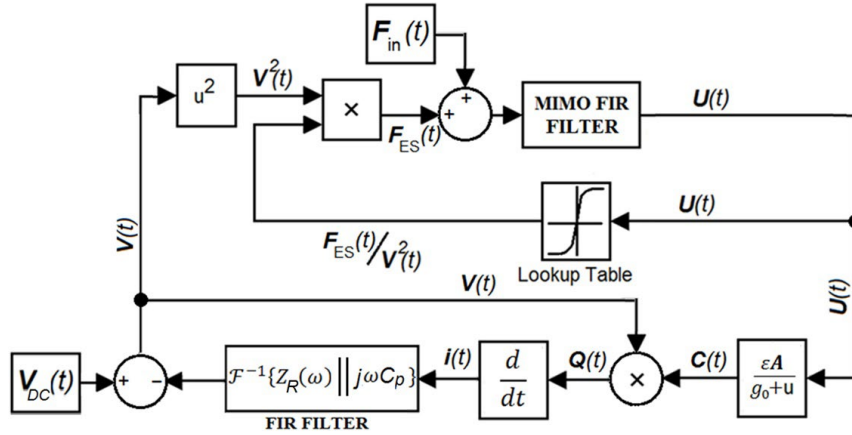


Figure 2.11: SIMULINK model with integrated receiver electronics [66].

Similar to receiver electronics, transmitter electronics can also be incorporated to the SIMULINK model as a loop. With the addition of a transmit/receive mode switch block, a complete system SIMULINK model can be formed, as seen in Figure 2.12, allowing for pulse-echo mode simulation of a complete integrated system.

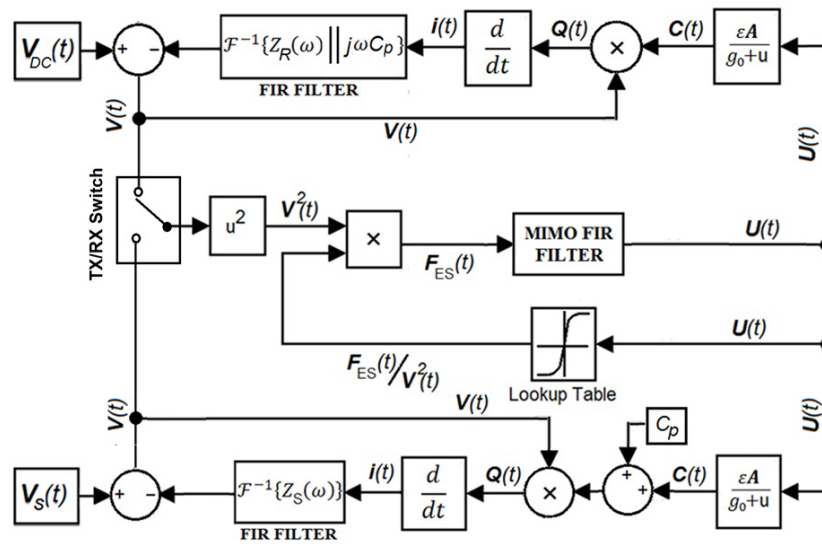


Figure 2.12: SIMULINK model with integrated transmitter and receiver electronics [66].

2.2. Analysis Methodology

Considering the applications of high frequency ultrasound imaging, a comprehensive analysis of CMUT arrays' performance would require focusing on both the receiver and transmitter characteristics. Previous analyses of CMUT array performance have focused solely the transmitter characteristics [65, 67]. Although CMUT arrays are capable of operating in transmit-receive mode, they are also favorable for applications that do not require CMUTs operating as transmitters such as photoacoustic imaging [68] and passive acoustic imaging [69, 70]. Therefore, separate analysis methodologies focusing on receiver, transmitter, and pulse-echo performance have been developed.

2.2.1. Receiver Analysis Methodology

For most conventional applications, CMUT arrays in receive mode are subject to small acoustic pressure waves, allowing the use of the small signal Mason equivalent circuit. The two-port network formed by the model enables extraction of multiple parameters from the equivalent circuit, including the CMUT element's electrical input impedance, thermal mechanical current noise, and pressure sensitivity. These parameters can be further combined to obtain the minimum detectable pressure wave amplitude of a CMUT element integrated with receiver electronics.

2.2.1.1 Impedance Calculation

Considering short circuit termination, the electrical impedance of a CMUT element Z_{CMUT} at a specific frequency ω is simply the ratio between the input voltage V and output current i when no acoustic force is present, written as:

$$Z_{CMUT}(\omega) = \frac{V(\omega)}{i(\omega)} \quad (2.21)$$

From transient simulation, the electrical impedance across the full frequency range can be calculated by modeling the output current of the CMUT element to an impulse input voltage. However, a small signal impulse input voltage cannot provide sufficient energy into the system for feasible analysis. As we are interested in only the impedance in the CMUT operation frequency, a more efficient method of calculation would be applying the input voltage as a Gaussian pulse with a frequency range similar to the CMUT operation frequency and modeling the resultant output current, as shown in Figure 2.13.

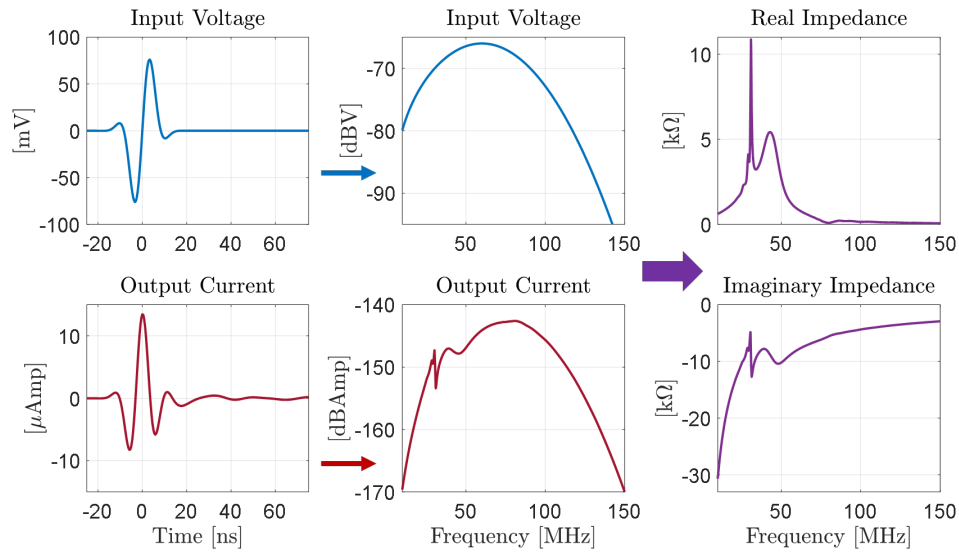


Figure 2.13: Impedance calculation through transient simulation.

2.2.1.2 Thermal Mechanical Noise

The calculated impedance can be utilized to obtain the thermal mechanical current noise of the CMUT array element [71]. Brownian motion, which is generated by the

random vibration of microscopic particles due to collisions with the atoms and molecules in the surrounding material, is considered as the source mechanism of thermal mechanical noise. These thermal vibrations generate a fluctuation force associated with the damper in the system with a spectral density of:

$$\overline{F_{TM\ noise}^2} = 4kTR_{mech} \quad (2.22)$$

where $F_{TM\ noise}$ is the noise force, k is the Boltzmann's constant (1.38×10^{-23} J/K), T is the temperature of the environment, and R_{mech} is the mechanical resistance. For a CMUT element of electrical impedance Z_{CMUT} , this term transfers to the electrical domain as:

$$\overline{i_{TM\ noise}^2} = 4kTRe(Y_{CMUT}) = 4kTRe\left(\frac{1}{Z_{CMUT}}\right) \quad (2.23)$$

where $i_{TM\ noise}$ is the current noise, Y_{CMUT} is the electrical admittance of the CMUT element, and Re denotes the real part of the complex admittance.

2.2.1.3 Plane Wave Pressure Sensitivity

Considering short circuit termination, the pressure sensitivity of a CMUT element to a plane wave, PS , at a specific frequency ω is simply the ratio between the input pressure p and output current i when input voltage is constant, written as:

$$PS(\omega) = \text{Mag} \left(\frac{i(\omega)}{p(\omega)} \right) \quad (2.24)$$

where Mag denotes the magnitude of complex ratio. Similar to impedance calculation, frequency dependent PS can be extracted from transient simulation by modeling the output current in response to an applied Gaussian force pulse. The same transient simulation can be also utilized to calculate the transformer ratio φ by calculating by dividing the output current i to its analog equivalent velocity v as:

$$\varphi = \frac{i}{v} \quad (2.25)$$

2.2.1.4 Pressure Noise Spectrum

For an ultrasonic receiver, the noise level determines the minimum signal strength that can be distinguished to form an image. Using the Mason equivalent circuit, the CMUT element electrical noise level can be translated into the acoustic domain as the pressure noise spectrum. The pressure noise spectrum is the most important measure of receiver performance, as it directly defines the minimum detectable pressure amplitude by the CMUT element. Pressure noise spectrum of a baffled piston can be obtained from its radiation impedance [72], enabling comparison the CMUT element receiver performance with an ideal case. For low noise receiver circuitry, the receiver electronics impedance is much lower than the CMUT element impedance, and can be approximated as a short circuit termination. As a result, the noise level of the imaging system can be assumed to the CMUT element's thermal mechanical noise [52, 73]. The thermal mechanical noise and plane

wave pressure sensitivity can then be used the pressure noise spectrum p_{noise} for plane waves as:

$$\overline{p_{noise}^2} = \overline{v_{TM\ noise}^2} / PS^2 \quad (2.26)$$

2.2.2. Transmitter Analysis Methodology

For most conventional applications, the CMUT array is operated as the transmitter to generate the echoes received by the CMUT element. In transmitter mode, an electrical pulse is applied to actuate the CMUT membranes, generating a pressure pulse proportional to the displacement of the CMUT membrane. To obtain the highest contrast ultrasonic image possible, the echo signal, and therefore the pressure output of the CMUT needs to be maximized. As a result, to analyze the full potential of the CMUT element as a transmitter, large signal analysis needs to be utilized. As high frequency operation is especially susceptible to acoustic attenuation, acoustic attenuation of the generated pressure wave cannot be ignored during modeling.

The nonlinear lumped model allows modeling of pressure output to any transient input pulse arbitrary points in the immersion fluid. This allows optimization of drive signals of the CMUT element along with determining the depth of field and resolution of the ultrasonic system. By modeling the pressure output to an input pulse at multiple points, the beam pattern of the CMUT element and hence the angular range of the ultrasound image can be calculated. For phased array operation modeling, the input pulse of each CMUT element can be set independently, allowing accurate simulation of electronic beam steering.

2.2.3. Pulse-Echo Analysis Methodology

Apart from the resolution and depth of field, the most important measure of ultrasonic imaging system is the SNR. Higher SNR of an imaging system would translate to higher contrast and greater dynamic range in the ultrasound image, making it easier to distinguish between parts of the tissue. Using pulse-echo mode modeling, the signal can be set as the output current generated the echo from a perfect planar reflector at a set distance and the noise level can be set as the thermal mechanical current noise of the CMUT element, as mentioned in the receiver analysis methodology. However, pulse-echo mode modeling is not limited to short circuit termination and different receiver electronics can be integrated by modifying the SIMULINK model. As a result, SNR calculation can be carried out for different CMUT element termination and realistic imaging systems. Pulse-echo mode modeling is capable of simulating the time domain pressure fields propagating back and forth between the CMUT array and the reflector. Through analysis of the multiple echoes, the reflectivity of the integrated CMUT, as in how much of a received pressure wave is reflected, can be evaluated.

2.3. Case Study: Guidewire IVUS Array

The motivating application for the case study is guidewire based IVUS imaging. As an important high frequency ultrasound application, IVUS provides critical diagnostic information regarding the arterial lumen size and plaque buildup. Despite its clinical value, IVUS is only used in ~20% of cardiovascular interventions [74]. One of the main reasons of the limited usage of IVUS is the dimensions of current IVUS catheters. Current IVUS catheters have a diameter of 2-4 Fr [75] and therefore cannot be used in narrow and severely

occluded arteries. In contrast, the guidewire used as the first step of IVUS procedures has a 0.014" diameter. Developing a guidewire with IVUS imaging capabilities would overcome the size limitation. Moreover, such a device would remove the need of separate IVUS catheter and guidewire, reducing the total examination time significantly.

2.3.1. Guidewire IVUS System

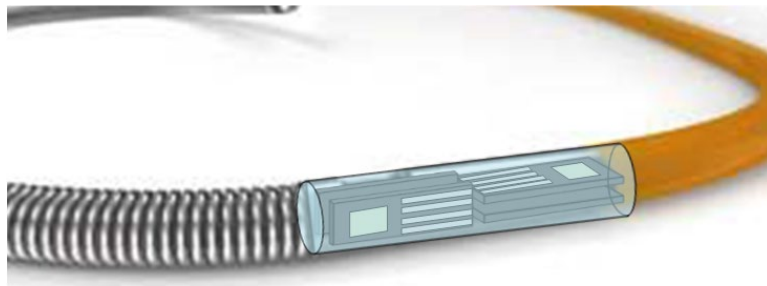


Figure 2.14: Conceptual schematic of the guidewire IVUS system.

The proposed guidewire IVUS is shown in Figure 2.14. Four 1D phased arrays are located in a small rigid capsule of the same size of commercial integrated pressure sensors for fractional flow reserve (FFR) measurements [55]. Full cross-sectional images of the artery are formed by joining 90° sector images obtained from the four 1D phased arrays as shown in Figure 2.15. To be able to integrate onto a 0.014" guidewire, each array needs to be ~300um in width. As a result, to achieve similar lateral resolution to that of a 20 MHz, 3.5F IVUS array, an operation frequency around 40 MHz is required. Due to the high impedance of CMUT array elements, and the limited area available, the guidewire IVUS system requires close integration to electronics to reduce the parasitic elements and cable count. Therefore, monolithic integration with CMUT-on-CMOS technology is considered as the fabrication method. As a result, the CMUT material properties are determined by

available low temperature fabrication processes and the available voltage on the CMUT arrays is determined by the integrated CMOS chip.

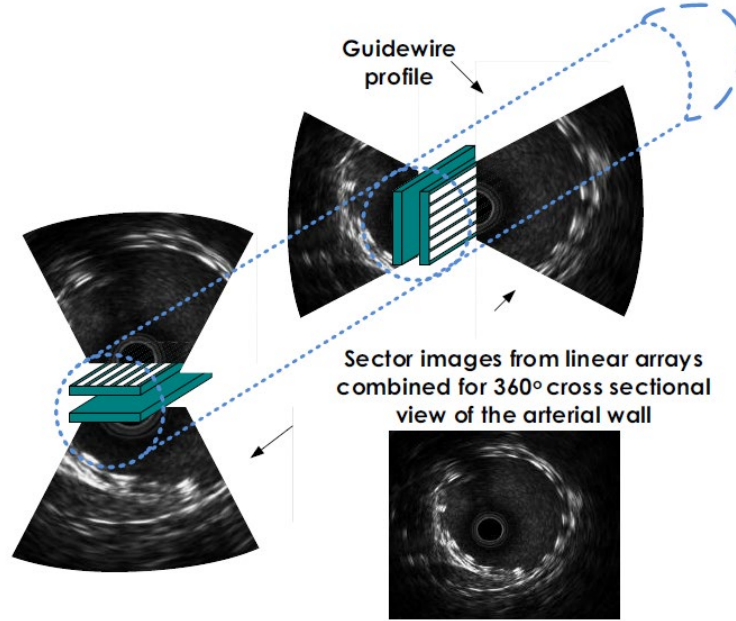


Figure 2.15: Schematic of full cross section image formation from four sectors obtained from the four 1D CMUT arrays [55].

2.3.2. Design Constraints

Analysis of 1D phased arrays operating in water with a f_{center} of 40 MHz is chosen for the case study. Total array size is chosen to be $300 \times 500 \mu\text{m}^2$ and the maximum element pitch (d_{el}) is chosen to be 33% larger than the half wavelength of the operation frequency, resulting in a maximum pitch of $25 \mu\text{m}$ and a minimum of 12 elements. Each element is populated with square membranes comprised of plasma enhanced chemical vapor deposition (PECVD) silicon nitride (Young's modulus (E) =110 GPa and density (ρ) =2040 kg/m³) of varying lateral dimensions (a), elevation (d_x) and azimuthal (d_y) membrane pitches, membrane thicknesses (h), and gap thicknesses (g), as seen in Figure

2.16. The stress in the nitride membrane is not considered. The electrode coverage of the membranes is kept constant at 56%, and the isolation material is chosen as HfO_2 (relative permittivity = 15) of a thickness (t_{iso}) so that the electric field under operation is at 75% of the breakdown field strength [76].

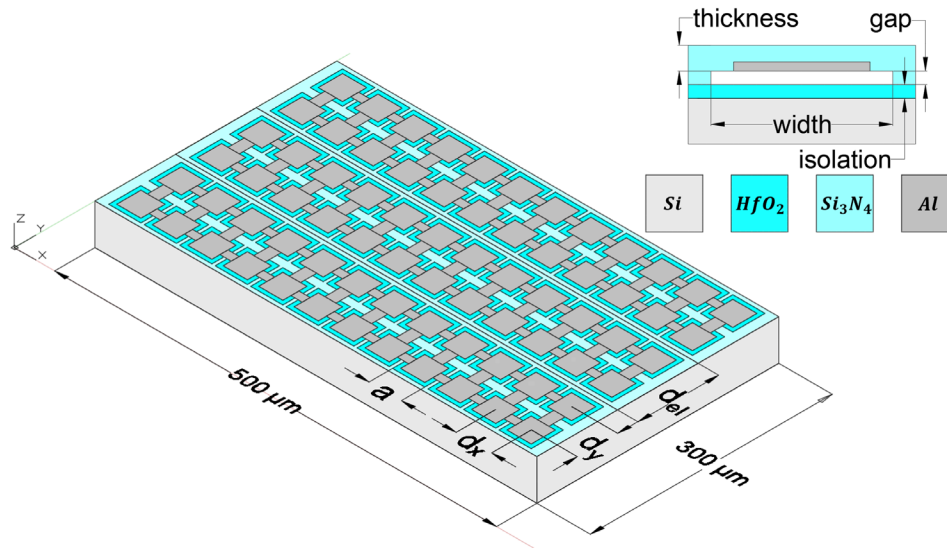
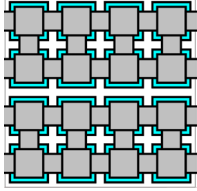
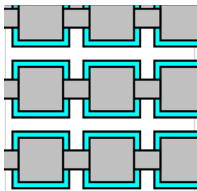
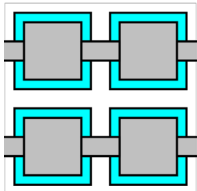


Figure 2.16: 2D representation of CMUT array. Cross section of a single membrane is seen in the inset.

Initial analysis is carried out on array geometries with varying lateral dimensions and constant fill factor (FF). Three high frequency 1D CMUT arrays are populated with membranes of three different lateral dimensions: 10, 15, and 20 μm . The elevation (d_x) and azimuthal (d_y) membrane pitch are kept at the same value (d) and adjusted to obtain 64% FF . The membrane thickness (h) is adjusted to obtain the desired f_{center} of 40 MHz. The analysis is then extended to different FF by modifying the d_x of the 10 μm array while keeping the same membrane geometry and d_y . A comparison of the array geometries of 64% FF can be seen in Table 2.1.

Table 2.1. Analyzed CMUT membrane geometries.

50x50 μm^2 section	a [μm]	d [μm]	d_{el} [μm]	# of Elements	h [μm]
	10	12.5	25	12	0.6
	15	18.75	18.75	16	1.2
	20	25	25	12	2.2

2.3.3. Receiver Analysis: Guidewire IVUS Array

2.3.3.1 Effect of DC Bias and Gap Thickness

Preliminary receiver performance analysis is carried out to analyze the effect of V_{DC} as percentage of V_{col} and gap thickness. The array geometry populated with 20 μm square membranes is considered as the basis. V_{DC} is swept from 50% to 90% V_{col} for an array with $g=45$ nm and the gap thickness is swept from 25 nm to 65 nm while the V_{DC} is kept at 90% collapse. Comparison of the extracted thermal mechanical current noise (I_{noise}), plane wave pressure sensitivity (PS) and pressure noise spectrum (p_{min}) of a single element of

the array can be seen in Figure 2.17 and Figure 2.18. As the ideal case, p_{min} of a baffled rectangular piston with the same geometry as the CMUT array element is considered.

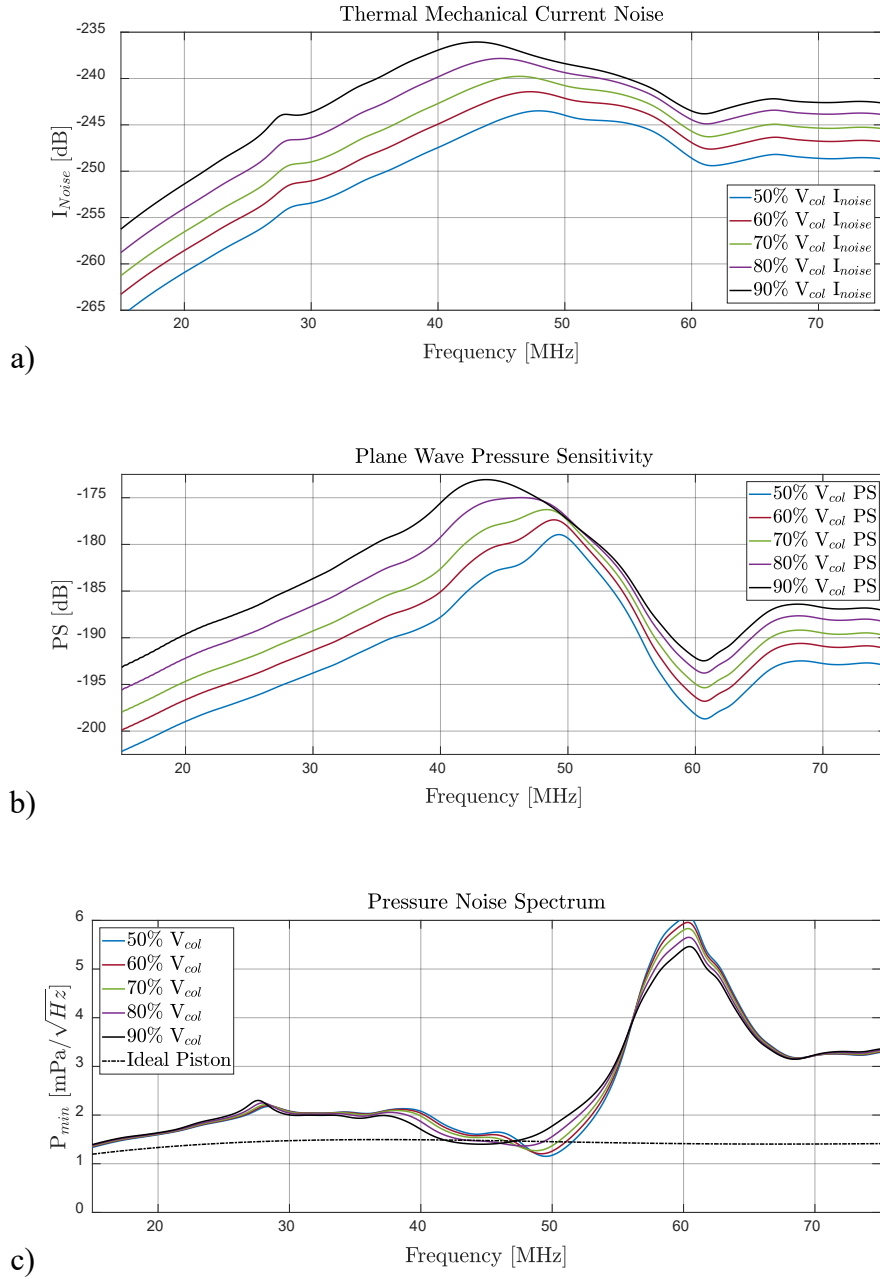


Figure 2.17: V_{DC} effect as percentage of V_{col} on current noise (I_{noise}), pressure sensitivity (PS) and pressure noise spectrum (p_{min}) of 20 μm membrane array elements.

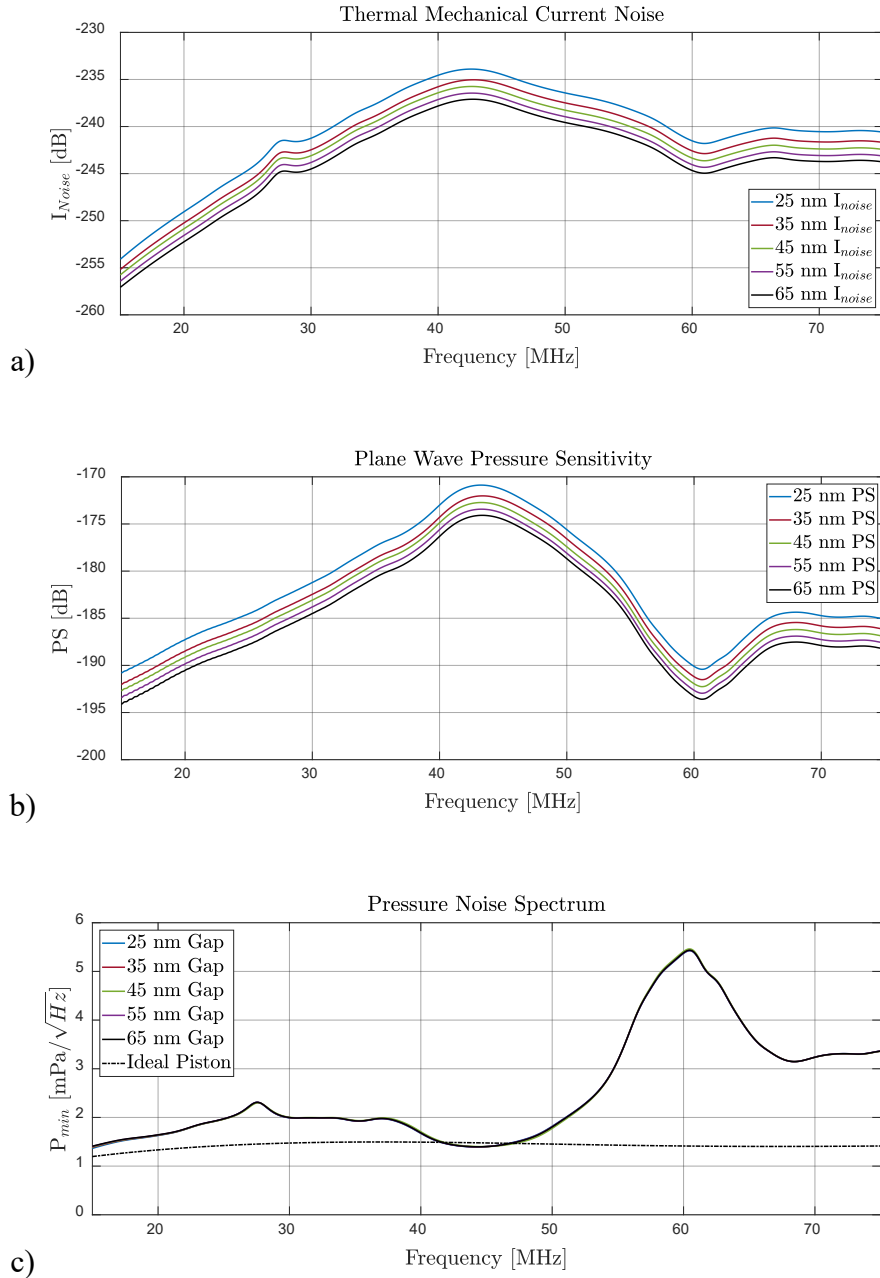


Figure 2.18: Gap thickness (g) effect on current noise (I_{noise}), pressure sensitivity (PS) and pressure noise spectrum (p_{min}) of $20\ \mu\text{m}$ membrane array elements.

As expected, both PS and I_{noise} increase as the V_{DC} is increased, with the effect of spring softening visible across the frequency spectrum. The same trend is observed as the gap thickness is decreased. Analyzing p_{min} of both cases reveal that the increase in PS is

mostly nulled by the increase of I_{noise} for both parameters. The effect of spring softening is visible in p_{min} , but is limited with respect to the overall receiver performance. From these results, it can be deduced that the gap thickness and to a lesser extent the V_{DC} have limited effect on the receiver performance of thermal mechanical current noise limited CMUT array element. As a result, the receiver performance is dictated by the membrane and array geometry, simplifying the design process.

2.3.3.2 Effect of Lateral Dimensions

Receiver performance analysis is extended to the three array geometries of different lateral dimensions. The receiver characteristic parameters are extracted for V_{DC} of 60 Volts, determined by the drain-to-source voltage (V_{DS}) of high voltage laterally-diffused metal-oxide-semiconductor (LDMOS) chips, with gap thickness adjusted for operation at 90% V_{col} , resulting in $g=72, 60,$ and 45 nm for $10, 15,$ and 20 μm membranes respectively. Since there are important differences between single element (SE) and imaging array element (AE) receiver characteristics, these cases are analyzed separately. The calculated I_{noise} and PS spectra for the CMUT membranes of Table 2.1 are plotted in Figure 2.19, with the salient features of the receiver performance dependent on lateral dimensions pointed out on the I_{noise} spectra. In the frequency range above the center frequency, three different cut-off frequencies are observed for each geometry (reference dips 1, 2, and 3) for both single and array elements. These cut-off frequencies are due to the Bragg's resonance (f_{Bragg}) of the elements. Bragg's resonance arises as a result of scattering caused by the periodic discontinuity of acoustic propagation between membranes. Destructive interference of the scattered waves forms a band gap at the frequency c_0/d ,

where c_0 is the speed of sound of the medium [77]. This resonance acts as a limiting factor to the frequency response of the CMUTs, both in single element and imaging array element, with smaller pitches resulting in higher limits.

In the frequency range below the center frequency, local sharp peaks and dips are observed especially for the imaging array elements (reference peaks 4, 5, and 6). These extrema are caused by the crosstalk between elements of the imaging array. Crosstalk excites subsonic and supersonic array modes in a frequency region around the first vibration mode resonance of the fluid loaded single membrane, resulting in multiple resonant peaks and dips and effectively forming a lower frequency limit [78, 79]. Crosstalk in the imaging array can also actuate higher vibration modes of single membranes (specifically the degenerate 2nd and 3rd modes which are the 1st asymmetrical modes of the square membranes shown as inset in Figure 2.19 (a)), resulting in additional resonant peaks and dips around the frequency range of these vibration modes. The location of these peaks relative to the Bragg resonance depends on the thickness of the membrane. For example, these “array excited” asymmetric vibration modes manifest themselves as a peak in the imaging array element populated with 10 μm membranes (reference peak 7). For the imaging array element with 15 μm membranes, these modes overlap with the Bragg’s resonance cut-off frequency, hence they are suppressed. Finally, for the imaging array element with 20 μm membranes, these resonances are above 125 MHz and hence they do not impact the response in the bandwidth shown in Figure 2.19. Note that these modes are “array excited” and require large number of membranes in the lateral dimension and phased excitation of the array element. Their effects are not pronounced in single element CMUTs

considered here as these elements are only one or two membranes wide, and also when the whole imaging array is excited in phase.

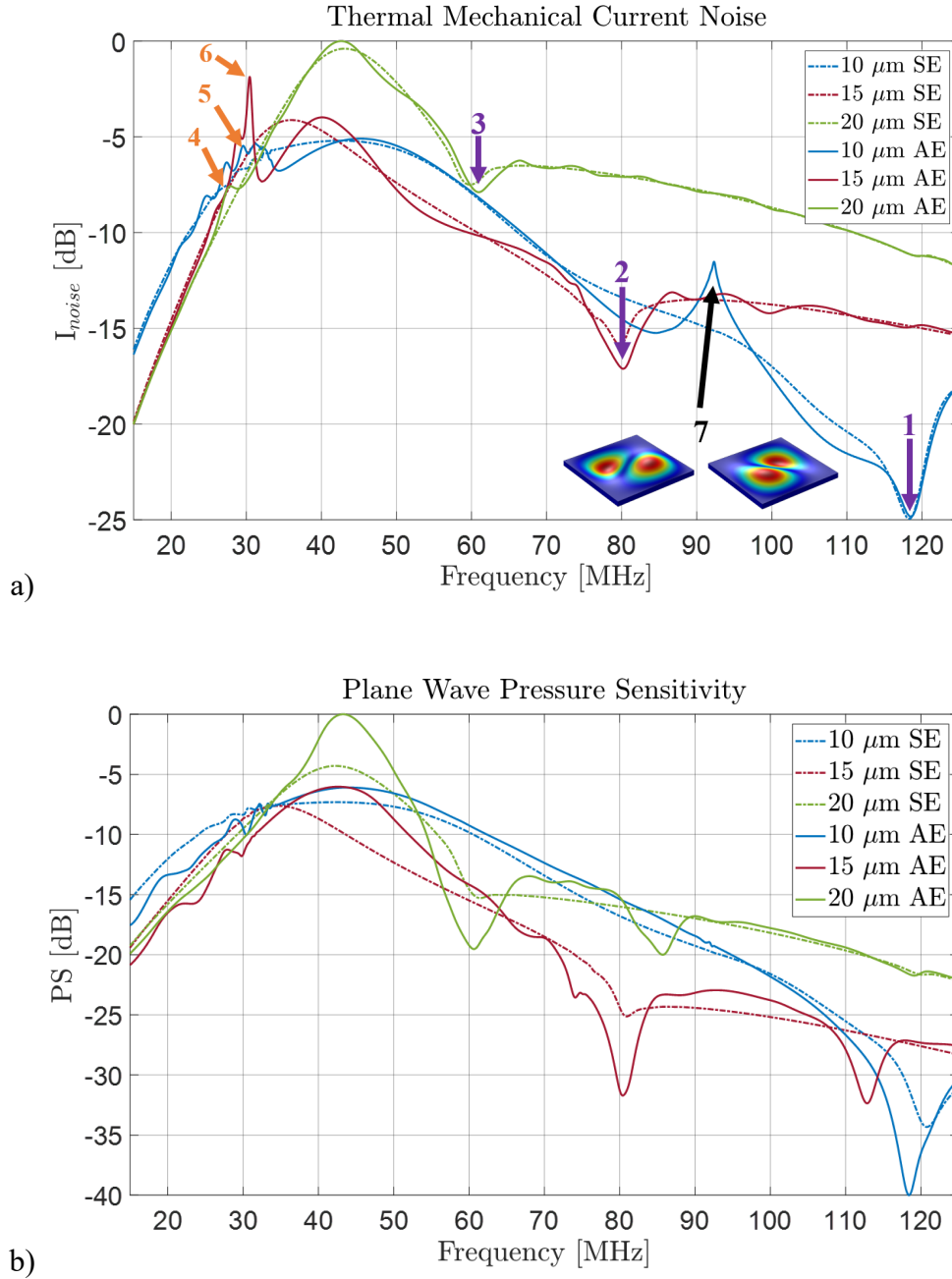


Figure 2.19: a) Current noise (I_{noise}) and b) pressure sensitivity (PS) spectra of SEs (dashed line) and imaging AEs (solid line) of different membrane geometries.

Overall, one observes a spurious resonance free range of frequencies between the first mode of the single CMUT membrane on the lower end and either Bragg or a higher order membrane mode resonance on the higher end [65, 80]. The effect of Bragg's resonance and crosstalk is also observed in pressure sensitivity. However, crosstalk is less prominent in pressure sensitivity, as that parameter is dominated by the in-phase excitation response of all membranes to a normally incident plane wave [81], whereas Bragg's scattering is more prominent with the effect of higher order Bragg's resonances visible in 15 μm and 20 μm membrane geometry.

The pressure noise spectrum of single elements and imaging array elements, along with the pressure noise spectrum of the ideal piston of the two element sizes are presented in Figure 2.20. It can be seen that utilizing membranes with smaller lateral dimensions approaches the receiver performance to that of the ideal piston, improving both sensitivity and bandwidth. Bragg's resonance manifests itself as an edge for single elements and a peak for imaging array elements. Crosstalk from neighboring elements increases the current noise and decreases sensitivity around the frequency region of single membrane resonance, resulting in several local maxima in pressure noise spectrum [79]. Similarly, in the array with 10 μm membrane geometry, the effect of crosstalk induced higher order membrane modes manifest themselves as another peak. These features are highlighted using the same numbering scheme of Figure 2.19 (a) for clarity.

Overall, compared to single element CMUTs, imaging array CMUTs have lower minimum detectable pressure in the spurious free frequency range, due to higher pressure sensitivity to incident plane waves. This increase is a result of the effective boundary conditions differing from an infinite baffle since imaging array elements are surrounded by

moving membranes. In addition, CMUTs with smaller membranes exhibit a pressure noise spectrum closer to the ideal piston over a broad frequency range (35-85 MHz for 10 μm membrane geometry).

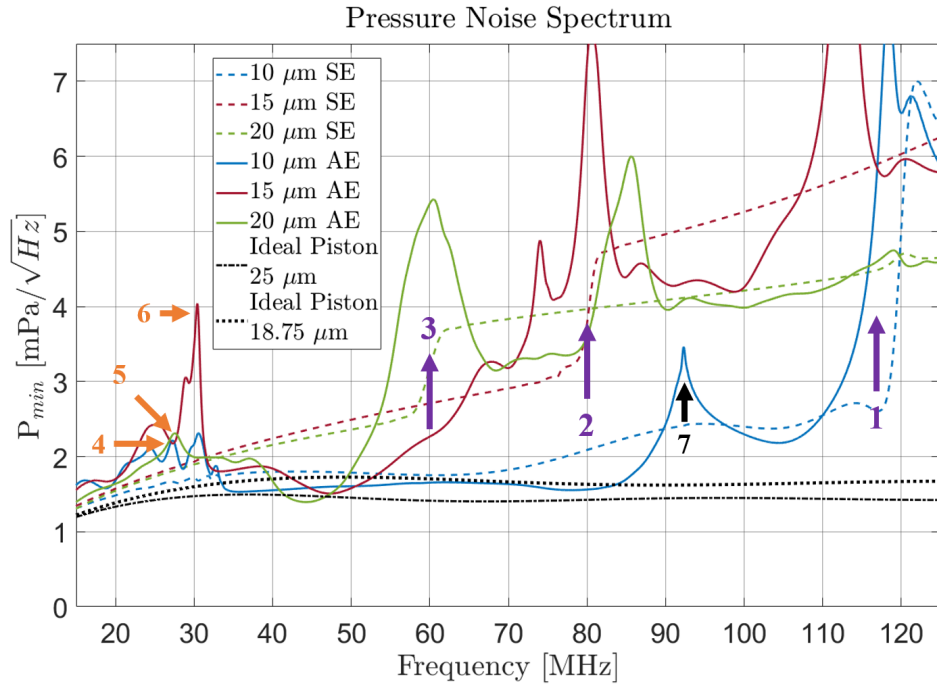


Figure 2.20: Pressure noise spectrum (p_{min}) of single elements (SE) and array elements (AE) with different membrane geometries.

2.3.4. Pulse-Echo Analysis: Guidewire IVUS Array

2.3.4.1 Effect of Lateral Dimensions

A transmit/receive performance analysis of CMUT imaging arrays is carried out by analyzing the pulse-echo response of imaging array elements of the previous geometries under unipolar pulsing. The performance is quantified using thermal mechanical noise limited pulse-echo SNR as a basis.

For best receiver sensitivity, the CMUT elements are biased close to collapse during transmit. Considering this limitation, two transmit pulsing methods are feasible for pulse-echo analysis: unipolar and bipolar pulsing. In unipolar pulsing, V_{DC} of the CMUT element is decreased to zero for the length of the pulse width, whereas in bipolar pulsing, V_{DC} is first increased to a certain value and then decreased to zero for the length of the pulse width. As a result, bipolar pulsing can utilize the gap thickness more efficiently. It has been shown that bipolar pulsing can enable an increase of 6 dB SNR compared to unipolar pulsing [82]. However, bipolar pulsing requires more complex electronics and a larger chip area for each element. Therefore, unipolar pulsing is considered in the pulse-echo analysis.

The maximum transmitted pressure output of a CMUT element operated in the non-collapsed mode is proportional to the gap thickness. Considering that the thermal mechanical current noise limited receiver performance of a CMUT array is independent of the gap thickness as demonstrated in the receiver analysis, the gap thickness must be maximized for optimum performance. The limiting factor therefore becomes the maximum available V_{DC} defined by the electronics integrated to the CMUT element. 60 V is chosen as the voltage limit for the initial analysis in which the gap thickness is adjusted for operation at 90% collapse voltage, followed by additional analysis on the effect of operation voltage.

The pulse-echo analysis is carried out with single unipolar pulse of 10 ns width, corresponding to $1/(2.5 \cdot f_{center})$ for a 40 MHz transducer which maximized the pulse-echo signal. The current signal due to the echo from a plane reflector positioned 5 mm from the CMUT array is analyzed (denoted as reflection current) to ensure far field operation. Comparison of the obtained reflection currents can be seen in Figure 2.21. Similar to the

receiver analysis, an increase in bandwidth is observed when smaller membranes are utilized. It is also observed that the signal levels are higher for wider array elements (25 μm width for 10 μm and 20 μm membrane elements, 18.75 μm width for 15 μm membrane elements). The noise value for SNR calculation is obtained by integrating the thermal mechanical noise over 20-60 MHz frequency range, assuming a 100% fractional bandwidth around 40 MHz for the receive system. SNR is then calculated as the ratio between the peak to peak value of the reflection current and root mean square noise. The SNR results for the three different designs can be found in Table 2.2. Analyzing the results, it is observed that utilizing larger elements improves the overall SNR, and utilizing smaller membranes improve both the overall SNR and the -6 dB fractional bandwidth.

Table 2.2. Characteristic of reflection currents and pulse-echo SNR of different membrane geometries in water

Membrane Width [μm]	f_{center} [MHz]	FBW [%]	Pulse-echo SNR [dB]
10	43.4	69	72.0
15	41.6	41	67.8
20	43.7	23	70.2

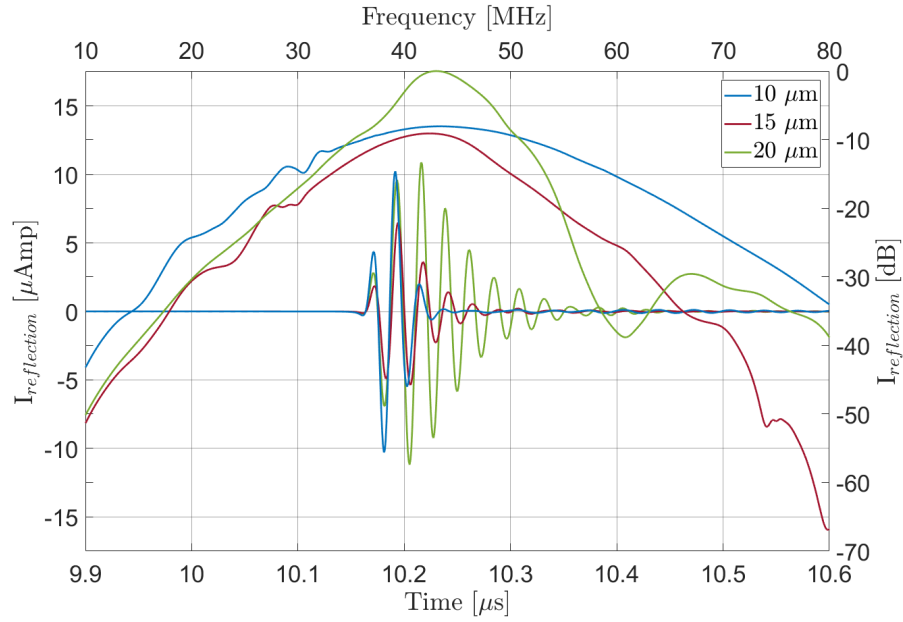


Figure 2.21: Membrane geometry effect on the reflection current of imaging AEs.

2.3.4.2 Operation in Blood

Since the assumed application of the arrays is in intravascular imaging, the performance of the different array geometries in blood is also analyzed. In comparison to water, blood has similar density and speed of sound, but significantly higher attenuation [83]. As a result, operating in blood does not alter the receiver performance significantly, but reduces the center frequency and SNR of the pulse-echo response. As the effect of attenuation increases with frequency, the center frequency shift is greater for arrays with higher fractional bandwidth. The characteristics of the reflection currents of the same setup operating in blood and the obtained pulse-echo SNR values can be found in Table 2.3. In all array geometries, operating in blood reduces the center frequency but increases the -6 dB bandwidth, which is in line with large fractional bandwidths observed in the literature when measurements are conducted in oil. In each case, the array element provides SNR

value above 50 dB. Assuming tissue walls to be weak reflectors of -40 dB, it can be deduced that each array has the capability of imaging a tissue wall at 5 mm distance in blood.

Table 2.3. Characteristic of reflection currents and pulse-echo SNR of different membrane geometries in blood

Membrane Width [μm]	f_{center} [MHz]	FBW [%]	Pulse-echo SNR [dB]
10	33.3	82	57.3
15	36.4	55	53.8
20	40.7	33	55.1

2.3.4.3 Effect of Operation Voltage

The pulse-echo analysis is extended to analyze the effect of operation voltage. Unipolar pulsing at 40, 60 and 80 V DC bias is carried out. The gap thickness and HfO₂ isolation thickness are adjusted to obtain 90% V_{col} and 75% of the breakdown field at each operation voltage. Larger V_{DC} enable utilization of larger gap thicknesses, resulting in larger pressure output and lower I_{noise} . A comparison of the obtained reflection currents and the thermal mechanical I_{noise} at the different operation voltages of the array geometry populated with 20 μm square membranes can be seen in Figure 2.22. The characteristics of the reflection currents and the resulting pulse-echo SNR values can be found in Table 2.4, Table 2.5, and Table 2.6. The results clearly demonstrate that increasing the operation voltage increases the SNR without affecting the frequency response of the array. From these results, it can be inferred that maximum available voltage must be utilized for best

pulse-echo response. The V_{DC} of the CMUT array should be maximized with respect to the pulsing method and electronics. The gap thickness should then be maximized accordingly. As the receiver performance is relatively independent of the gap thickness, available DC bias can be chosen as the main determinant of this design parameter.

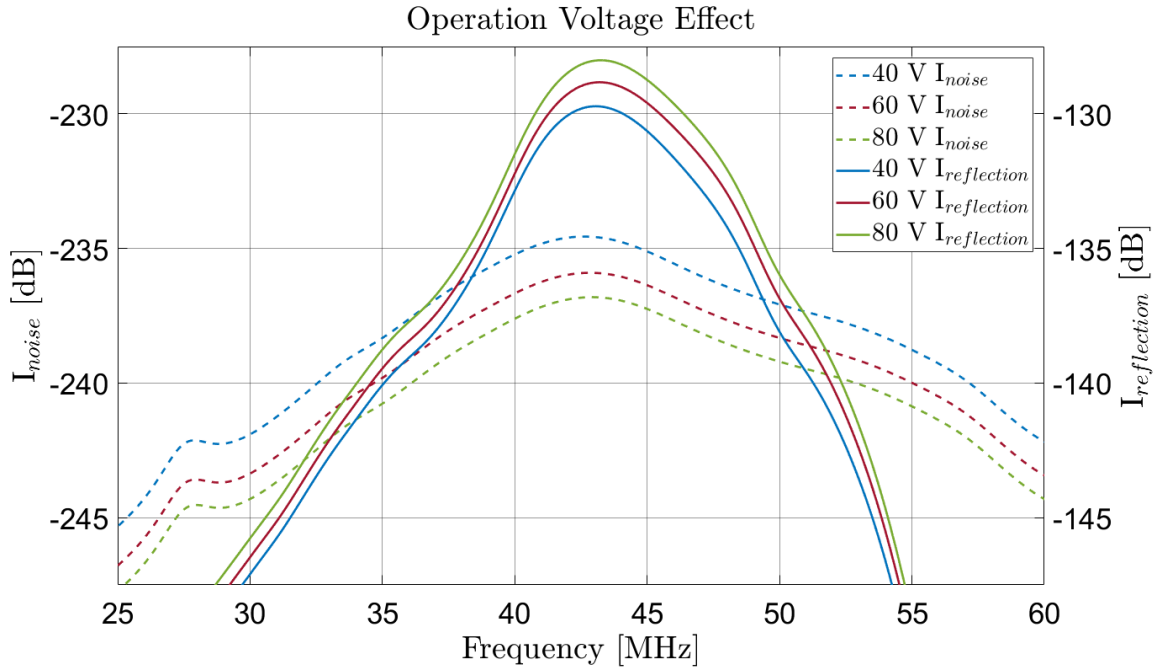


Figure 2.22: Membrane geometry effect on the reflection current of imaging AEs.

Table 2.4. Characteristics of reflection currents and pulse-echo SNR of 10 μm membrane geometry under different operation voltages

a [μm]	V_{DC} [V]	g [nm]	t_{iso} [nm]	f_{center} [MHz]	FBW [%]	Pulse-echo SNR [dB]
10	40	55	135	43.1	70	69.9
	60	72	200	43.4	69	72.0
	80	85.5	265	43.4	69	73.6

Table 2.5. Characteristics of reflection currents and pulse-echo SNR of 15 μm membrane geometry under different operation voltages

a [μm]	V_{DC} [V]	g [nm]	t_{iso} [nm]	f_{center} [MHz]	FBW [%]	Pulse-echo SNR [dB]
15	40	46	135	41.0	43	65.4
	60	60	200	41.6	41	67.8
	80	71	265	41.5	41	69.3

Table 2.6. Characteristics of reflection currents and pulse-echo SNR of 20 μm membrane geometry under different operation voltages

a [μm]	V_{DC} [V]	g [nm]	t_{iso} [nm]	f_{center} [MHz]	FBW [%]	Pulse-echo SNR [dB]
20	40	35.5	135	43.7	24	67.8
	60	45	200	43.7	23	70.2
	80	53.5	265	43.9	23	71.8

2.3.5. Transmitter Analysis: Guidewire IVUS Array

2.3.5.1 Directivity

The directivity of each imaging array element is examined through their transmit pressure beam patterns. Normalized beam patterns are shown in Figure 2.23. It is observed that the 25 μm wide element comprised of 10 μm membranes exhibits the lowest -3 dB span at $\pm 31.5^\circ$, indicating a larger equivalent rectangular element width (19 μm) as

compared to the 25 μm wide element comprised of 20 μm membranes, with an equivalent rectangular element width of 14 μm , and 18.75 μm wide element comprised of 15 μm membranes which exhibit -3dB spans of $\pm 54.9^\circ$ and $\pm 50.6^\circ$. However, the 10 μm geometry would provide a similar SNR over the $\pm 45^\circ$ range due its higher absolute SNR (Table 2.2). Overall, all three arrays would have radiation patterns suitable for phased array imaging.

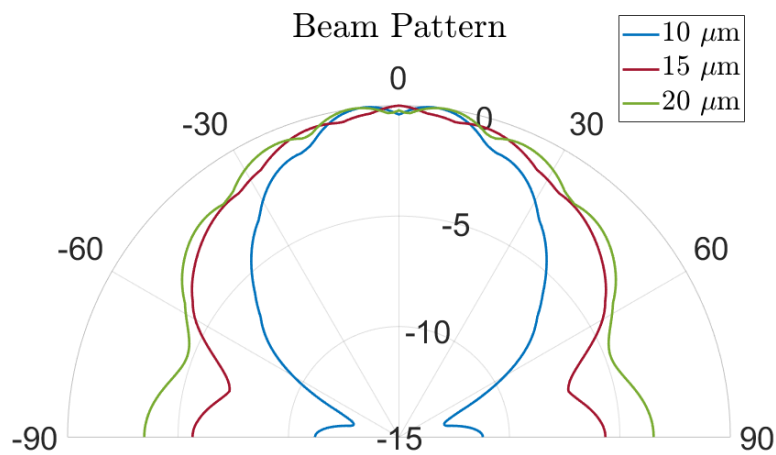


Figure 2.23: Beam pattern of array elements with different membrane geometries

2.3.5.2 Beam Focusing and Steering

The phased array geometry utilized in the analyzed CMUT array geometries enable electronic beam steering. By exciting each element in a specific time sequence, the transmitted pressure wave can be focused to a point on an azimuthal angle. Comparison of the pressure output of the arrays with single element actuation, and beam focusing to 5 mm distance for 0° and 30° can be seen in Figure 2.24. For constant aperture size, such as the case of the analyzed geometries, steering is improved with higher number of elements and smaller element pitch. This is visible at 30° focusing of the arrays, in which the 16 element 15 μm array demonstrates the minimization of grating lobes. The 12 element 10 μm and

20 μm arrays both demonstrate grating lobes around -30° . However, due to their larger equivalent element width, 10 μm arrays generate narrower beams and less energy loss to other angles. As a result, for a set element size utilization of smaller membranes result in better beam steering.

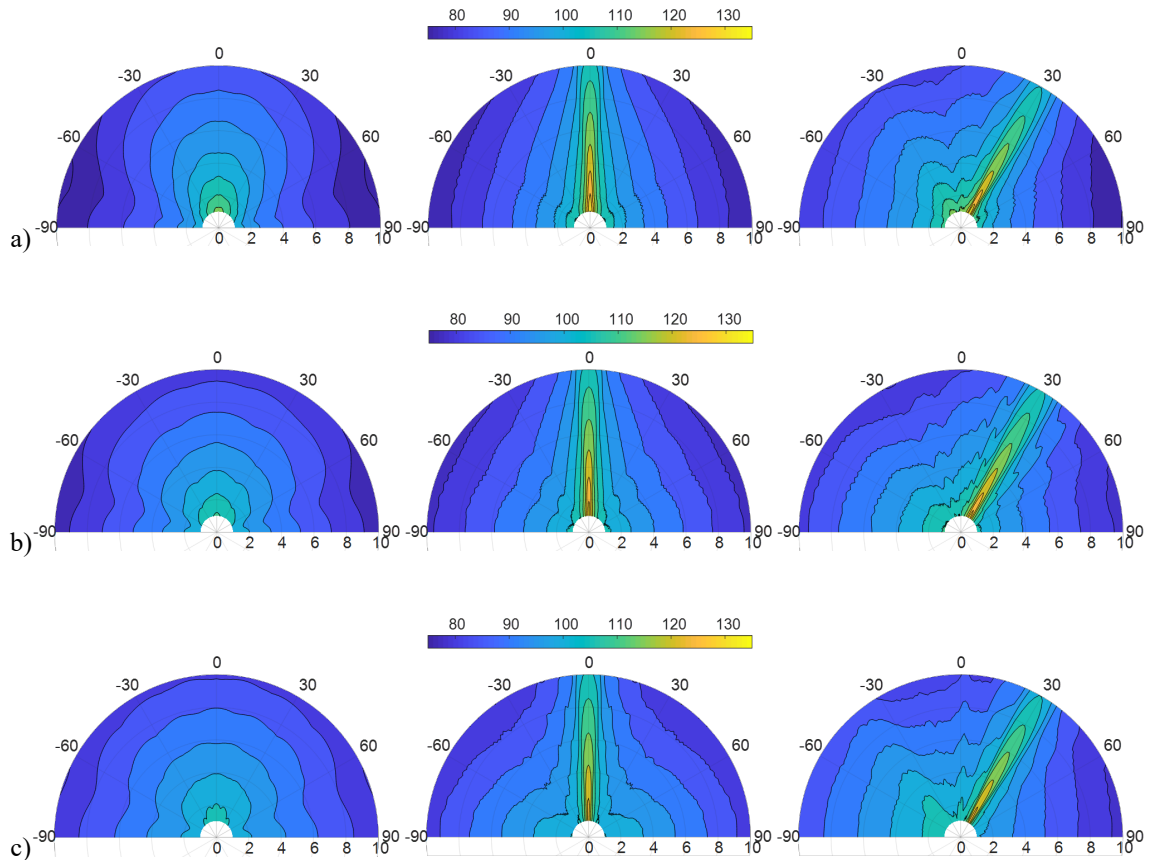


Figure 2.24: Comparison of single element actuation and beam focused pressure output for a) 10, b) 15, and c) 20 μm arrays

2.3.5.3 Angular Frequency Response

Imaging array elements radiate acoustic energy predominantly in the forward direction from the array plane. However, the constructive and destructive interference patterns generated by the bulk and evanescent waves traveling near the CMUT array

surface affect the angular frequency response of the radiated pressure at different angles. As a result, CMUT arrays can demonstrate a wide radiation angle at frequency ranges other than their operation frequency, enabling ultrasonic imaging beyond their beam pattern [84]. The frequency response of each array's far field pressure output from 0° to 90° are analyzed. The CMUT elements are actuated with a single unipolar pulse of 5 ns width to approximate impulse response. The normalized angular frequency response of each CMUT array can be seen in Figure 2.25. All arrays display narrower frequency bandwidth as the angle is increased. One main reason of this narrowing is the continuous decrease of the upper frequency limit, namely the Bragg's resonance. As mentioned in the receiver analysis, Bragg's resonance occurs at c_0/d at 0°. However, the Bragg's resonance observed in the transmitted pressure output is a function of the angle θ and can be written as:

$$f_{Bragg} = \frac{c_0}{d(1 + \sin(\theta))} \quad (2.27)$$

As a result, the upper frequency limit at 90° is half of the limit at 0°. The decrease of f_{Bragg} is especially visible in the arrays of 15 μm and 20 μm membranes where elements are composed of a single row of membranes, where in the array of 10 μm membranes, the angular effect of its asymmetric vibration mode around 90 MHz is stronger for angles below 30°. From the figure, it can be deduced that even though the 20 μm array has the highest -3dB span, the resolution will be significantly reduced at higher angles.

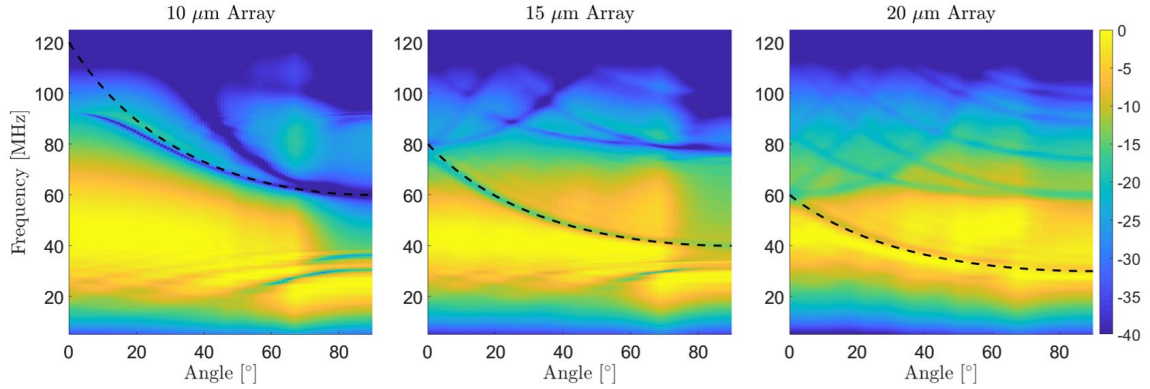


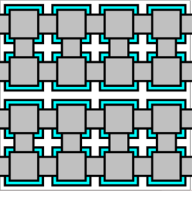
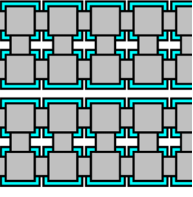
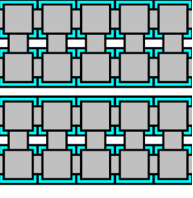
Figure 2.25: Narrowing of pressure output bandwidth with increasing angle. The angle dependent f_{Bragg} is plotted as dashed line

2.3.6. Fill Factor Analysis: Guidewire IVUS Array

The previous analysis has demonstrated that utilizing smaller membranes improve the frequency response and SNR when the fill factor is kept constant. Further analysis considering the fill factor is carried out with the same process since this is a factor easily controlled during CMUT fabrication. Three 1D CMUT arrays comprised of 10 μm membranes with different fill factors are investigated. The azimuthal pitch (d_y) is kept constant while the elevation pitch (d_x) is swept to obtain fill factors of 64, 73 and 80 %. A comparison of the array geometries can be seen in Table 2.7.

As in the previous analysis, the receiver characteristic parameters of single elements and array elements are extracted at a DC bias of 60 V and 90% collapse voltage operation. Unipolar pulsing method with 60 V pulse voltage and thermal mechanical noise limited SNR of reflection current is chosen for the pulse-echo analysis. Noise is integrated between 20 and 60 MHz and reflection current of a perfect reflector at 5 mm distance is simulated.

Table 2.7. Analyzed CMUT membrane geometries

50x50 μm^2 section	a [μm]	d_x [μm]	d_y [μm]	d_{el} [μm]	FF [%]
	10	12.5	12.5	25	64
		11			73
		10			80

2.3.6.1 Receiver Analysis

The calculated plane wave pressure sensitivity of the elements is shown in Figure 2.26. When d_x and d_y of these arrays are different, two different Bragg's resonances appear as two different cut-off frequencies (reference dips 1, 2, and 3). The two Bragg's resonances together determine the upper frequency limit, with the element geometry supporting the smallest d_x displaying the largest bandwidth. As the single membrane resonance frequency is identical, the behavior for frequencies below the center frequency is similar, with the lower frequency limit located around the single membrane resonance (reference dip 4). The fill factor mainly affects the frequency span above the center

frequency resulting in higher bandwidth and center frequency with higher fill factors. The same trend is also observed in thermal mechanical current noise and pressure noise spectrum. Therefore, the improvement of bandwidth due to increased fill factor is mainly due to higher effective Bragg resonance.

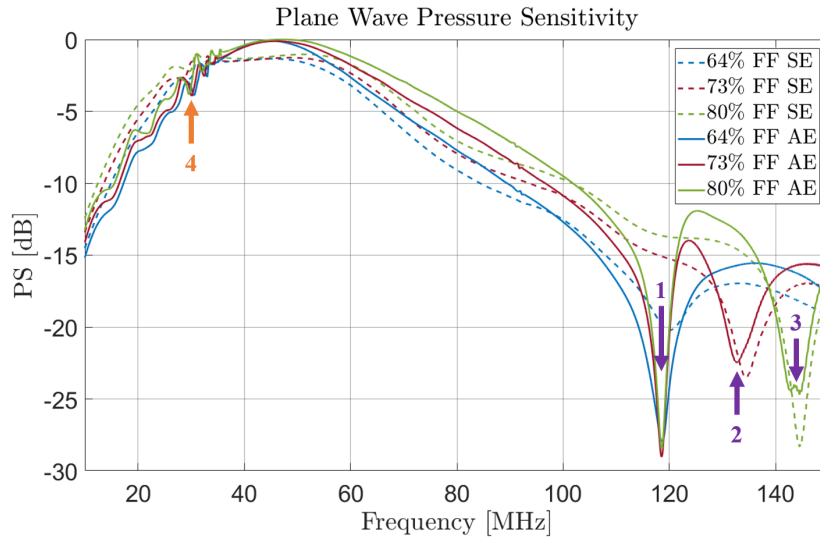


Figure 2.26: Receiver characteristics of single elements (SE) and array elements (AE) of different fill factors (FF)

2.3.6.2 Pulse-Echo Analysis

The reflection currents of the imaging array elements for 10ns pulse width can be seen in Figure 2.27. Similar to the receiver analysis, increase in bandwidth and center frequency is observed with higher fill factor. Moreover, this increase is accompanied with increased signal strength since the active area also increases. The characteristics of the reflection currents and the obtained pulse-echo SNR values of all 10 μm arrays of different FF can be found in Table 2.8.

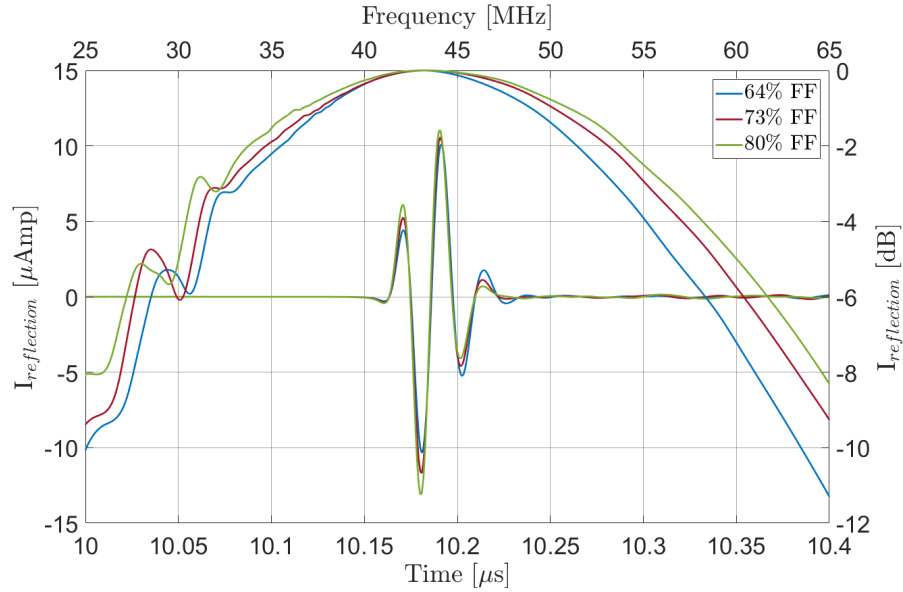


Figure 2.27: Fill factor (FF) effect on reflection current of $10\ \mu\text{m}$ membrane array elements

Table 2.8. Characteristic of reflection currents and pulse-echo SNR of $10\ \mu\text{m}$ arrays of constant element pitch and varying FF

Fill Factor [%]	f_{center} [MHz]	FBW [%]	Pulse-echo SNR [dB]
64	43.4	69	72.0
73	44.0	74	72.5
80	44.4	78	72.9

A similar analysis, in which the elevation pitch (d_x) is kept constant while the azimuthal pitch (d_y) is varied, yields similar results. An increase in fill factor results in an increase in bandwidth. However, as the element pitch (d_{el}) is defined by the azimuthal pitch (d_y), increasing the fill factor results in smaller element size, which in turn decreases

the SNR values. Nevertheless, signal strength per area increase, and an increase in fill factor is accompanied by an increase in area normalized SNR. The characteristics of the reflection currents and the obtained pulse-echo SNR values of all 10 μm arrays of different FF can be found in Table 2.9.

Table 2.9. Characteristic of reflection currents and pulse-echo SNR of 10 μm arrays of varying element pitch and varying FF

d_x [μm]	d_y [μm]	d_{el} [μm]	FF [%]	f_{center} [MHz]	FBW [%]	Pulse-echo SNR [dB]
12.5	12.5	25	64	43.4	69	72.0
12.5	11	22	73	44.6	72	70.8
11	11	22	83	45.0	79	71.2
12.5	10	20	80	45.4	73	69.8
10	10	20	100	46.8	81	70.4

2.4. Conclusion

The receiver performance and pulse-echo analysis demonstrated that high FBW operation with high SNR is feasible for high-frequency CMUT arrays with large FF s and small membrane dimensions. The analysis determined two limiting factors that dominate the frequency response of high-frequency CMUT arrays: Bragg's resonance (f_{Bragg}) as the upper frequency limit and the single membrane resonance (f_{single}) as the lower frequency limit. Therefore, for large operation bandwidth, these two limits need to be

sufficiently separated. A design process linking these limiting factors to the CMUT array geometry and performance characteristics is presented in Chapter 3.

CHAPTER 3. FREQUENCY RESPONSE LIMITING MECHANISMS AND DESIGN PROCESS

The comprehensive analysis of the multiple design parameters and their effect on performance conducted in Chapter 2 makes it possible to prioritize these parameters for a design process. Design process of CMUT arrays need to be simple and efficient to be able to navigate the large design space in a timely manner. One method of simplification is to condense the large number of design parameters into a lower number of acoustic parameters, in which optimization is carried out. Such a simplified design process has been developed by Boulme *et al* [65]. Boulme *et al* utilized normal mode theory to obtain eigenmodes of 1D CMUT array element's radiation matrix. The modes and their role in the performance of the CMUT array element is analyzed and a fundamental mode is determined as the limiting factor that dominates the frequency response of the CMUT array element. The fundamental mode is then utilized to develop a design process that links the CMUT array geometry to the frequency response and optimizes the element response in terms of bandwidth or sensitivity.

In this chapter, a similar approach to Boulme *et al* is utilized to develop a simplified design process for high frequency 1D CMUT arrays to obtain a desired pulse-echo frequency response and associated maximum SNR. The design process considers thermal mechanical current noise limited operation, i.e., the integrated transmit/receive electronics generates less or equivalent noise as compared to the CMUT imaging array element. First, the vibroacoustic frequency limiting factors observed in Chapter 2 are summarized. The frequencies of these limiting mechanisms are established as the key design parameters and

their relationship with the design parameters and CMUT performance are analyzed. Then, an algorithm is proposed to determine the lateral dimensions and membrane thickness for a desired f_{center} and FBW . A design example is provided, and the limitations of the design process is discussed. The design process is then extended to a broader frequency range and utilized to design CMUT arrays for a case study of low frequency receiver imaging devices for passive acoustic imaging.

3.1. Frequency Limiting Factors

The vibroacoustic frequency response of CMUT arrays is governed by multiple mechanisms, including dynamics of the membranes, acoustic interactions between the substrate and membranes, acoustic interactions between neighboring membranes as well as the DC bias and electrical termination. Considering the membrane and array geometry, the main frequency limiting interactions can be categorized into two phenomena: Bragg's scattering and crosstalk induced array modes [63, 85].

3.1.1. Bragg Scattering

Bragg's scattering occurs when a wave is propagating in a medium containing multiple periodic discontinuities. Destructive interference of the multiple reflections generated by these discontinuities form frequency band gaps with cut-off frequencies dependent on the medium and periodicity. Multiple membranes are positioned in periodic manner to form the elements of CMUT arrays, resulting in a limiting factor at the Bragg's resonance frequency (f_{Bragg}) of c_0/d_p , where c_0 is the speed of sound of the medium and d_p is the periodic spacing [63]. The periodic spacing d_p in question is not necessarily the spacing between membranes, but the spacing in the array in which periodicity is observed

the strongest. For instance, considering arrays with a set minimum distance d between membranes, Bragg's resonance will occur at $f_{Bragg} = c_0/d$ for square lattice arrays, and at $f_{Bragg} = c_0/(\frac{\sqrt{3}}{2}d)$ for a hexagonal lattice arrays.

3.1.2. Crosstalk Induced Array Modes

Crosstalk induced CMUT array modes are mainly generated by dispersive guided modes propagated through the fluid-solid interface [78, 80, 85-87]. These array modes form in CMUT geometries with membrane spacing below half wavelength at frequencies in the vicinity of individual vibration modes [79]. The destructive interference strength of the array modes depends on the aperture size of the CMUT element [88] and the vibration mode that has been excited. When the receiver and far-field behavior of the CMUT elements are considered, the effect of asymmetric vibration modes average out, and the effect of symmetric vibration modes dominates the frequency response. This averaging effect is also visible in the frequency response of individual membranes, in which the first symmetric vibration mode is excited around the resonance frequency (f_{single}), and the second symmetric vibration mode is excited around the antiresonance frequency (f_{ares}). As a result, the crosstalk induced frequency limit values of an array can be obtained from individual membrane simulation.

3.2. Operation Frequency Band

The frequency limits established by these two phenomena can be used to estimate the operation frequency band of the CMUT element. For CMUT array geometries of adequately thin membranes and high FF , the operation band's lower limit appears in the

vicinity of f_{single} , and the upper limit appears in the vicinity of either f_{ares} or f_{Bragg} , depending on which limit demonstrates a lower value. To illustrate the relationship between these three limiting frequencies, a case study of CMUT arrays populated with square PECVD silicon nitride (Young's modulus (E) = 110 GPa and density (ρ) = 2040 kg/m³) membranes of 15 μ m width and varying thickness is chosen. Considering water as the immersion fluid, frequency response of individual membranes and f_{Bragg} values of square lattice arrays for different FF are calculated to obtain the operation band estimation. Comparison with actual array response is carried out through the far field pressure output of CMUT arrays of 70% FF and 250 μ m x 250 μ m area. The gap of the CMUT membranes is adjusted to obtain 90% collapse voltage operation at 60 V bias. Unipolar pulsing is applied with the pulse width adjusted to coincide with the upper frequency limit and the resulting pressure output at 1 cm distance is calculated.

Two sample results are presented in Figure 3.1. For the CMUT array with 600nm thick membrane, the frequency response, shown in light green and limited by the -3dB point on the low end and the first major dip in the high end, is clearly dominated by the single membrane dynamics, as f_{Bragg} is larger than f_{ares} . When the membrane thickness is increased to 800 nm, the relationship between f_{ares} and f_{Bragg} is reversed, and Bragg's scattering determines the higher limit. The -3 dB frequency band of the pressure output is denoted as dark green shading and shown in detail in the right side of the graphs. The f_{ares} limited array demonstrates lower f_{center} and larger absolute bandwidth (BW) than the f_{Bragg} limited array, resulting in a higher FBW .

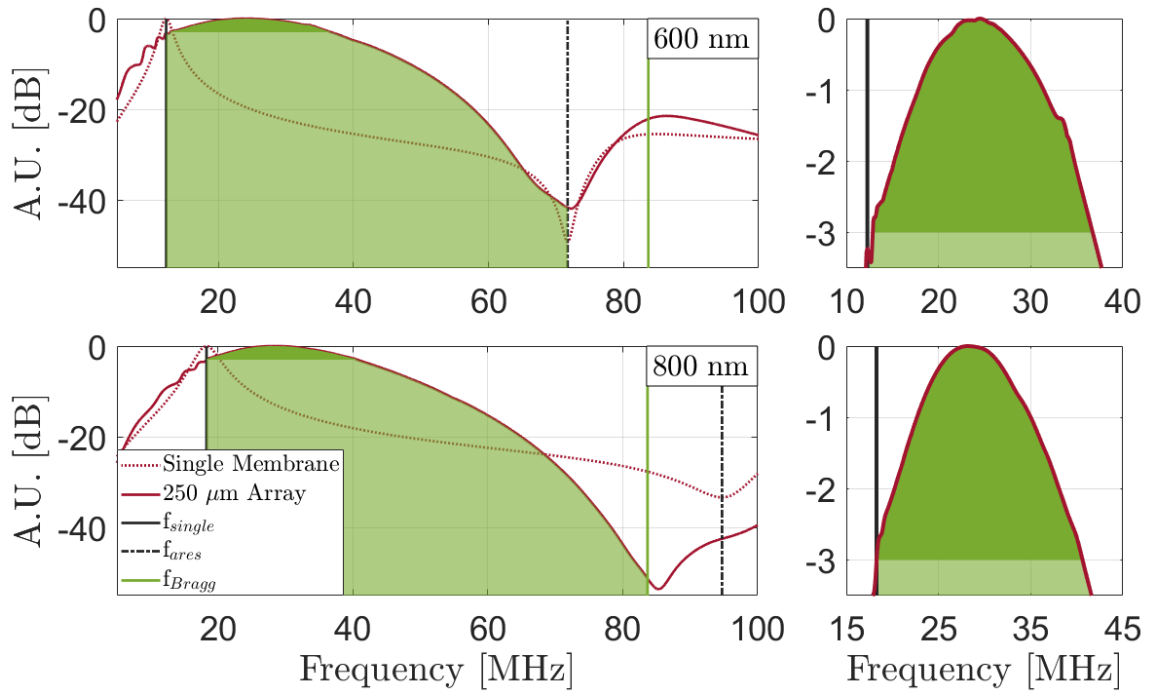


Figure 3.1: Normalized frequency response comparison of individual membranes and arrays of 600 and 800 nm thickness. Zoomed in sections of the pressure output -3 dB frequency span are visible on the right. The light shaded area illustrates operation band estimation and the dark shaded area illustrates -3dB frequency band of the pressure output.

3.2.1. Impact of Membrane Thickness

The analysis is expanded upon in Figure 3.2, where the operation band estimation of a larger range of arrays is plotted as a function of membrane thickness. The operation band estimation for 70% FF arrays is denoted as the light shaded area, and the -3 dB frequency band of the pressure output is denoted as the dark shaded area. From the figure, it is observed that as thickness increases, f_{single} and f_{aves} increase in a manner that expands the operation bandwidth, whereas f_{Bragg} remains constant. As a result, at a certain thickness value, specifically 700 nm in this case study, the upper limiting frequency shifts from f_{aves} to f_{Bragg} , leading to a reduced frequency operation band. The -3dB frequency

band of arrays follow a similar trend as the operation band estimation, with the maximum absolute bandwidth occurring when f_{ares} and f_{Bragg} have similar values. The -3dB frequency band characteristics of the arrays can be seen in Figure 3.3. f_{center} increases as thickness increases, and the shift in limiting mechanism to Bragg scattering manifests itself as increased linearity. FBW decreases as thickness increases, with a more drastic decline observed in f_{Bragg} limited operation, resulting in larger FBW when the upper frequency limit is determined by f_{ares} .

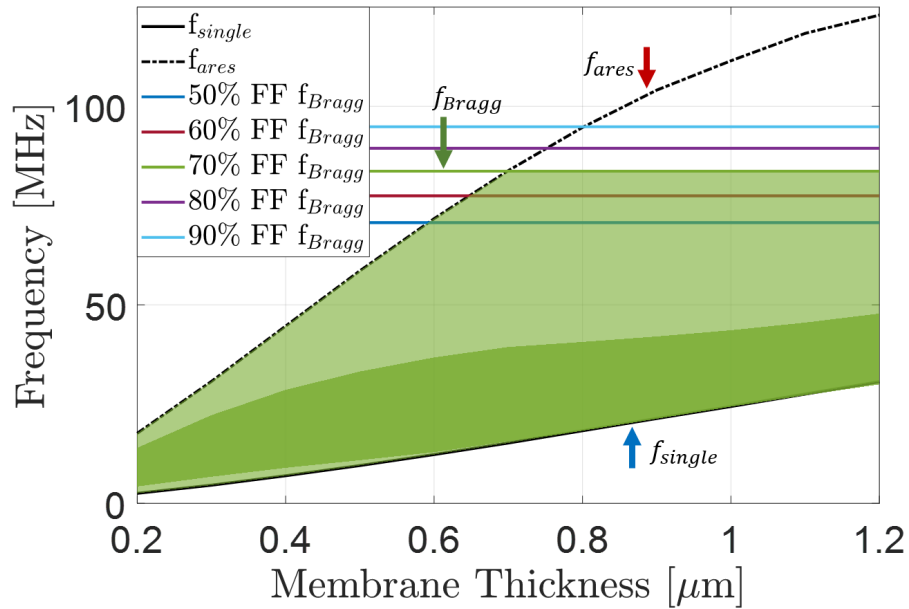


Figure 3.2: Frequency limits of 15 μm square membrane array geometries of varying thickness. The light shaded area illustrates operation band estimation for array geometries of 70% FF and the dark shaded area illustrates -3dB frequency band of the same array geometries of 250 μm x 250 μm size.

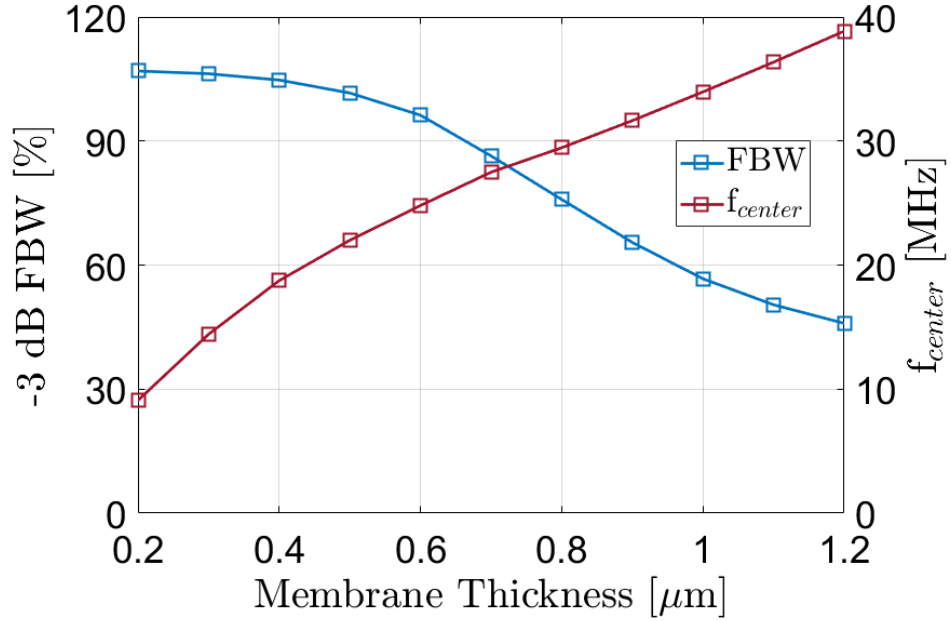


Figure 3.3: Pressure output characteristics of 250 μm x 250 μm sized 15 μm square membrane array geometries of varying thickness.

3.2.2. Impact of Membrane Aspect Ratio

Further insight on bandwidth estimation can be obtained by plotting the limiting frequencies as a function of membrane size and aspect ratio (membrane thickness (h) / width (a)). Figure 3.4 shows the single membrane resonances of square PECVD silicon nitride membranes of three specific aspect ratio and varying width, as well as the f_{Bragg} value of the corresponding 70% FF arrays. From the figure, it is seen that the upper frequency limits display similar trends, and above a specific aspect ratio array operation is f_{Bragg} limited. To take advantage of the higher FBW provided by f_{ares} limited operation, a sufficiently small h/a should be chosen first, then the membrane width of the array should be adjusted to obtain the desired f_{center} . Therefore, to obtain f_{ares} limited arrays

with high frequency operation, the membrane width and h/a need to be significantly small, making it difficult to fabricate through standard CMUT array fabrication methods while fabrication of f_{ares} limited arrays is easier for low frequency operation with sufficiently large FF and membrane width.

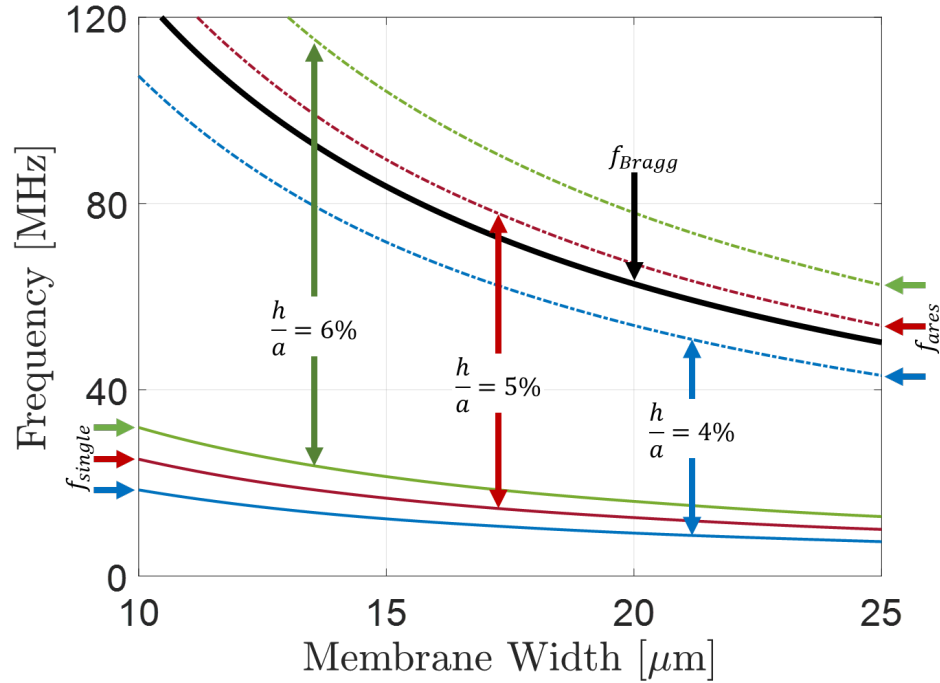


Figure 3.4: Frequency limits of square membrane array geometries of varying width and aspect ratio. The colored arrows denote the single membrane limiting frequencies and their band for different aspect ratios. The black arrow denotes the f_{Bragg} .

3.2.3. Impact of Membrane Shape and Array Lattice

Since the underlying model for the frequency limit determination is applicable to arbitrary membrane and array geometry, a comparison study has been conducted between the two most common CMUT array configurations. Single membrane resonances of square and circular CMUT membranes of varying width in water is calculated, and the thickness of the membranes are adjusted to obtain a set f_{single} value of 20MHz. These membranes

are then used to form array geometries of different FF . In a rectangular grid, circular membranes can only demonstrate a maximum FF of 79%. Therefore, to obtain comparably high FF as square membranes in a rectangular grid, circular membranes are populated in a hexagonal grid. The f_{Bragg} values of the corresponding arrays for different FF are calculated. It should be noted that, arrays comprised of circular membranes require smaller membrane spacing than those comprised of square membranes to achieve the same FF value, resulting in higher f_{Bragg} values. Moreover, due to the hexagonal grid geometry, periodicity is observed strongest at a spacing smaller than the membrane pitch ($d_p = \sqrt{3}/2 d$), further increasing its f_{Bragg} values. The resultant operation band estimation can be seen in Figure 3.5. It is observed that for a fixed single membrane resonance, if the arrays are limited by f_{ares} , utilizing circular membranes provide a larger operation band, and if the arrays are limited by f_{Bragg} , utilizing hexagonal grid geometry and higher FF provide a larger operation band.

The results presented here apply for non-collapsed CMUT operation. However, we note that similar frequency response limitations should apply to collapsed mode operated CMUT arrays and PMUT arrays in general, as it is a fundamental phenomenon due to vibroacoustics of transducer.

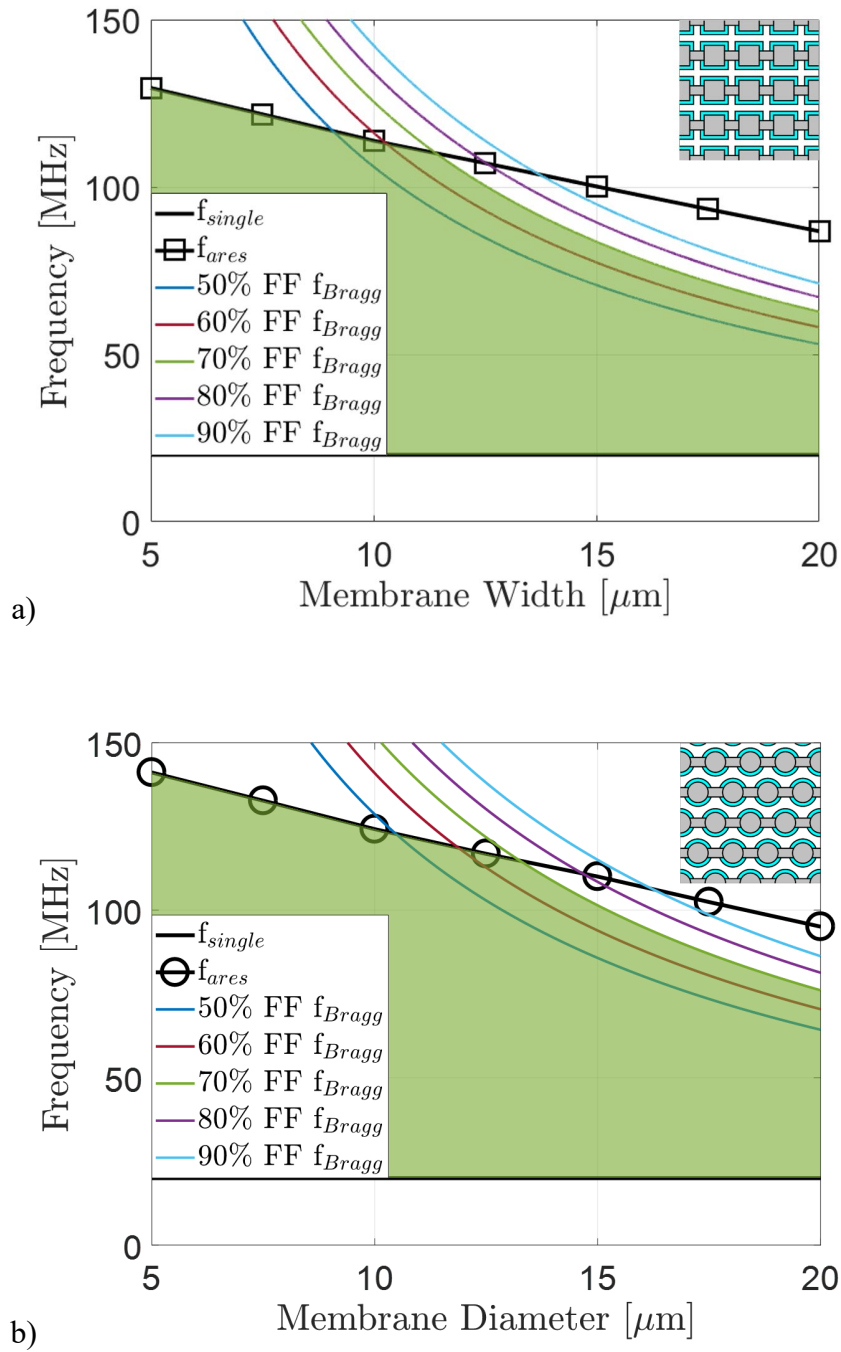


Figure 3.5: Frequency limits for a) square, and b) circular membranes of varying width. The shaded area illustrates operation band estimation for array geometries of 70% *FF*. An example of array geometries can be seen in the inset.

3.3. High Frequency CMUT Array Design Strategy

Considering that CMUT arrays operating in high frequencies are generally limited by f_{Bragg} , to obtain large operation bandwidth, the CMUT array's f_{single} and f_{Bragg} need to be sufficiently separated. To evaluate the relationship between the frequency limits f_{single} and f_{Bragg} , and the operation characteristics f_{center} and FBW , additional simulations were conducted in the design space of the guidewire IVUS arrays with membrane dimensions ranging from 7.5 to 20 μm and different FFs . The characteristics of the additional array geometries and their pulse-echo responses can be found in Table 3.1. The relationship between the BW and the average f_{Bragg} is investigated, where the average f_{Bragg} is defined as:

$$f_{Bragg_ave} = 0.5 \times \left(\frac{c_0}{d_x} + \frac{c_0}{d_y} \right) \quad (3.1)$$

When the BW versus f_{Bragg_ave} is plotted as shown in Figure 3.6, a linear relationship in the form of $BW \sim f_{Bragg_ave}/4$ is observed. The linear dependence arises from the fact that f_{single} displays a similar value in the array geometries. When f_{single} is fixed to a constant value determining the lower frequency limit, BW is determined by slope of the frequency response above the f_{center} which is in turn determined by f_{Bragg_ave} . Note that this BW estimation loses accuracy as f_{Bragg_ave} approaches f_{center} , where the Bragg resonance and single membrane resonance effects cannot be isolated.

Table 3.1. Characteristic of reflection currents and pulse-echo SNR of additional simulated arrays of varying element pitch and varying FF

a [μm]	d_{el} [μm]	FF [%]	f_{center} [MHz]	FBW [%]	Pulse-echo SNR [dB]
7.5	18.75	64	42.1	90	66.9
8.75	21.88	64	40.2	82	68.8
15	18.75	73	42.7	48	69.0
15	18.75	80	43.2	52	69.5
20	25	73	44.9	29	71.2
20	25	80	45.4	14.23	71.6

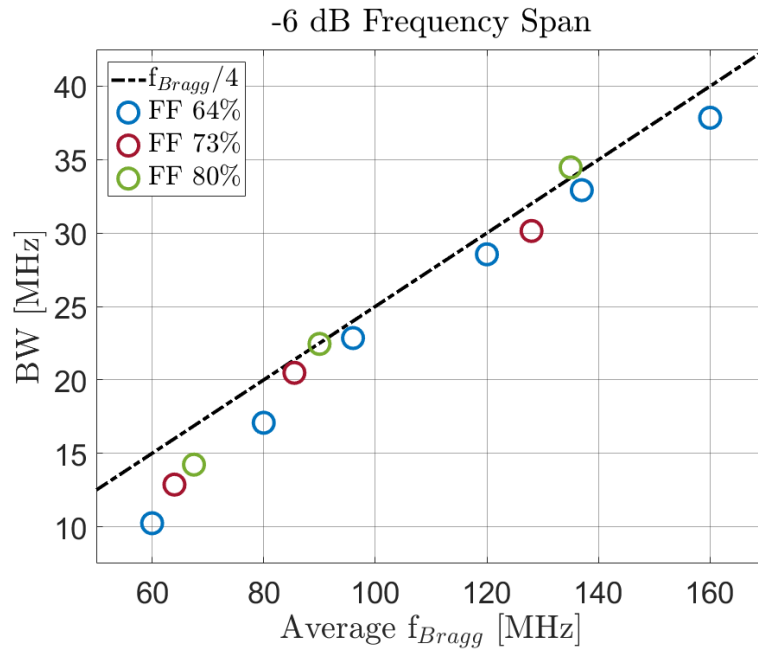


Figure 3.6: -6-dB frequency span (BW) relation with f_{Bragg_ave} .

3.3.1. Design Process Algorithm

Taking the frequency limits of the CMUT array and their mechanisms into consideration, an algorithm can now be proposed to determine the lateral dimensions and membrane thickness for a desired f_{center} and FBW . This is depicted in Figure 3.7. As the first step, the frequency limits (f_{low} , f_{high}) are determined for a 1D CMUT array operating at a center frequency of f_{center} and a fractional bandwidth of FBW . For large FBW and f_{Bragg} limited operation, f_{Bragg} can then be determined from the frequency span. f_{Bragg} and f_{center} are then used to determine the membrane and element pitch (d , d_{el}). At this point, it is important to check if the calculated f_{Bragg} is larger than f_{high} . If $f_{Bragg} < f_{high}$, the pitch has to be decreased to ensure the validity of f_{high} . If d and f_{Bragg} are reasonable, membrane lateral dimensions maximizing the fill factor are chosen. The thickness of the membrane (h) is then set to obtain a f_{single} close to f_{low} . While setting the thickness, one needs to check that $f_{ares} > f_{Bragg}$ holds to make sure that f_{Bragg} is still the limiting factor.

After the lateral dimensions and thickness is determined, the gap thickness (g) can be chosen. For thermal mechanical current noise limited operation, it is observed that the receiver performance is independent of the DC bias and gap thickness. However, a realistic device integrated with transmit/receive electronics would still require operation close to collapse to increase the signal levels. This limitation makes the maximum available voltage the main limiting factor. For unipolar pulsing, gap thickness is chosen to have close to collapse operation at the maximum available voltage. For bipolar pulsing, DC bias voltage is lower than the maximum available voltage and a smaller gap thickness can be chosen [82]. Smaller membranes require thinner thickness values, enabling larger gap thicknesses

for the same operation voltage. As a result, an increase in SNR in addition to the increased bandwidth can be obtained by utilizing smaller membrane geometries.

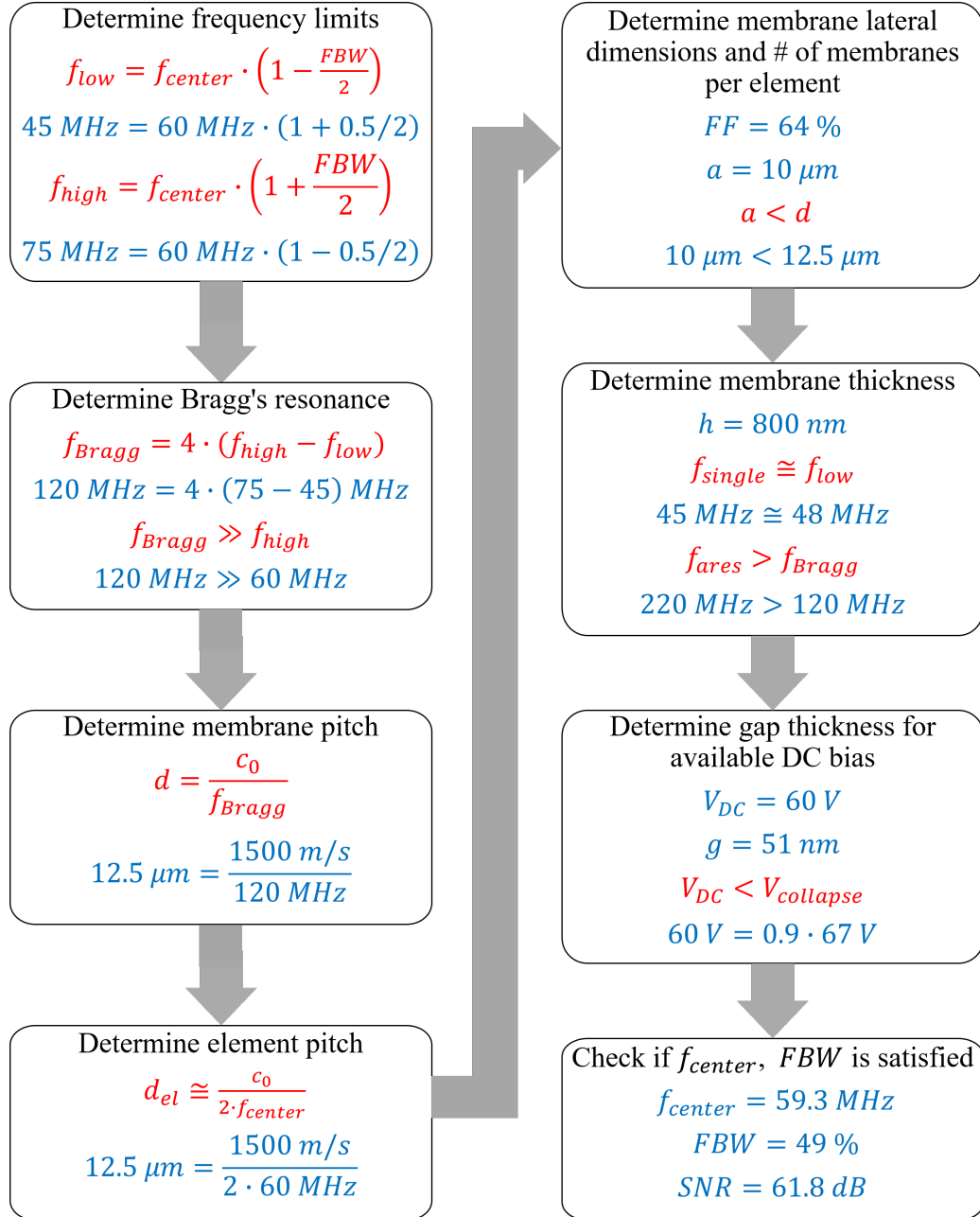


Figure 3.7: Design algorithm for 1D high frequency imaging array of $f_{center} = 60 \text{ MHz}$ and $FBW = 50\%$.

3.3.2. Design Process Example

To illustrate the design process, design of a 1D CMUT imaging array with a center frequency of $f_{center} = 60 \text{ MHz}$ and a fractional bandwidth of $FBW = 50\%$ is considered. Similar to the analyzed geometries, a fill factor of 64%, and electrode coverage of 56% is chosen. Assuming 60 V operation with unipolar pulsing, the V_{col} is chosen to be 67 V, to operate at 90% of collapse. The details of the design process of this array can be seen in Figure 3.7 (shown in blue). The resulting parameters shown in the last box in Figure 3.7 indicate that the center frequency and fractional bandwidth requirements are satisfied. The pulse-echo response of the designed CMUT array from a perfect reflector at 5 mm distance and 6.7 ns unipolar pulse can be seen in Figure 3.8.

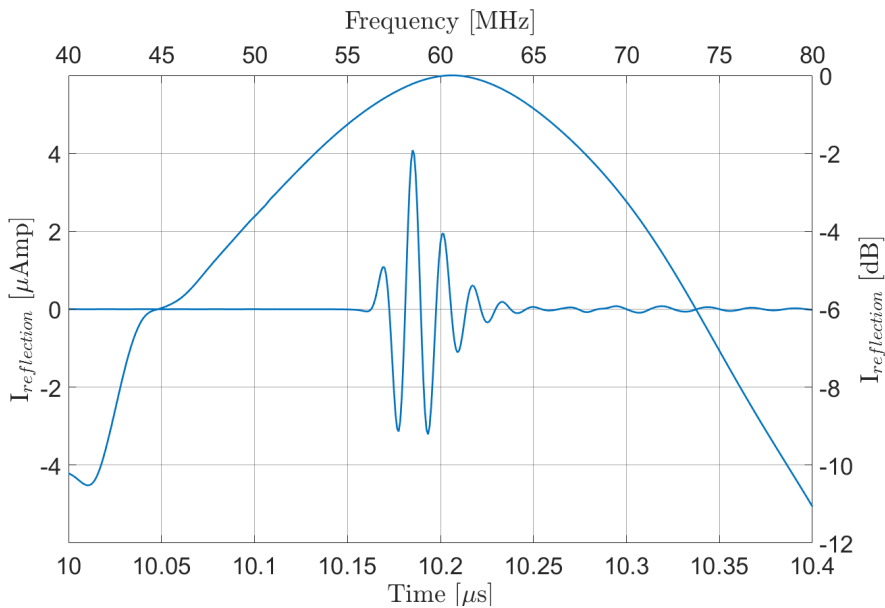


Figure 3.8: Reflection current of imaging array element determined from the design process.

3.3.3. Design Process Limitations

The foregoing design process has its limitations in terms of practicality. As noted above, while determining the membrane thickness, the membrane f_{ares} needs to be considered to ensure that f_{Bragg} is the limiting factor. To illustrate the effect of this limitation, the SNR (normalized to element area) and BW for the CMUT arrays as a function of membrane width is plotted in Figure 3.9. All CMUT arrays have 40MHz center frequency and 64% fill factor, resulting in f_{ares} and f_{Bragg} crossing over around membrane width of 8.5 μm . When $f_{ares} < f_{Bragg}$, the -6 dB frequency span estimation diverges from $f_{Bragg}/4$. While the bandwidth still increases (beyond 100% FBW shown by the dashed line), the slope is smaller. Our simulations show that for high frequency arrays operating around 30 MHz and above, this condition is encountered when membrane thickness needs to be reduced to below 500 nm. This value is close to the CMUT fabrication limit. Therefore, for practical high frequency CMUT arrays, the proposed design guidelines based on f_{Bragg} are valid and can achieve nearly 100% FBW. Also, it should be noted that the area normalized SNR achieved in the f_{ares} limited region is lower indicating a SNR-bandwidth compromise for high frequency CMUT arrays. A similar tradeoff between bandwidth and sensitivity has been demonstrated by Boulme *et al* [65] and Hery *et al* [67] for lower operation frequencies.

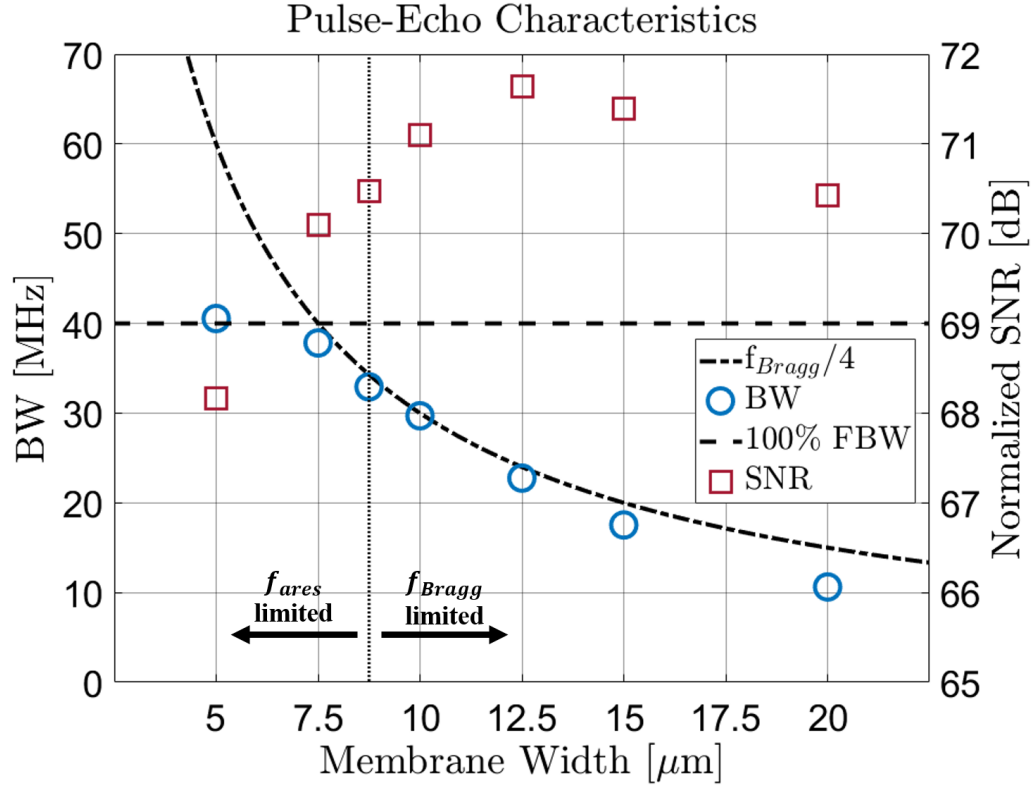


Figure 3.9: Pulse-echo characteristics of f_{Bragg} and f_{ares} limited arrays. The element pitch varies between 15.6 μm and 25 μm and SNR is normalized to element area.

Although the design process here focused on phased array operation with array element pitch close to half wavelength, the design guidelines for bandwidth limits are also valid for larger array elements suitable for linear 1D arrays. Overall, for larger elements the bandwidth remains the same as it is dominated by the membrane pitch within the element and single membrane dynamics but the beamwidth is reduced. The reflector distance utilized in the analysis and design process was significantly larger than the array dimensions, resulting in far field operation. In the near field, the effect of the asymmetric vibration modes is more prominent which may impact the predicted bandwidth.

3.3.4. Design Strategy Extension to Broader Frequency Range

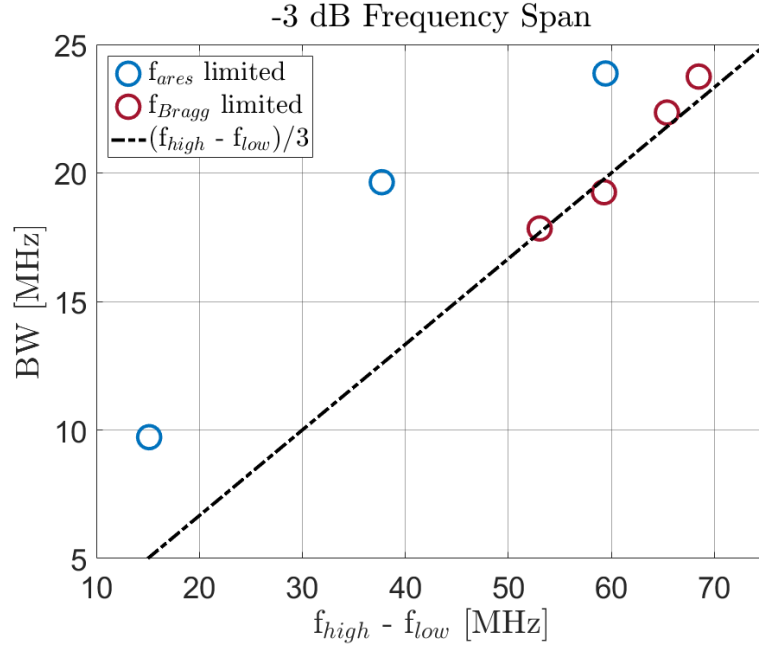


Figure 3.10: -3dB frequency span (BW) relation with $(f_{high} - f_{low})$.

Considering that the BW estimation $f_{Bragg}/4$ is insufficient for f_{ares} limited arrays, a different design strategy is required for CMUT arrays operating in lower frequencies. To evaluate the relationship between the frequency limits and operation characteristics across a broad frequency range, the $15\ \mu\text{m}$ square membrane array geometries discussed in Section 3.2.1 are analyzed. When the -3dB BW of the pressure output versus the operation band estimation $(f_{high} - f_{low})$ is plotted, as shown in Figure 3.10, a linear relationship in the form of $BW \sim (f_{high} - f_{low})/3$ is observed in the f_{Bragg} limited array geometries. This linear relationship corresponds to a linear approximation to frequency response, in which f_{low} corresponds to -3dB and f_{high} corresponds to -15dB decrease in the normalized response. In the f_{ares} limited array geometries it is observed

that $(f_{high} - f_{low})/3$ underestimates the BW , with the amount of error increasing as the difference between f_{ares} and f_{Bragg} increases.

A BW estimation range can then be established for f_{ares} limited array geometries. Assuming the mechanisms of f_{high} and f_{low} are isolated from each other, the lower limit of BW is set as $(f_{high} - f_{low})/3$ and the upper limit is set as $(f_{high} - f_{low})$. The position of BW in this range would then be determined by how separated the f_{ares} and f_{Bragg} are. Considering the SNR-bandwidth compromise observed in CMUT arrays, an array geometry with $f_{ares} \ll f_{Bragg}$ will provide a larger BW but a smaller SNR, whereas an array geometry with $f_{ares} \cong f_{Bragg}$ will provide a BW close to the lower limit but a larger SNR. Considering the design guidelines proposed by Boulme *et al* [65] an appropriate ratio between f_{ares} and f_{Bragg} would be between 70% to 85% for broadband operation, and between 85% to 100% for higher sensitivity.

Taking the change in relationship between the frequency limits and the operation characteristics into consideration, the f_{Bragg} limited arrays design algorithm can be modified for f_{ares} limited CMUT arrays. The initial steps of the previous algorithm are used to calculate the minimum f_{Bragg} and the corresponding maximum membrane pitch (d) value that can be used for the array. Depending on the desired type of array operation (broadband or high SNR), d is then reduced up to 30%. Membrane lateral dimensions maximizing the fill factor are then chosen, and the thickness of the membrane (h) is then set to obtain a f_{single} close to f_{low} . It should be noted that as f_{ares} and f_{Bragg} are separated, the amount of crosstalk observed within the CMUT array increases, resulting in a shift of f_{low} to higher frequencies. As a result, a f_{single} lower than the desired f_{low} can

also be chosen. While setting the thickness, one needs to check that $f_{ares} < f_{Bragg}$ holds to make sure that f_{ares} is still the limiting factor, and $f_{ares} > f_{high}$ to ensure the frequency limits are within the operation band.

3.4. Case Study: Passive Acoustic Imaging Array

High intensity focused ultrasound (HIFU) is a low frequency ultrasound application that utilizes focused ultrasound waves to locally deposit high levels of energy deep in the soft tissue. The increase in pressure at the focal point can be used to thermally ablate a portion of the tissue or induce acoustic cavitation, i.e. the stable or inertial oscillations of microbubbles. Acoustic cavitation has been utilized in a multitude of therapies, such as lithotripsy of kidney stones [89], blood clot dissolution [90], and permeabilization of vascular or cellular barriers for drug delivery [91]. The level of thermal and mechanical mechanisms activated in the tissue is dependent on the acoustic characteristics of the system. As a result, the desired temperature rise or level of cavitation activity can be controlled by tuning the transmitted pressure wave. However, to ensure a safe and effective treatment, it is critical that the precise position of the HIFU induced heating and cavitation activity is known.

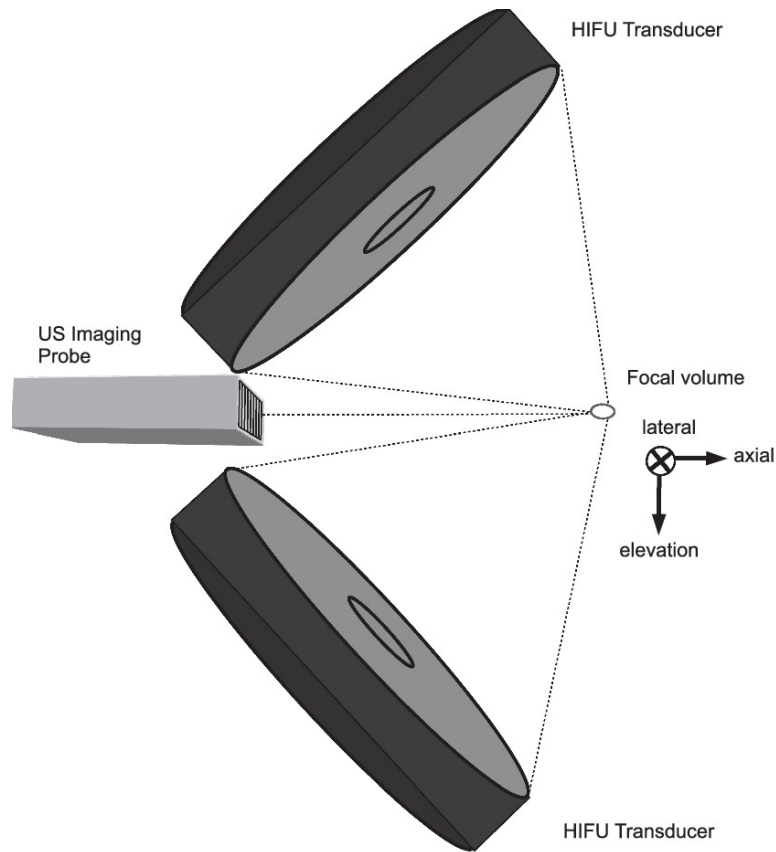


Figure 3.11: Dual HIFU transducer and diagnostic imaging array geometry [92].

The acoustic emission produced by the microbubbles in the focal point can be used for monitoring with the use of a passive acoustic imaging array. A schematic of a passive imaging array integrated dual HIFU transducers can be seen in Figure 3.11. The frequency content of the emissions can be used to verify the presence of cavitation, as well as determine the mode of oscillation. Strong emissions at harmonics, including subharmonics and ultra-harmonics, of the HIFU operation frequency are generally associated with stable cavitation, whereas broadband emissions are associated with inertial cavitation [93]. An example of the cavitation activity power spectra can be seen in Figure 3.12. As a result, to effectively monitor the cavitation activity, the passive imaging arrays needs to be able to operate in a broad frequency range.

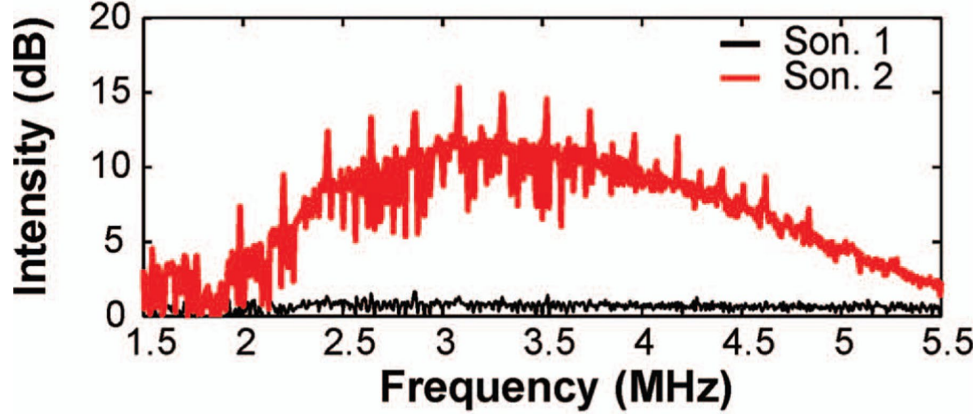


Figure 3.12: Power spectra of cavitation activity during two sonifications [93].

3.4.1. Design Constraints

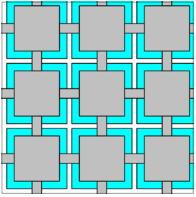
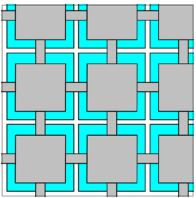
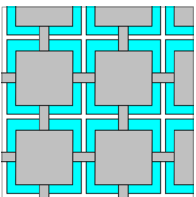
Considering a standard HIFU transducer operating at 0.5 MHz, a passive acoustic imaging operation frequency band from 0.5 to 5 MHz, similar to the bandwidth of acquisition supplied by Arvanitis *et al* [93], is chosen. Unlike the guidewire IVUS system, the passive acoustic imaging array size is not a limiting factor, and total array size is chosen to be $750 \times 2750 \mu\text{m}^2$. To maximize bandwidth, aperture is maximized by considering single element operation.

3.4.2. Array Design

For frequency limits of $f_{low} = 0.5 \text{ MHz}$ and $f_{high} = 5 \text{ MHz}$, the minimum Bragg resonance is $f_{Bragg} = (5 - 0.5) \times 4 = 18 \text{ MHz}$, corresponding to a maximum membrane pitch of $d = 1500/18 \cong 83 \mu\text{m}$. Considering a minimum spacing of $5 \mu\text{m}$ between membranes, the three array geometries seen in Table 3.2 can then be formed by reducing d by 20%, 10%, and 0%. The thickness can then be adjusted to obtain f_{single} and f_{ares} values in agreement with the desired operation band. The gap can then be adjusted for a

desired V_{col} , which is chosen as 20 V for this case study. The plane wave pressure sensitivity and pressure noise spectrum of the designed CMUT arrays can be seen in Figure 3.13, in which broadband sensitivity is observed between 0.75 and 5 MHz with minimum detectable pressure levels.

Table 3.2. Analyzed CMUT membrane geometries.

200x200 μm^2 section	a [μm]	d [μm]	h [μm]	f_{Bragg} [MHz]	f_{single} [MHz]	f_{ares} [μm]
	63	68	1.0	22	0.76	5.20
	70	75	1.2	20	0.75	5.20
	78	83	1.4	18	0.74	4.96

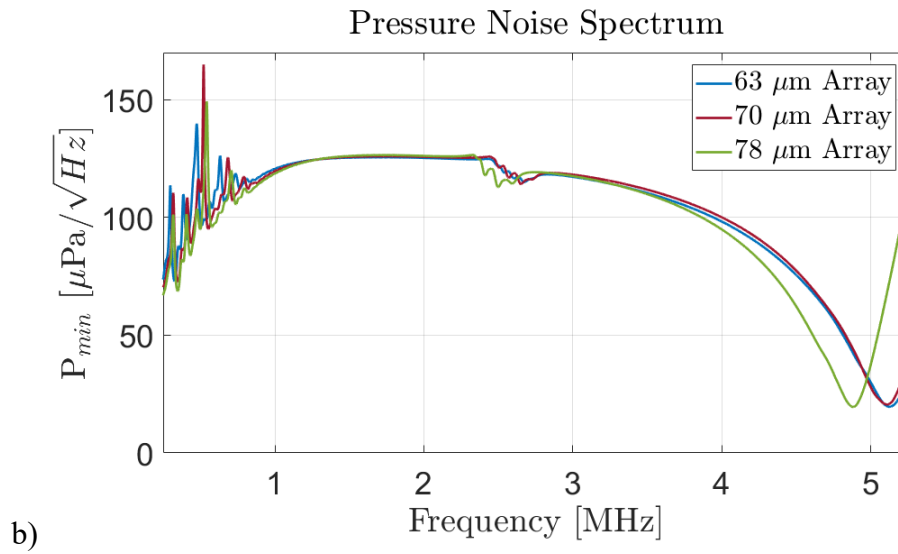
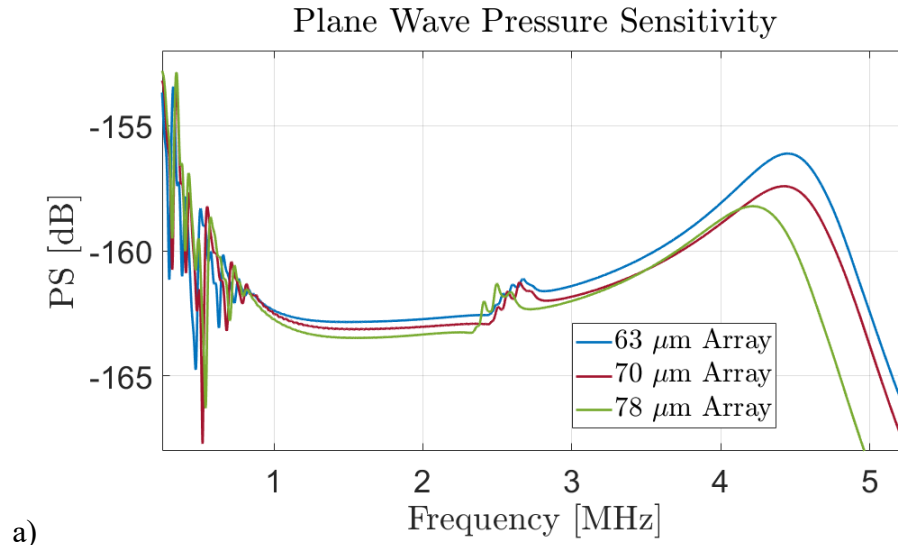


Figure 3.13: a) Plane wave pressure sensitivity (PS) and b) pressure noise spectrum (p_{min}) of designed array elements

CHAPTER 4. DEVICE FABRICATION AND EXPERIMENTAL VALIDATION

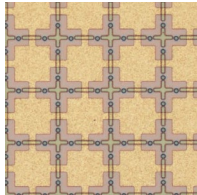
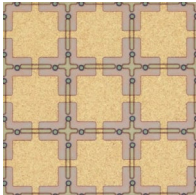
This chapter utilizes experimental methods to verify the frequency limiting mechanisms and design process discussed in Chapter 3. CMUT arrays with two different upper frequency limiting mechanisms are designed and fabricated to experimentally test the validity of these limiting phenomena. As mentioned in Chapter 3, among the two upper frequency limiting mechanisms, f_{ares} is dependent on the CMUT membrane's lateral and vertical dimensions, whereas f_{Bragg} is dependent only on the lateral dimensions and the specific upper frequency limit can be estimated from the aspect ratio of the CMUT membrane. Correspondingly, CMUT arrays with low aspect ratio membranes for low frequency operation are designed to analyze the f_{ares} limited arrays, and CMUT arrays with high aspect ratio for high frequency operation are designed to analyze the f_{Bragg} limited arrays, enabling experimental validation in a broad frequency range, from 1 to 80 MHz. In consideration with their operation frequencies, the two set of CMUT arrays are fabricated separately using modified versions of the CMUT-on-CMOS technology developed by Zahorian [94]. The CMUT arrays' pressure output and admittance measurements in comparison with simulations are utilized to validate the limiting mechanisms. Frequency limiting mechanisms are further isolated with the use of immersion fluids with different sound speeds. Finally, an array geometry from guidewire IVUS case study is fabricated and integrated to an application-specific integrated circuit (ASIC) with transmitter and receiver electronics. Performance of the ultrasonic imaging

system as a transmitter, receiver, and full system is analyzed through pressure output, pitch-catch, and pulse-echo measurements.

4.1. Arrays Limited by Single Membrane Dynamics

Two single element array geometries designed in the passive acoustic imaging array case study are chosen for f_{ares} limited operation analysis. An area of 2.8 mm x 0.8 mm is populated with silicon nitride (Young's modulus (E) = 110 GPa, density (ρ) = 2040 kg/m³) square membranes of two different lateral dimensions: 63 and 78 μ m. Electrodes made of aluminum (E = 70 GPa, ρ = 2700 kg/m³) are positioned on top of the membranes for maximum isolation thickness and electrode coverage is kept constant at 56%. A final layer of Parylene-C (E = 2.76 GPa, ρ = 1289 kg/m³) is deposited to electrically isolate the arrays. The elevation and azimuthal membrane spacing is kept constant at 5 μ m, resulting in varying membrane pitches and slightly different FF . Arrays are fabricated on the same wafer and therefore have the same membrane and gap thickness. Limiting frequencies of the arrays are calculated considering water as the immersion fluid (c_0 = 1500 m/s, ρ = 1000 kg/m³). As the aluminum and Parylene-C thickness is comparable to the silicon nitride thickness, calculation is done with the CMUT model incorporating static FEA for stiffness matrix calculation [64]. A comparison of the array geometries and their limiting frequencies at 75% collapse voltage can be seen in Table 4.1. Calculated f_{ares} values are considerably lower than the f_{Bragg} values in both arrays, determining crosstalk induced array modes of the second symmetric vibration mode as the frequency limiting mechanism.

Table 4.1. f_{ares} limited array properties and limiting factor frequencies

250x250 μm^2 section		
Membrane width [μm]	63	78
Membrane pitch [μm]	68	83
Silicon nitride thickness [μm]	1.5	
Electrode thickness [μm]	0.4	
Parylene-C thickness [μm]	3.0	
Gap thickness [nm]	275	
Fill factor [%]	86	88
Aspect ratio [%]	2.4	1.9
f_{single} [MHz]	2.24	1.36
f_{ares} [MHz]	11.74	8.00
f_{Bragg} [MHz]	22.06	18.07

4.1.1. Low Frequency CMUT Array Fabrication

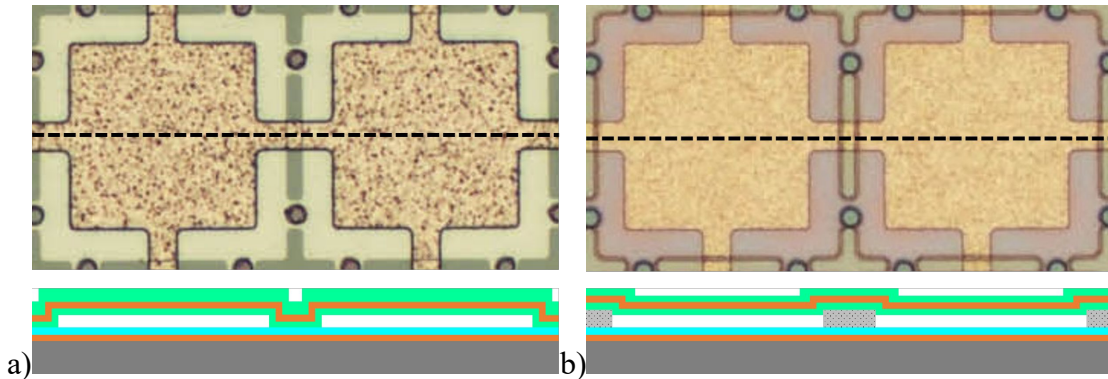


Figure 4.1: a) Cross section of a conventional surface micromachined CMUT with thin isolation layer over TE-BE overlap area. b) Cross section of CMUT with the extra layer of dielectric deposited over TE-BE overlap area.

A modified version of the fabrication method described by Pirouz *et al.* [95] is utilized for f_{ares} limited CMUT array fabrication. As seen in Figure 4.1(a), CMUT arrays fabricated with sacrificial layer technique have a thin layer of isolation separating the top electrode (TE) and the bottom electrode (BE) over the vacuum gap. During operation a high electric field is generated over the vacuum gap and isolation layer. Ideally, this high electric field should only exist over the membrane of the CMUT vibrating over the vacuum gap, but the electrical interconnections between CMUT cells also pass over the thin dielectric isolation layers. The resulting high electric fields on the thin isolation layer at these interconnections cause charging, dielectric breakdown, and increase parasitic elements. Pirouz *et al.* proposed introduction of a self-aligned lift-off step to the process flow, in which a thick dielectric layer is deposited between the TE and BE except for the sacrificial layer as seen in Figure 4.1(b). The simple addition of the additional dielectric layer reduced the electric field in unwanted areas without affecting the vacuum gap thickness, improving reliability and reducing parasitic capacitance.

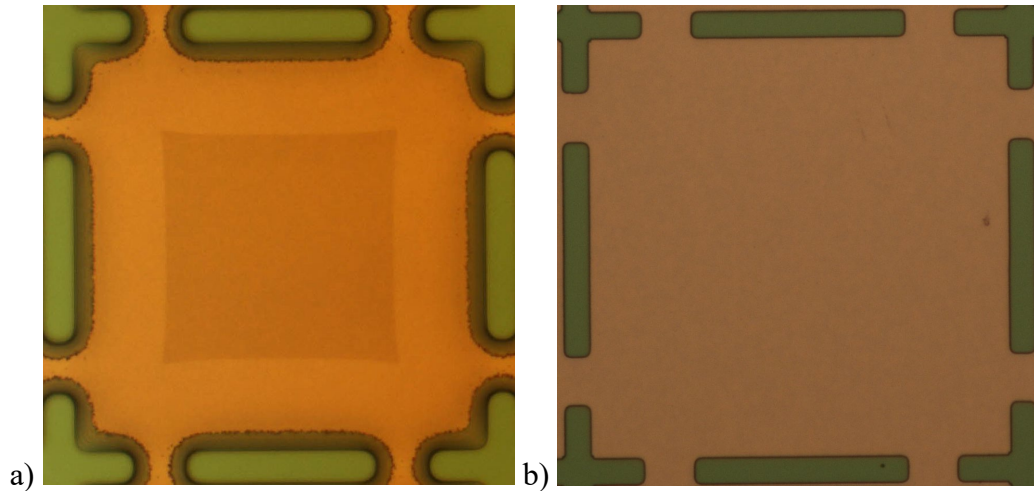


Figure 4.2: Sacrificial layer patterning with a) wet etching and over etching and b) lift-off without over etching.

Details of the fabrication process utilized in fabrication of f_{ares} limited CMUT arrays is shown in Figure 4.3. Starting with a 4" $\langle 100 \rangle$ silicon wafer with 3 μm thermal oxide, chromium of 360 nm thickness is sputtered and patterned to form the BE of the CMUT arrays. A 275 nm PECVD oxide layer is deposited and patterned with negative photoresist. The PECVD oxide is etched via anisotropic reactive ion etching (RIE) to the chromium BE. Without doing a photoresist strip, 275 nm of copper is evaporated on the wafer and lift-off is carried out to establish the sacrificial layer. The benefit of a copper lift-off process is the avoidance of wet etching in patterning of the sacrificial layer, which is harder to control and can cause over etching. An example of wet etched sacrificial layer with over etching in comparison with a sacrificial layer fabricated through lift-off can be seen in Figure 4.2. Over etching should especially be avoided if the CMUT membrane dimensions are small and therefore especially susceptible to variations in membrane geometry. Copper is chosen as the sacrificial layer as it can be etched very selectively with

chromium and silicon nitride, removing the need for an additional passivation layer between BE and sacrificial layer.

Low stress PECVD silicon nitride is deposited as the membrane and isolation layer. The TE is not embedded in the membrane to maximize isolation and reliability. Deposition of silicon nitride is carried out in two steps. After an initial deposition of 450 nm thickness, etch holes are patterned and etched via RIE to reach the sacrificial layer. The wafer is immersed in copper etchant APS 100 to etch the sacrificial layer. As the TE has not been patterned removal of the sacrificial layer can be easily monitored. The wafer is rinsed 4-5 times in water to remove any copper residues and dipped in isopropyl alcohol (IPA) overnight. As the gap thickness of the arrays are larger than 100 nm, the sample is dried in an oven with temperature of about 85-90°C for about 1 hour. 1050 nm of silicon nitride is deposited to seal the membranes and reach the desired membrane thickness. The TE is then formed by sputtering a 400 nm of aluminum silica (AlSi 1%) and photolithography. Finally, connection to the BE is obtained by patterning the bond pads and etching the silicon nitride layer via RIE. All mentioned process steps are carried out at temperatures below 250°C, indicating compatibility with CMOS wafers.

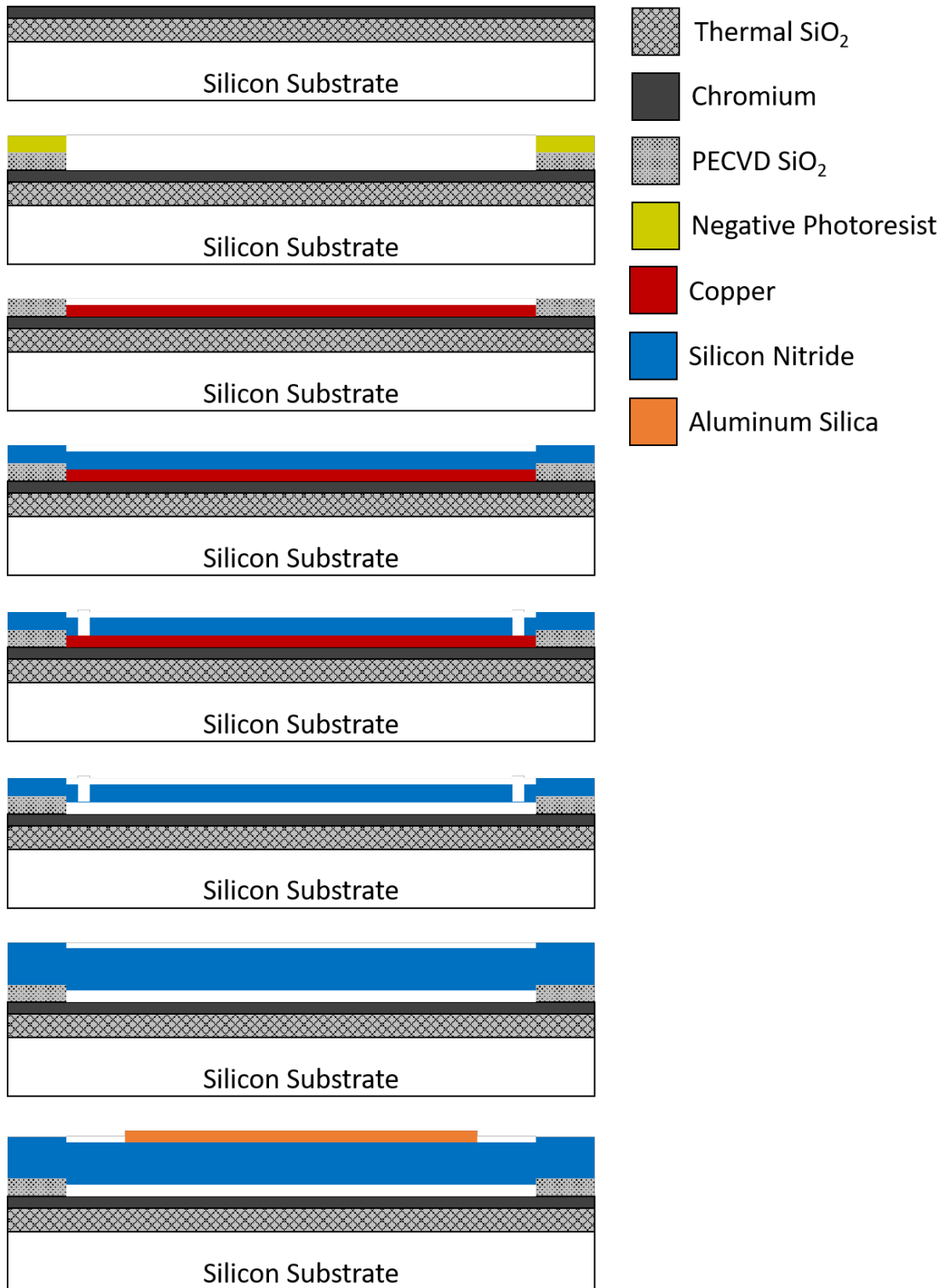
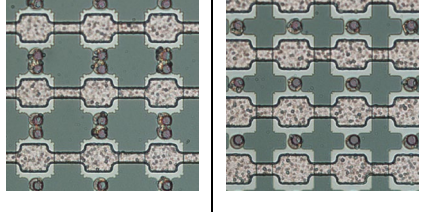


Figure 4.3: Schematic of fabrication process flow of f_{ares} limited CMUT arrays

4.2. Arrays Limited by Bragg Scattering

Table 4.2. f_{Bragg} limited array properties and limiting factor frequencies

75x75 μm^2 section		
Membrane width [μm]	15	
Membrane pitch [μm]	25.00	21.36
Hafnium oxide thickness [μm]	0.3	
Silicon nitride thickness [μm]	1.0	
Electrode thickness [μm]	0.3	
Parylene-C thickness [μm]	2.0	
Gap thickness [nm]	80	
Fill factor [%]	36	49
Aspect ratio [%]	8.7	
f_{single} [MHz]	32.42	
f_{ares} [MHz]	121.5	
f_{Bragg} [MHz]	60	70.22

Two single element array geometries are designed for f_{Bragg} limited operation analysis. An area of $250\ \mu\text{m} \times 250\ \mu\text{m}$ is populated with silicon nitride square membranes of $15\ \mu\text{m}$ width and two different membrane pitches: 25 and $21.36\ \mu\text{m}$, resulting in 39% and 49% FF , respectively. Electrodes are embedded in the membranes with an isolation layer of hafnium oxide ($E = 160\ \text{GPa}$, $\rho = 9700\ \text{kg/m}^3$) to reduce the collapse voltage. Similar to the f_{ares} limited arrays, electrode coverage is kept constant at 56% and a final layer of Parylene-C is deposited to electrically isolate the arrays. Arrays are fabricated together, and the limiting frequencies are calculated with the FEA incorporated CMUT model considering water as the immersion fluid. A comparison of the array geometries and their limiting frequencies at 90% collapse voltage can be seen in Table 4.2. The calculated f_{Bragg} values are considerably lower than the f_{ares} values in both arrays, determining Bragg scattering as the frequency limiting mechanism.

4.2.1. High Frequency CMUT Array Fabrication

A modified version of the fabrication method described by Xu *et al.* [76] is utilized for f_{Bragg} limited CMUT array fabrication. Unlike the low frequency f_{ares} limited arrays, high frequency CMUT arrays require significantly smaller gap thicknesses to effectively operate within feasible bias voltages. In CMUT arrays of small gap thickness, the choice of dielectric isolation layer material becomes a significant factor in determining the electromechanical performance of the CMUT. To maximize the electromechanical coupling factor, the applied DC bias should be close to the collapse voltage of the CMUT. The collapse voltage is determined by the effective gap of the CMUT, which is dependent on the vacuum gap thickness, isolation layer thickness, and its relative permittivity. For a

set effective gap, the SNR of the CMUT array proportional to the vacuum gap thickness. Ideally, SNR at a given applied voltage can be maximized by removing the isolation layer and operating with a gap comprised of only vacuum. However, an isolation layer between the TE and BE is crucial to ensure the electrodes do not electrically short during full gap swings in transmit and near collapse operation during receive. Instead, a similar increase in SNR can be supplied by increasing the relative permittivity of the dielectric material. This high relative permittivity dielectric material must also be able to withstand the electric fields generated within it during CMUT operation, especially at the above mentioned TE/BE interconnect overlap areas or if the CMUT has collapsed. Unfortunately, there exists a tradeoff between dielectric breakdown strength (E_{BD}) and the relative permittivity (ϵ_r). As a result, the figure of merit one should maximize in choosing the dielectric isolation material is actually the product: $E_{BD}\epsilon_r$.

In sacrificial layer technique fabrication of CMUT arrays, the isolation layer and membrane layer can be constructed with the same dielectric material, eliminating any adverse effects that might arise from material mismatch, such as adhesion issues and residual stress. The low stress PECVD silicon nitride utilized in f_{ares} limited array fabrication demonstrates a $E_{BD} = 6.5 \text{ MV/cm}$, and $\epsilon_r = 6.3$ [94]. Replacing the isolation layer with hafnium oxide deposited by atomic layer deposition (ALD), which demonstrates a $E_{BD} = 4 \text{ MV/cm}$, and $\epsilon_r = 15$ [76], one can improve the electrostatic force generated on the CMUT more than 2 times. Layers deposited with ALD are intrinsically stress-free. However, depending on the processing temperature of the ALD process, the thermal mismatch between the silicon substrate and the hafnium oxide layer can cause thermal

stress, which can affect the curvature of the CMUT membrane and even cause the device layer to peel-off, as seen in Figure 4.4.

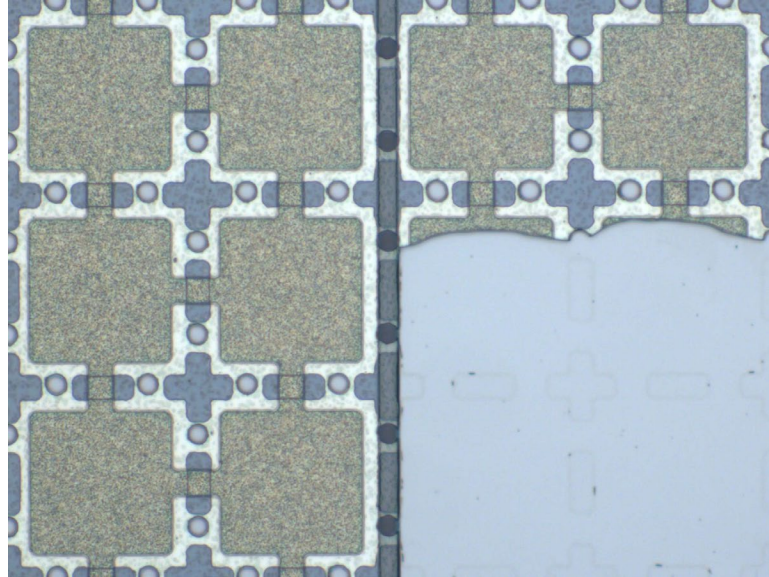


Figure 4.4: Catastrophic peel-off of CMUT membrane due to thermal stress in hafnium oxide isolation layer.

Details of the fabrication process utilized in fabrication of f_{Bragg} limited CMUT arrays is shown in Figure 4.5. Starting with a 4" $\langle 100 \rangle$ silicon wafer with 3 μm thermal oxide, chromium of 375 nm thickness is sputtered and patterned to form the BE of the CMUT arrays. Before establishing the sacrificial layer, half of the isolation layer is deposited on the BE to reduce the effect of thermal stress on the membrane. A hafnium oxide layer of 150 nm thickness is deposited with 1000 thermal ALD cycles at 250°C. To avoid over etching, a sacrificial layer of 80 nm of copper patterned on the wafer with lift-off. This is followed by the deposition the remaining hafnium oxide layer of 150 nm thickness via ALD. After the isolation has been established, 300 nm of aluminum silica (AlSi 1%) is sputtered and patterned to form the TE. 300 nm of low stress PECVD silicon nitride is deposited as initial membrane formation. As the next step, etch holes are patterned

and etched via RIE to reach the sacrificial layer. It should be noted that, a separate sulfur hexafluoride (SF_6) chemistry is needed to etch the hafnium oxide layer in addition to the standard fluoroform (CHF_3) chemistry used to etch silicon nitride. SF_6 is particularly aggressive to photoresist and one must be careful to use sufficiently thick photoresist. Sacrificial layer is etched via immersion in copper etchant APS 100 and the wafer is rinsed 4-5 times in water to remove any copper residues and dipped in isopropyl alcohol (IPA) overnight. As the gap thickness of the arrays are smaller than 100 nm, the sample is dried in CO_2 super critical dryer chamber, to avoid stiction. The remaining 700 nm of silicon nitride is deposited to seal the membranes and reach the desired membrane thickness. Finally, connection to the BE and TE is obtained by patterning the bond pads and etching the silicon nitride and hafnium oxide layer via RIE. Similar to f_{ares} limited array fabrication, temperatures of all processes do not exceed 250°C , indicating compatibility with CMOS wafers.

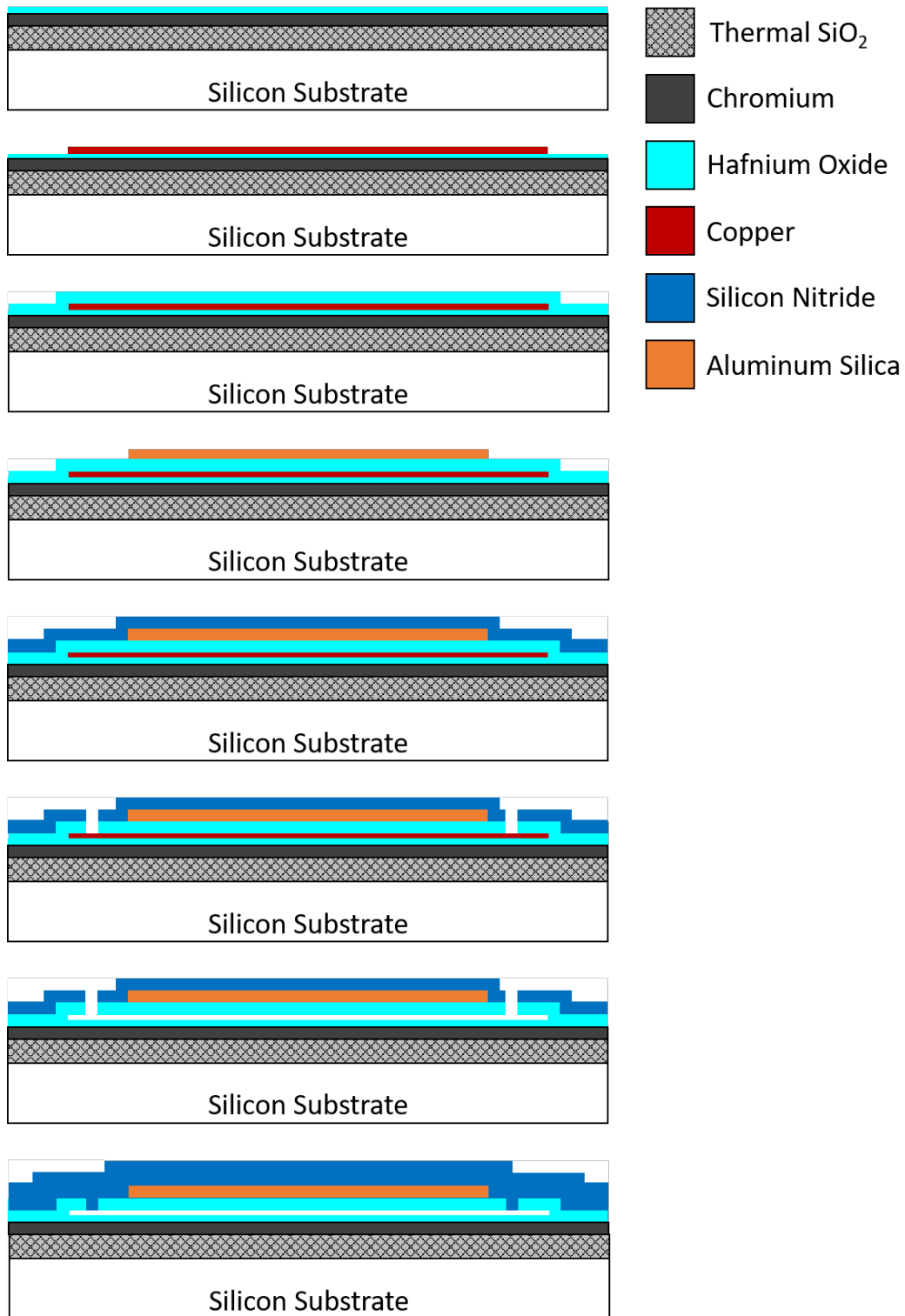


Figure 4.5: Schematic of fabrication process flow of f_{Bragg} limited CMUT arrays

4.3. Experimental Validation

Validation experiments consisted of pressure measurements and admittance measurements. Pressure measurements are effective in demonstrating the limiting mechanisms, but are limited by the frequency range of the hydrophone sensitivity and the transmitter pulse. Admittance/impedance measurements are susceptible to electrical parasitic elements but are not limited by any additional transmit-receive components, resulting in a more broadband analysis. Therefore, pressure measurements are used for f_{ares} limited arrays and admittance measurements are used for both f_{ares} and f_{Bragg} limited arrays. It should be noted that, even though both measurements are effective in demonstrating limiting mechanisms, they reveal different characteristics of the CMUT array. On axis pressure measurements consider a single point and involve diffraction, making them especially relevant for imaging performance. In comparison, admittance/impedance measurements provide information on both the radiated and non-radiated components allowing these measurements to show non-radiated features or features that can be lost due to wave propagation, such as the asymmetric vibration modes that are predicted by the model.

4.3.1. Pressure Measurements

Pressure output of the f_{ares} limited arrays are measured in a water tank at a normal angle and 10 mm distance, corresponding to the far field region of the CMUT arrays. Arrays are biased to 70 V and excited with a 50 ns long 70 V unipolar pulse, which is then used in the time domain model to obtain the simulated pressure output. The generated pressure is measured by a hydrophone calibrated between 1 to 20MHz. Figure 4.6 and

Figure 4.7 show the measured and simulated pressure outputs and their normalized frequency response. The measurements and simulations are in good agreement with each other in both time domain and frequency domain. The main discrepancy is identified as the ringing tail generated by silicon substrate ringing, which is not included in the simulation. The arrays demonstrate broadband acoustic behavior in agreement with an earlier study, with approximately 100% FBW and 5MHz f_{center} for 63 μm arrays and 90% FBW at 4MHz f_{center} for 78 μm arrays. The frequency response of the pressure signals clearly demonstrate the limiting effect of the crosstalk induced array modes, observed as a -6 dB dip in the vicinity of f_{single} , and a much stronger dip exceeding -30 dB in the vicinity of f_{ares} . The limiting effect of the silicon substrate ringing mechanism is also observed in the measurement as a dip around 7.7MHz.

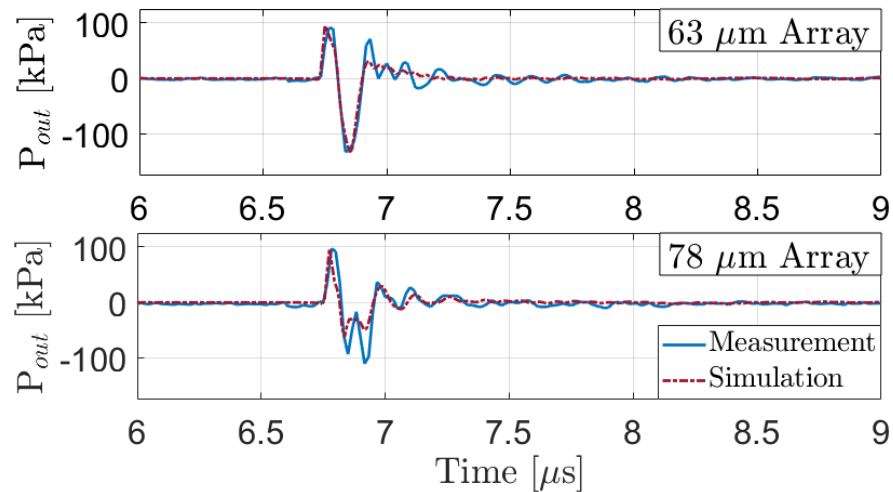


Figure 4.6: Comparison of simulated and measured pressure signals of f_{ares} limited arrays in time domain.

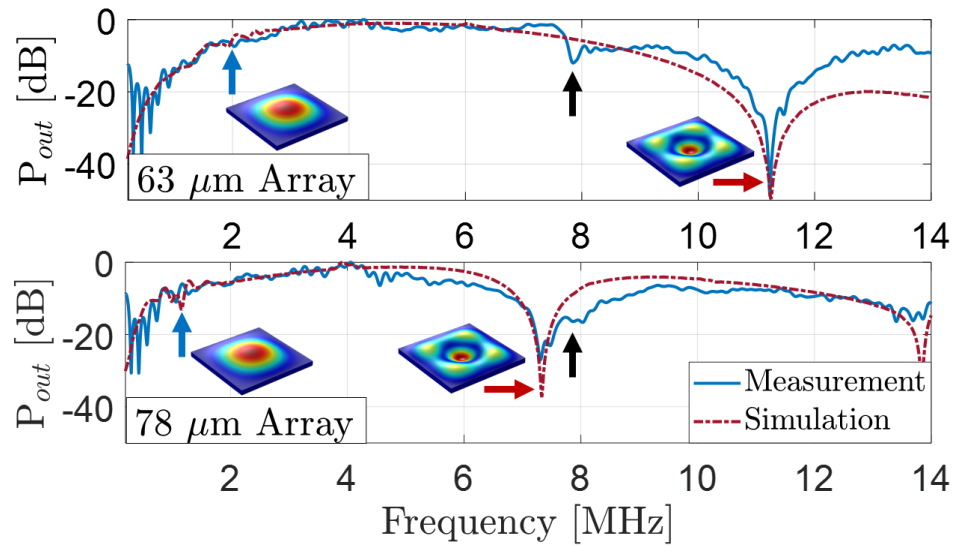


Figure 4.7: Comparison of simulated and measured pressure signals of f_{ares} limited arrays in frequency domain. The blue and red arrows denote the limiting frequencies of the crosstalk induced array modes and the black arrow denotes the dip in the frequency response due to wafer ringing

4.3.2. Admittance Measurements

Among the components that can be acquired from admittance/impedance measurements of CMUT arrays, conductance is especially suitable as the effect of parasitic capacitance is isolated in the susceptance. Figure 4.8 shows the comparison of the measured and simulated conductance of the 78 μm array immersed in water at three different bias voltages. The conductance values clearly demonstrate the effect of the limiting factors along with other vibroacoustic mechanisms across a broad frequency band, including array modes generated by the symmetric vibration modes (f_{single} , f_{ares} , and 3rd symmetric mode), the asymmetric vibration modes (1st and 2nd asymmetric mode), and Bragg scattering (f_{Bragg}). Of note are the asymmetric vibration modes, predicted accurately by the model and observed in the admittance data as a small peak around 4MHz.

These modes are only predicted by a full finite size array simulation and are not observed in far field pressure measurements, indicating the value of admittance measurements for model verification.

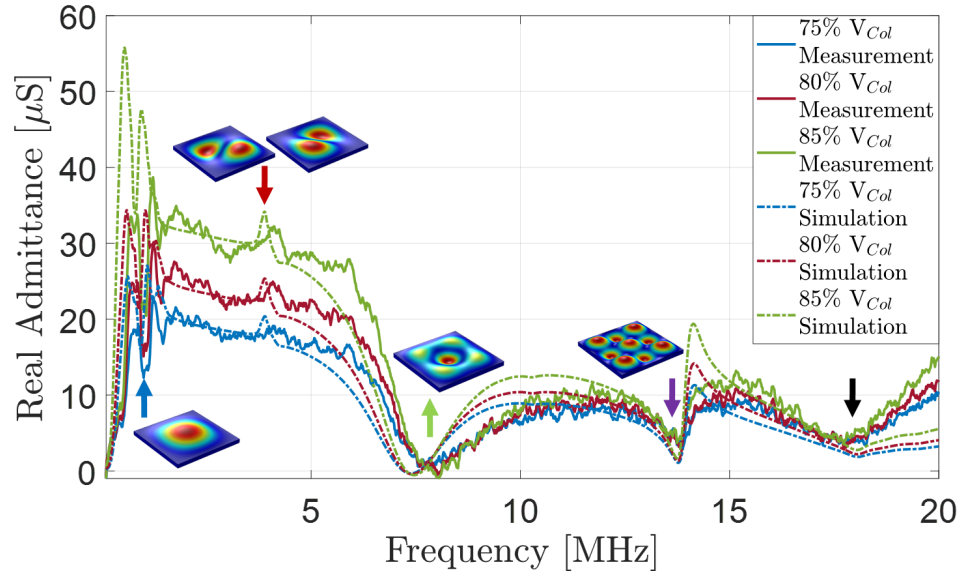


Figure 4.8: Comparison of simulated and measured conductance of 78 μm array. The colored arrows denote the limiting frequency of the crosstalk induced array modes and the black arrow denotes the limiting frequency due to Bragg scattering.

For high frequency arrays with Bragg scattering limited frequency response, admittance measurements are conducted since the pressure output measurements were out of the range of the available hydrophones. Figure 4.9 shows the real part of the admittance measured in water at 90% collapse voltage for arrays with same membrane geometry but different periodicity leading the different FF s of 36% and 49%, respectively. The simulations accurately predict the constant single membrane resonance and higher shifting f_{Bragg} with increasing FF . Similar to f_{ares} limited array measurements, the effect of silicon substrate ringing is observed in the measured conductance around the multiples of

7.7MHz, resulting in additional peaks and dips that are not observed in the simulated admittance.

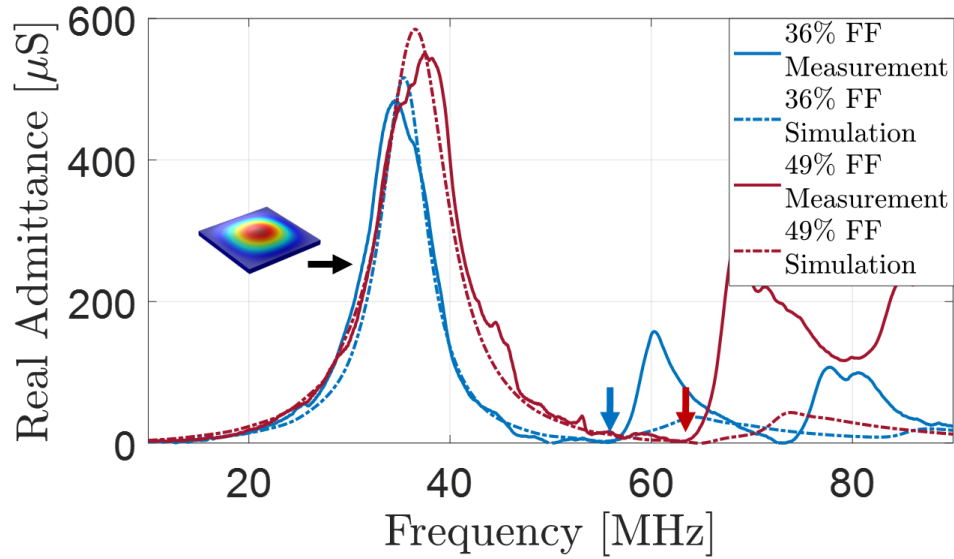
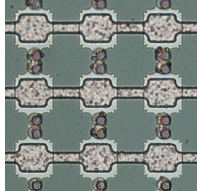
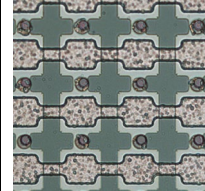


Figure 4.9: Comparison of simulated and measured conductance of f_{Bragg} limited arrays of 36% and 49% FF in water. The colored arrows denote the frequencies of Bragg scattering and the black arrow denotes the frequency of the crosstalk induced array modes in the vicinity of f_{single} .

4.3.3. Water vs FC-70

As it is directly proportional to the speed of sound in the immersion medium, Bragg scattering based limits can be further validated using an immersion fluid with a different speed of sound. A suitable fluid for such an analysis is FC-70 ($c_0 = 691$ m/s, $\rho = 1940$ kg/m³), which has nearly half the speed of sound in water while having similar acoustic impedance. Therefore, operation in FC-70 should result in an approximately 50% decrease in f_{Bragg} while maintaining similar f_{single} and f_{ares} values. Such a reduction in the upper frequency limit would result in a drastically more narrowband frequency response and a f_{center} shift to lower frequencies in f_{Bragg} limited array operation.

Table 4.3. f_{Bragg} limited limiting factor frequencies in FC-70

75x75 μm^2 section		
Fill factor [%]	36	49
f_{single} [MHz]	28.19	
f_{ares} [MHz]	146.1	
f_{Bragg} [MHz]	27.64	32.35

The limiting frequencies of the f_{Bragg} limited arrays immersed in FC-70 can be seen in Table 4.3. The effect of the lower f_{Bragg} values in FC-70 can be observed in Figure 4.10, in which Bragg resonance dips nearly at half the frequencies as compared to water is visible in both the admittance measurement results and the simulations. Note that when f_{single} and f_{Bragg} values are close to each other, the effect of Bragg scattering dominates the effect of crosstalk induced array modes, leading to a further shift to lower frequencies. Although the model predicts the main structures well into the higher frequencies, the impact of parasitic effects, especially inductance of the bondwires and PCB traces makes the fit to measurements less accurate. Nevertheless, these measurements in two different immersion fluids verify the main outputs of the model in terms of frequency limiting factors.

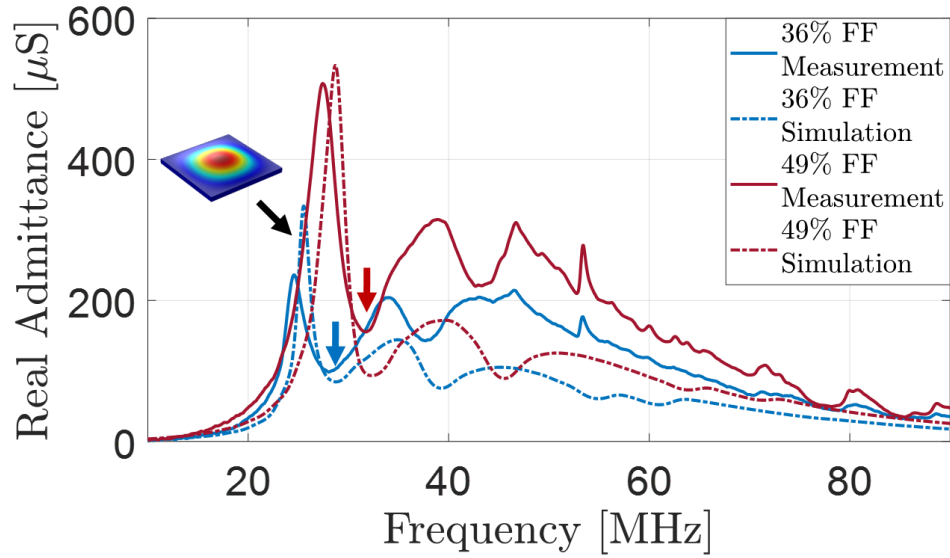


Figure 4.10: Comparison of simulated and measured conductance of f_{Bragg} limited arrays of 36% and 49% FF in FC-70. The colored arrows denote the frequencies of Bragg scattering and the black arrow denotes the frequency of the crosstalk induced array modes in the vicinity of f_{single} .

4.4. Integrated Guidewire IVUS Imaging System

A variation of the 20 μm square array geometry from the guidewire IVUS case study is fabricated with slight variation. While keeping the lateral dimensions and thickness the same, the total array size is increased to 300x1000 μm^2 , corresponding to 40 membranes for each element. Silicon nitride of 200 nm thickness is chosen as the isolation layer, and with a vacuum gap of 50 nm the collapse voltage is increased to 100 V. A micrograph of the fabricated CMUT array shown in Figure 4.11. The fabricated CMUT array is integrated to a CMOS system-on-a-chip (SoC) with channel reduction, transmit, and receive electronics, forming a full ultrasound imaging system suitable for integration on a 0.035" guidewire [96-98].

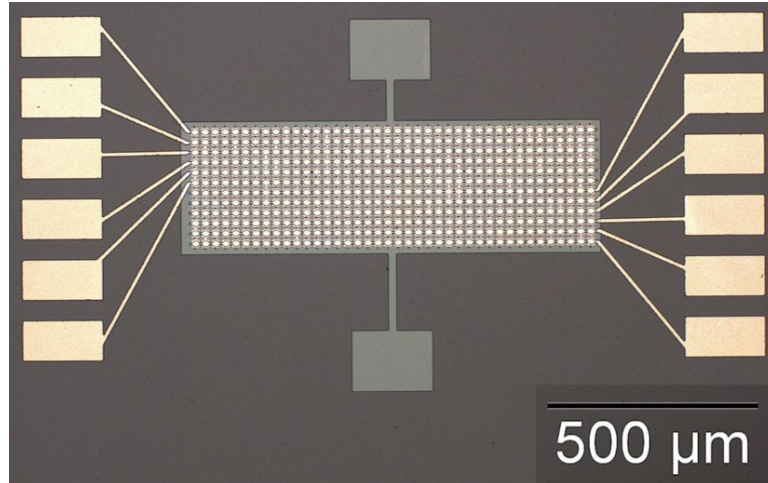


Figure 4.11: Micrograph of fabricated IVUS CMUT array [55].

4.4.1. Ultrasound Imaging System Characterization

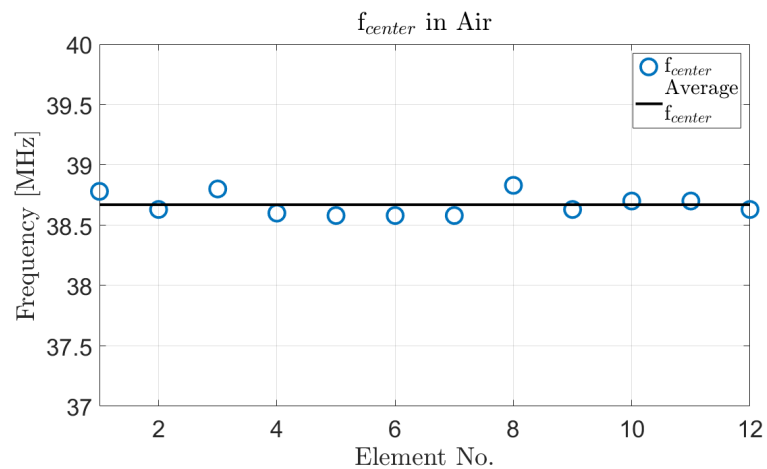


Figure 4.12: Measured f_{center} of each CMUT array element [55].

Electrical impedance measurement is performed for each of the 12 elements to determine device uniformity through resonance frequency in air. An average resonance frequency of 38.7MHz is observed at 80% collapse with a 90 kHz standard deviation between all elements, showing less than 1% f_{center} deviation among array elements, as seen in Figure 4.12.

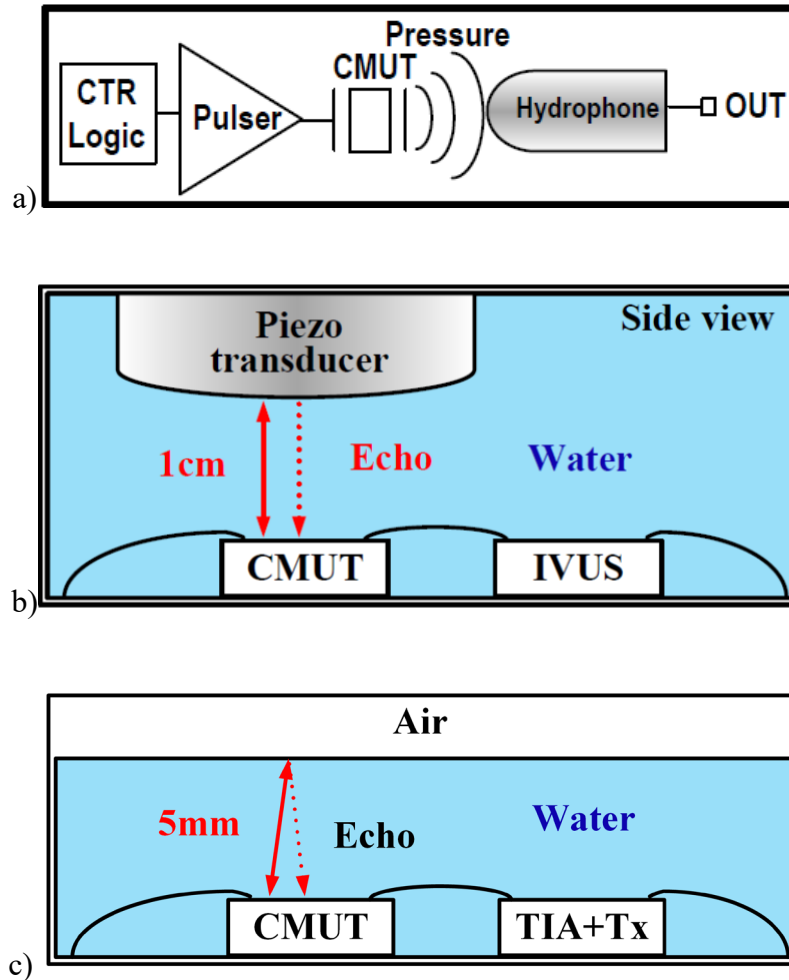


Figure 4.13: Measurement setup for a) transmitter, b) receiver, and c) pulse-echo characterization of SoC [97].

Ultrasound imaging system characterization is carried out on the CMUT elements biased to 80% collapse. Transmitter characterization of the ultrasound imaging system is carried out with an Onda HGL-0085 hydrophone calibrated between 0-60 MHz. CMUT elements are actuated with a 12.5 ns 40 V pulse and the generated pressure output is measured on axis at a 1 cm distance, as seen in Figure 4.13(a). A transmitter spectrum of 37.0 MHz f_{center} and 27% -3 dB FBW is measured. Receiver characterization of the ultrasound imaging system is carried out with an Olympus V358-SU piezoelectric transducer with 50 MHz f_{center} used to generate a pressure pulse, which is then received

by the CMUT elements, as seen in Figure 4.13(b). The spectrum of the piezoelectric transducer pressure output is measured with the Onda HGL-0085 hydrophone calibrated between 0-60 MHz, and subtracted from the measured signal spectrum to obtain the actual receiver frequency response. A receiver spectrum of 36.5 MHz f_{center} and 19% -3 dB FBW is measured. Full system characterization of the ultrasound imaging system is carried out through pulse-echo measurements with the water-air interface at 5 mm distance as the planar reflector, as seen in Figure 4.13(c). The CMUT elements are used as both transmitter and receiver to obtain the transient echo generated by the water-air interface, as seen in Figure 4.14. The pulse-echo signal spectrum is measured to have a 35.1 MHz f_{center} and 14% -3 dB FBW . The frequency response of all characterization can be seen in Figure 4.15. The SNR is obtained by dividing the peak voltage output of the pulse-echo signal to the root mean square (RMS) of output-referred noise of the ultrasound imaging system, resulting in an SNR of 36 dB.

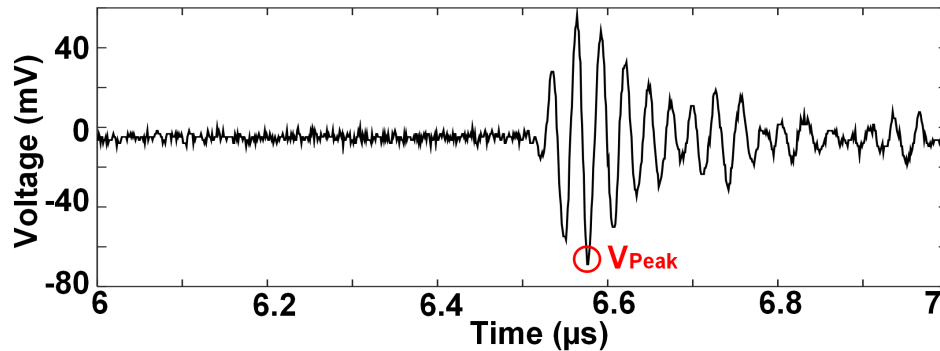


Figure 4.14: Transient pulse-echo signal of pulse-echo characterization [97].

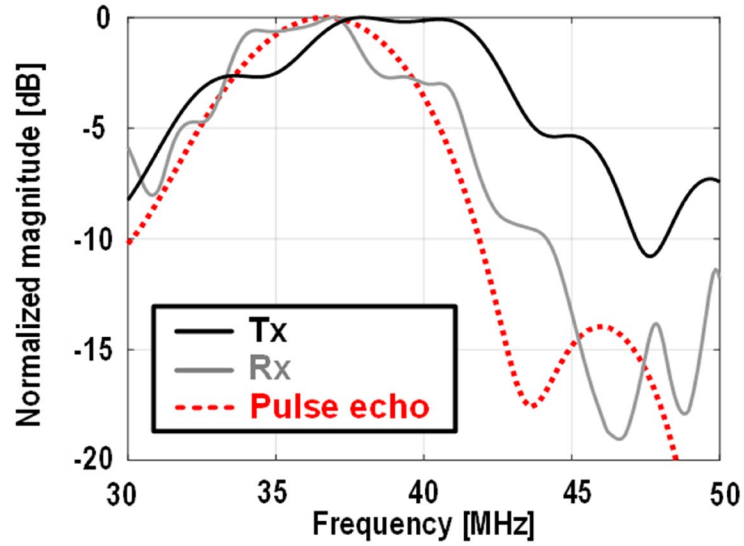


Figure 4.15: Transmitter, receiver and pulse-echo spectrums of the SoC [97].

4.4.2. System Imaging Measurement

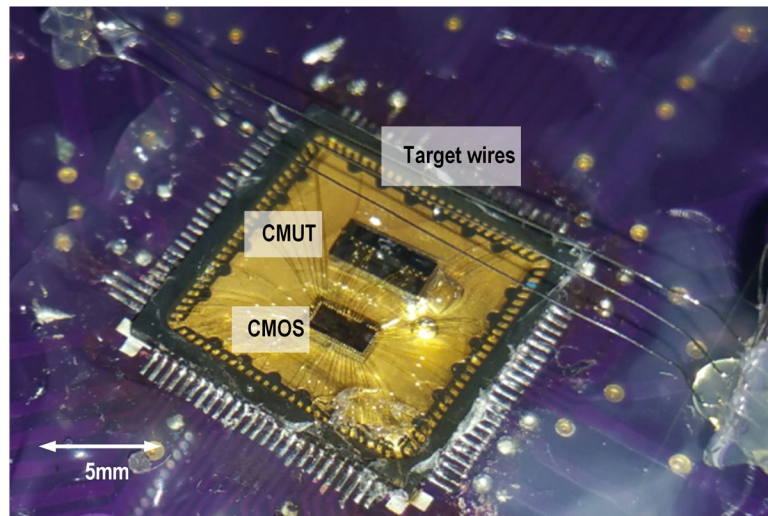


Figure 4.16: Imaging test setup of the ultrasonic imaging system [97].

The integrated ultrasound imaging system is utilized to obtain ultrasonic images of three $100\ \mu\text{m}$ diameter metal wires placed above the CMUT array, as seen in Figure 4.16. Image reconstruction is carried out with pulse-echo signals from all 12×12 transmit-receive

pairs to perform off-line processing and beamforming. Synthetic phased array technique is applied together with dynamic transmit and receive beamforming to calculate each pixel's intensity value. Standard delay-and-sum method, in which the ultrasound flight time is calculated from a particular transmit element to every pixel point in the image and back to receive element is utilized. The reconstructed image, as seen in Figure 4.17, shows the cross-sectional view of the wires, imaged in a gray scale dynamic range of 35 dB, where the brightest spot corresponds to peak signal level. This is close to the desired 40 dB dynamic range for clinical IVUS systems. The lateral resolution of the 3rd wire at 8 mm distance is 560 μm , in agreement with the expected resolution from a 300 μm aperture at 37 MHz. The image also shows two additional bright spots, which are artifacts due to reflection from the bondwire and packaging of the system.

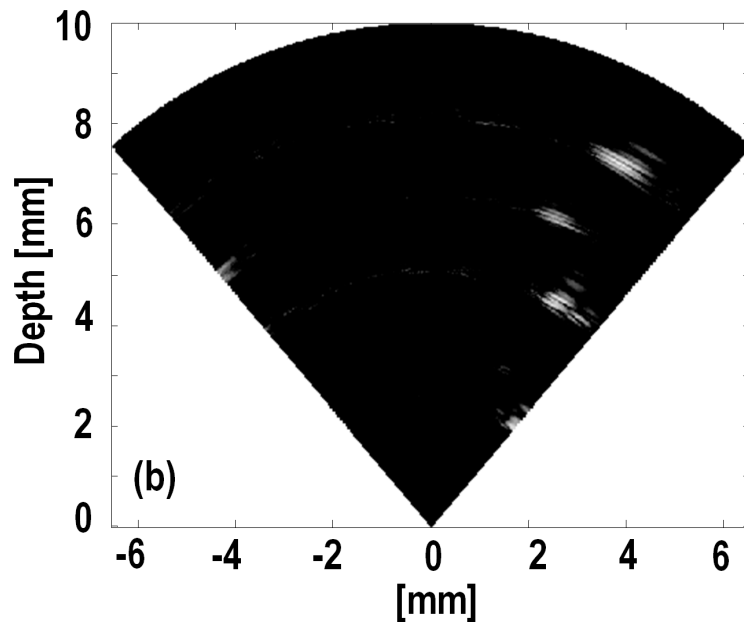


Figure 4.17: Constructed image of metal wires with 35 dB grey scale dynamic range [97].

CHAPTER 5. RECEIVER ELECTRONICS INTEGRATION ANALYSIS

It has been demonstrated in previous chapters that CMUT arrays can be designed to obtain broadband operation and high SNR. However, to fully take advantage of the CMUT arrays potential, one must consider the electrical termination integrated to the CMUT arrays. As previously discussed, electronic integration to CMUT arrays can be carried out with ease with multiple methods available, such as post-CMOS processing monolithic integration or flip-chip bonding. The analyses in the previous chapters considered low impedance termination, enabling thermal mechanical noise limited system assumption. However, the overall performance of the CMUT imaging system can be further improved by implementing impedance matching schemes between the CMUT element and the integrated electronics. This is especially significant, as typical terminations using trans-impedance amplifier (TIA) and low-noise amplifier (LNA) structures act as short-circuit and open-circuit termination respectively, resulting in limited power transfer and high acoustic reflectivity. Although there has been here a few studies on CMUT performance improvements in terms of power transfer and acoustic reflection in literature [99, 100], a more comprehensive analysis is needed to provide intuitive understanding of key parameters and their trade-offs, especially considering the possibility of using active circuits offered by integrated electronics.

In this chapter, different receive mode termination schemes are analyzed with respect to their capabilities in CMUT impedance matching. Afterwards, two different analysis methodologies to analyze power matching and acoustic matching performance is

introduced. Finally, the analysis methodologies are used to analyze the performance of a case study of 1D CMUT ICE array.

5.1. Receive Mode Termination Schemes

In receive mode operation, CMUT elements generate a change in current in response to a received acoustic signal, which is then converted to an output voltage via receive electronics. Therefore, front-end transceivers in CMUT imaging systems are generally chosen as TIAs, with structures based on LNAs also occasionally used. In comparison, TIAs present a low impedance and LNAs present a high impedance, which can be approximated as short-circuit and open-circuit termination respectively. However, as CMUTs demonstrate a complex impedance, neither termination is sufficient for CMUT impedance matching. Impedance matching of CMUT elements can be considered as two distinct functions, maximum power transfer from an acoustic signal to electrical domain and minimum acoustic reflection from an acoustic signal.

5.1.1. Power Matching

In electronics, for a complex source impedance Z_S , maximum power transfer is obtained when the load impedance Z_L is written as:

$$Z_L = Z_S^* \quad (5.1)$$

In which the asterisk indicates the complex conjugate of the variable. CMUT elements can be approximated as a Mason equivalent circuit in receive mode, allowing one to obtain the frequency dependent electrical impedance of a CMUT element Z_{CMUT} . Therefore,

maximum power transfer from a CMUT element with a receive circuitry of load impedance Z_{CMUT}^* . Assuming CMUT array aperture is significantly larger than the signal wavelength, the radiation impedance can be approximated as a resistor R . The source and load impedance at maximum power transfer then simply becomes:

$$Z_S = Z_{CMUT} = R || C \quad (5.2)$$

$$Z_L = Z_{CMUT}^* = R || -C \quad (5.3)$$

5.1.2. Acoustic Matching

During pulse-echo operation, the echoes generated in the medium are partially reflected by the transducer surface, resulting in propagation of a second unwanted set of ultrasonic waves. This effect, often referred to as multiple reflection reverberation, can cause noise and imaging artifacts, such as repetition of some of the imaged structures and appearance of bright bands in the axial direction if close parallel reflectors are present. Maximizing the power transfer from acoustic domain to electrical domain can be used to reduce the acoustic reflectivity of a CMUT element. Conversion and subsequent dissipation of the acoustic signal in electrical domain will naturally reduce the energy of the reflected acoustic signal. As a result, one might assume optimum conditions for power matching would coincide with optimum conditions for acoustic matching. However, acoustic impedance matching is achieved between medium and the CMUT surface, while power matching is achieved between the CMUT interface and front-end electronics. As a result, variation between the two optimum conditions is possible, especially if the CMUT radiation impedance is complex.

5.2. Impedance Matching Schemes

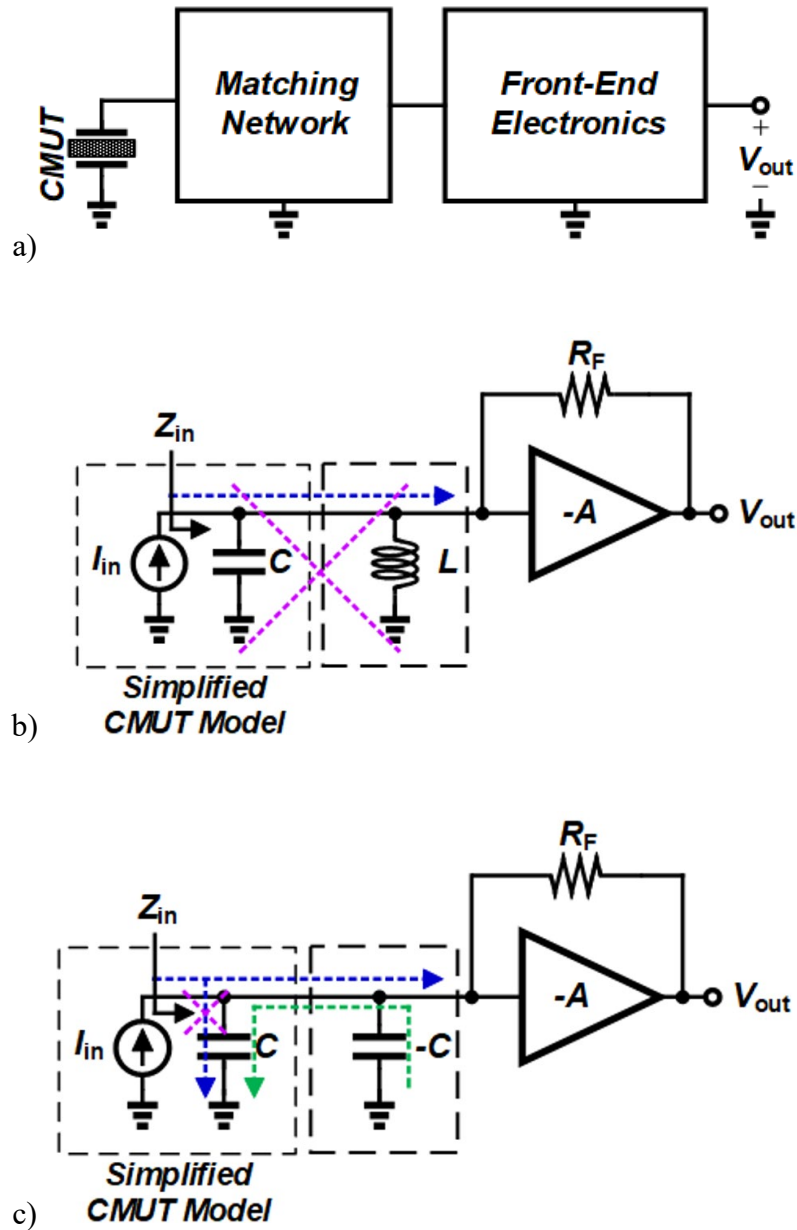


Figure 5.1: Conceptual view of a) impedance matching network at the interface of the CMUT and electronics, b) narrowband $R||L$ impedance matching, and c) broadband $R||-C$ impedance matching.

Impedance matching schemes can be determined by considering a matching network at the interface of the CMUT array and electronics, as seen in Figure 5.1 (a).

Considering Mason equivalent circuit of CMUT elements, the matching network needs to nullify the effect of the CMUT elements capacitance. Two impedance matching schemes can then be considered: inductor based impedance matching ($R||L$), and negative capacitance based impedance matching ($R||-C$). Through the use of a $Z_L = R||L$, as seen in Figure 5.1 (b), perfect power matching to a $Z_S = Z_{CMUT}$ can be obtained. However, due to the different trends followed by Z_{CMUT} and $R||L$, this matching would only occur in a very narrowband frequency range. A more broadband matching can be obtained using an active component of negative capacitance which would negate the CMUT element's capacitance, as seen in Figure 5.1 (c), to form $Z_L = R||-C$.

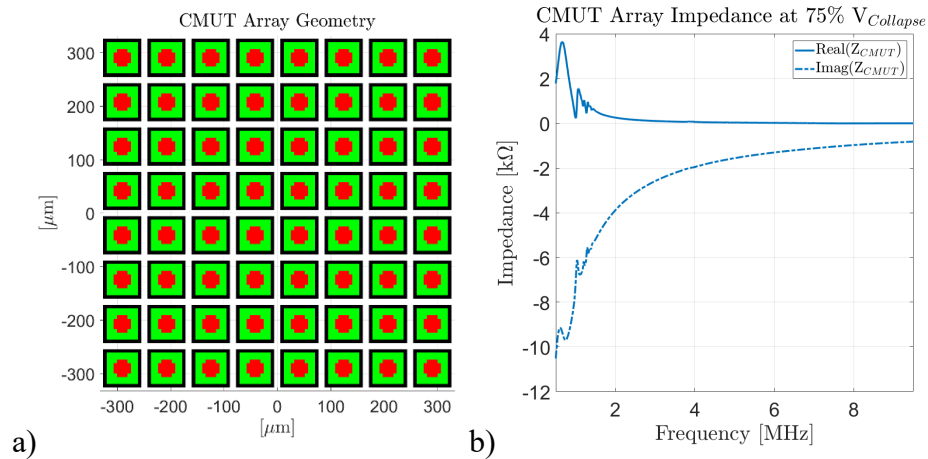


Figure 5.2: a) Analyzed CMUT array geometry. b) Analyzed CMUT array impedance.

To illustrate the difference between matching circuitry, a single element CMUT array of $665 \times 665 \mu\text{m}^2$ and $f_{center} = 5 \text{ MHz}$ is considered with $R||L$ and $R||-C$ matching receive circuitry. The CMUT array is biased to 75% collapse and its input impedance is calculated. The analyzed array geometry and the calculated impedance can be seen in Figure 5.2. Matching $R||L$ and $R||-C$ receive circuitry is obtained for 5 MHz operation.

A comparison of the impedance of the matching receive circuitry and the CMUT array impedance can be seen in Figure 5.3. The improvement in bandwidth for $R|| - C$ matching can be clearly seen when the real impedance of the CMUT array and receive circuitry is compared.

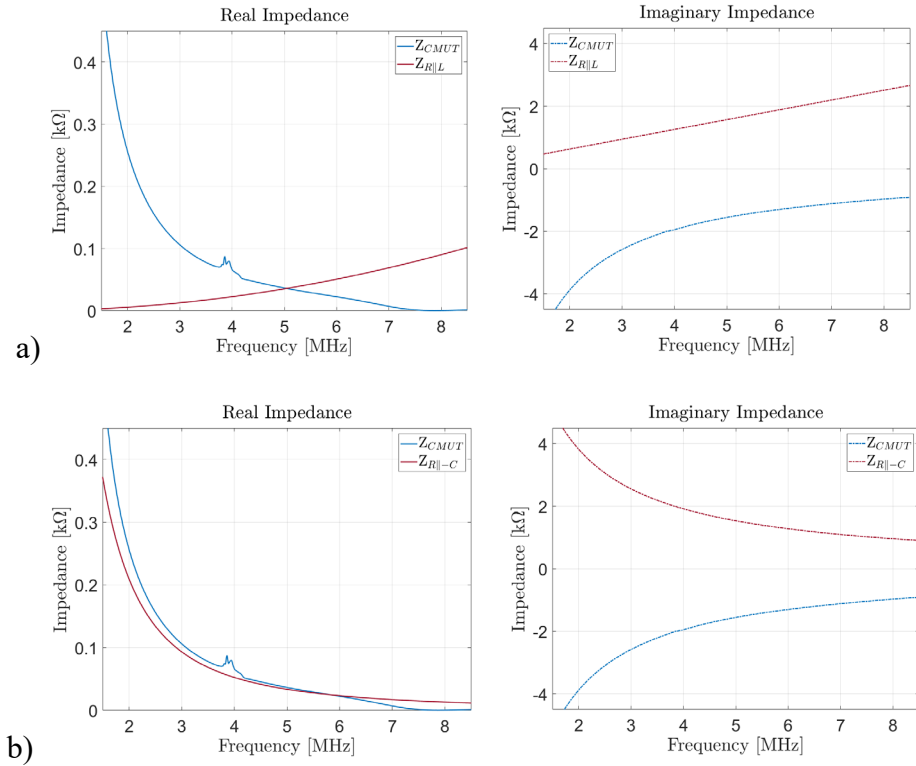


Figure 5.3: Comparison of CMUT array impedance with a) $R||L$ and b) $R|| - C$ matching receive circuitry.

The bandwidth of the two terminations can be analyzed through the power reflection coefficient [101] defined as:

$$|s^2| = \left| \frac{Z_S - Z_L^*}{Z_S + Z_L^*} \right|^2 \quad (5.4)$$

A comparison of the power reflection coefficient of different termination with a sample CMUT element can be seen in Figure 5.4. From the figure, it can be seen that inductor based impedance matching operates only around 5 MHz, whereas negative capacitance based impedance matching operates in the range of 1-5 MHz.

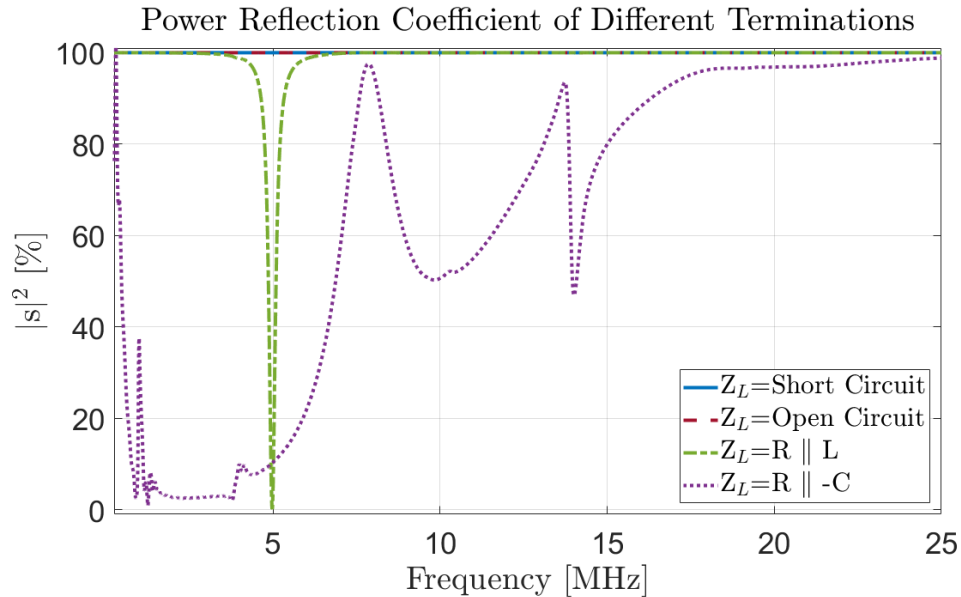


Figure 5.4: Power reflection coefficient comparison of different terminations.

5.3. Analysis Methodology

The effect of receive mode termination CMUT performance can be analyzed through pulse-echo mode modeling with integrated electronics. Using a fixed transmit configuration the echo generated from a perfect reflector can be received with varying receive termination. The transmitted pressure wave will propagate back and forth between the array and hard wall, as seen in Figure 5.5, generating multiple reflection output. As the transmit configuration is fixed, the 1st reflection is generated by the same pressure wave and variation is strictly due to the receive termination. Once the effect of the receiver

termination on the received signal strength is established, acoustic reflectivity of the CMUT element can then be analyzed by considering the amount of decrease observed in the following reflections.

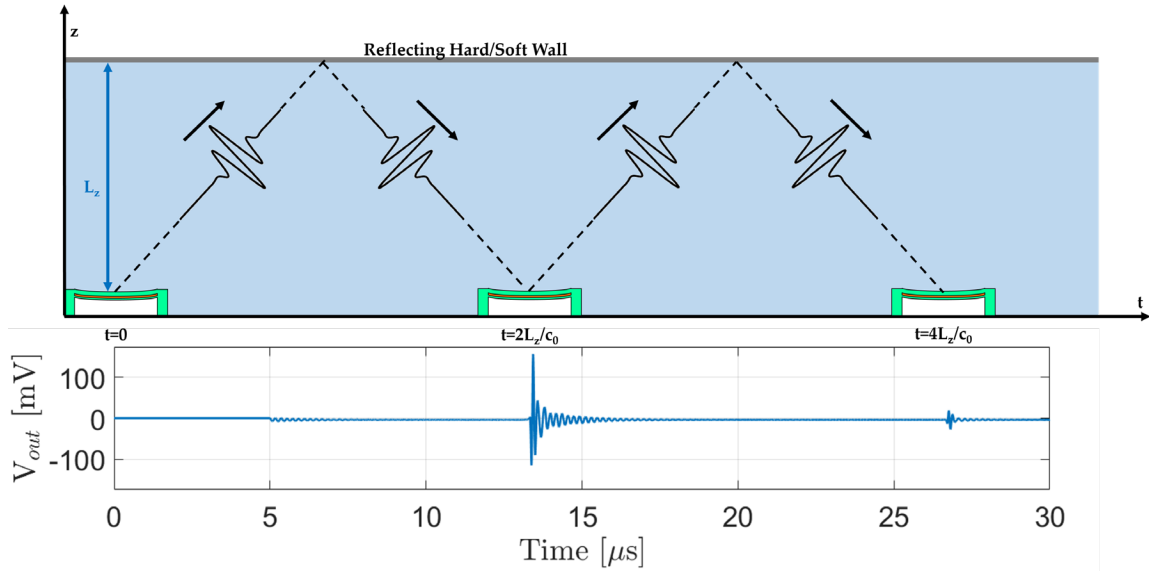


Figure 5.5: Time domain multiple reflection output utilized in acoustic reflectivity analysis.

5.4. Case Study: 1D ICE Array

A 1D CMUT array geometry developed for ICE imaging is chosen as a case study [49]. The investigated array geometry operates at a f_{center} of 9 MHz and with a FBW of 65% with 15-ns-width 30 V unipolar pulse with no DC bias [95]. Analysis is conducted on a 3-element configuration of the CMUT array, as shown in Figure 5.6 (a). Array elements are operated in transmit-receive mode and the pulse-echo response from a perfect reflector at 1 cm distance is examined. Each element is biased at 36 V, corresponding to 90% of the collapse voltage, and terminated with the short circuit transmitter and distinct receiver circuitry and zero parasitic capacitance. The center element is excited with a 50-ns-width

36 V unipolar pulse, and the multiple echoes and the corresponding signals generated by each element is simulated. The CMUT element impedance is calculated for receiver circuitry component selection. The calculated output impedance of the center element and the equivalent $R||C$ circuit is depicted in Figure 5.6 (b).

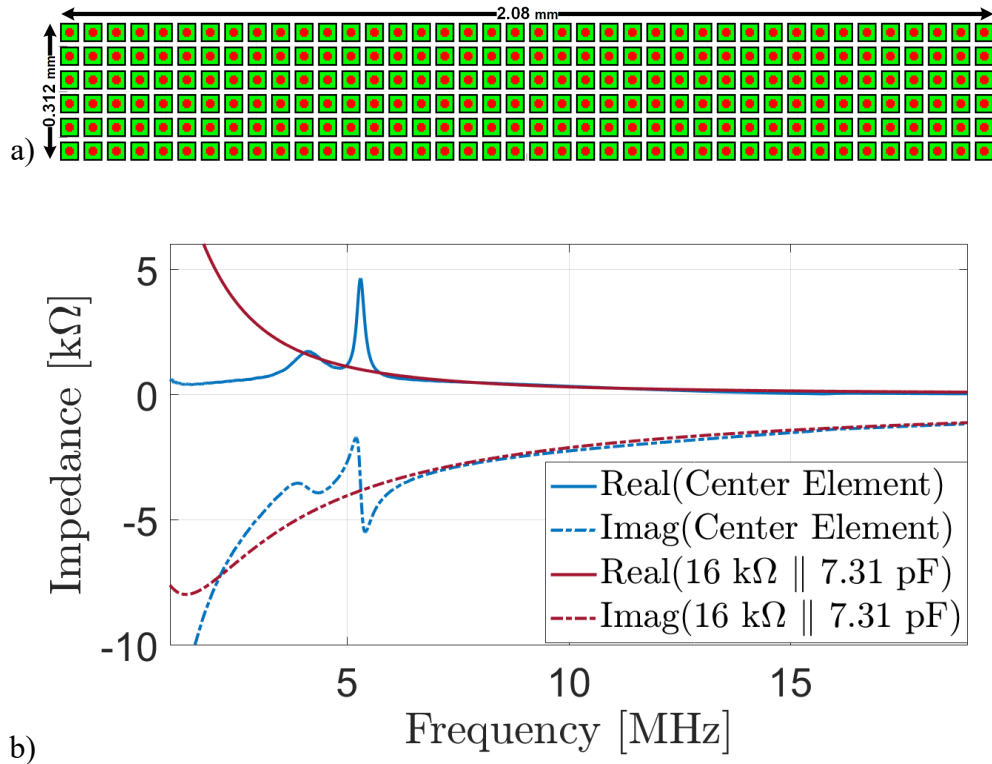


Figure 5.6: a) Analyzed 1D CMUT array geometry. b) Output impedance of the center element of the designed CMUT array biased at 36 V and the equivalent $R||C$ circuit.

The designed array was used to obtain the output response of the array for different terminations employing the pulse-echo model. Figure 5.7 shows the output response of the CMUT for different terminations. Short-circuit (SC), open-circuit (OC), narrowband impedance matching with inductor ($R||L$), and broadband impedance matching with negative capacitance ($R||-C$) are used for comparison between the CMUT's response at the presence of each termination. Figure 5.7 (a) shows the response of 0.1Ω termination,

which results in very weak echo, while Figure 5.7 (b) illustrates the response of $1\text{ G}\Omega$ termination. Figure 5.7 (c) shows the response of a $R||L$ ($16\text{ k}\Omega||45\mu\text{H}$), chosen as the complex conjugate at 9 MHz . Figure 5.7 (d) shows the response of a parallel $R||-C$ ($87\text{ k}\Omega||-7.31\text{ pF}$) termination. As expected, the broadband matching provided by the negative capacitance supplies higher output signal (1^{st} reflection), while the 2^{nd} reflection has been strongly attenuated due to reduced acoustic reflectivity made possible by the better acoustic matching in mechanical domain. It should also be noted that broadband matching termination affects the CMUT response variation between the CMUT elements.

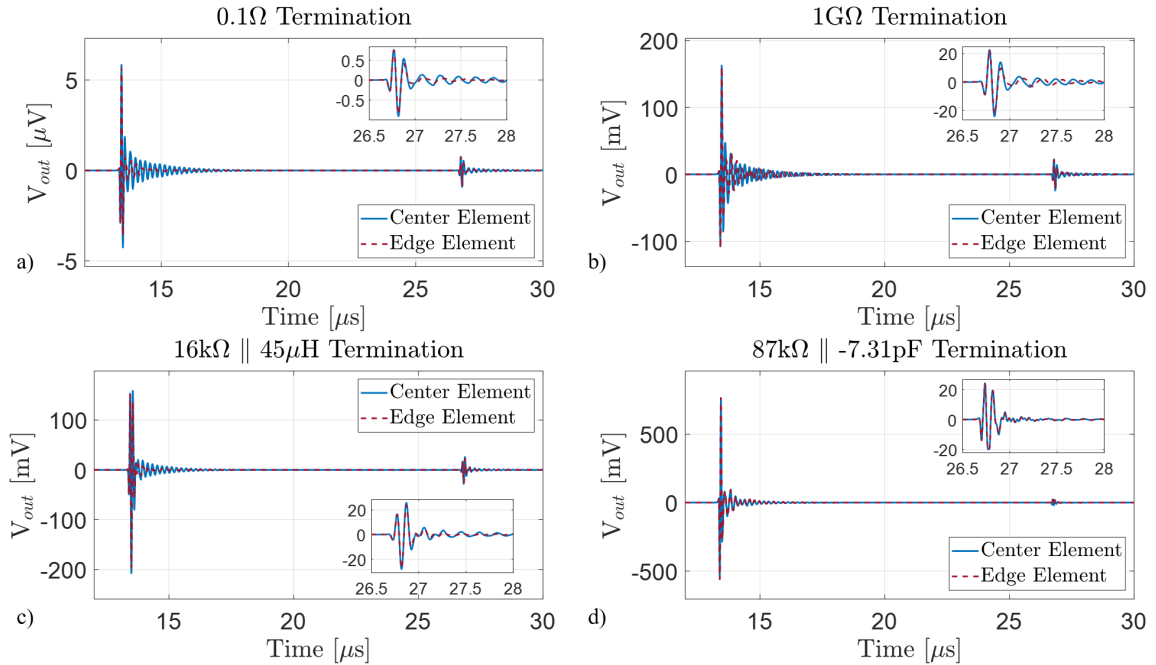


Figure 5.7: The simulated CMUT response at the presence of: (a) a SC with $0.1\ \Omega$ termination, (b) an OC with $1\text{ G}\Omega$ termination, (c) a narrowband matching circuit with $R||L$ ($16\text{ k}\Omega||45\mu\text{H}$) termination, and (d) a broadband matching circuit with $R||-C$ ($87\text{ k}\Omega||-7.31\text{ pF}$) termination.

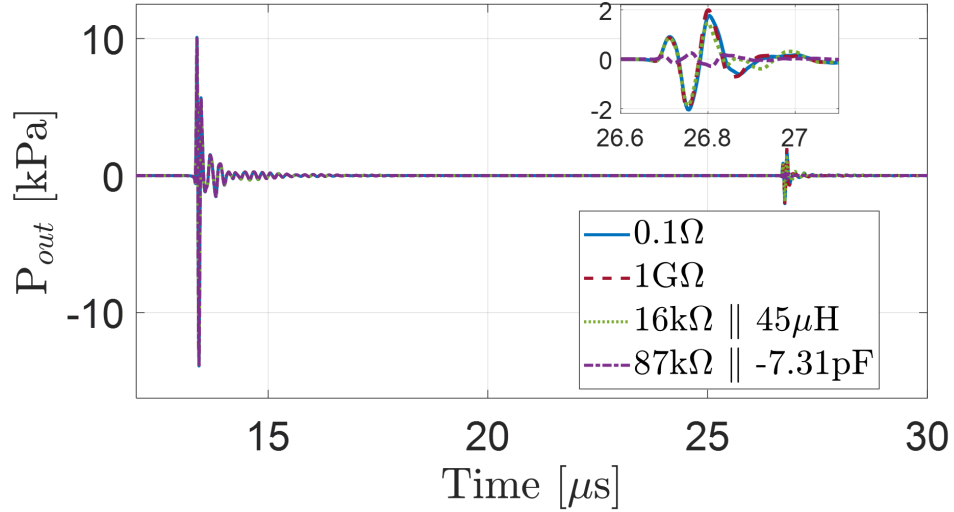


Figure 5.8: The simulated output acoustic pressure output of the CMUT for different terminations.

Figure 5.8 shows the output acoustic pressure of the CMUT at 2 cm distance for different terminations. The 1st output acoustic pressure is the initial transmitted pressure wave, while the 2nd pressure output is the reflected pressure wave from the CMUT array. From the figure, it can be seen that the amount of pressure radiating back toward the medium is reduced through improved acoustic matching, with maximum reduction observed in broadband impedance matching with negative capacitance. The normalized CMUT output voltage frequency response for different terminations can be seen in Figure 5.9. The $R||L$ impedance matching demonstrates the lowest FBW while the $R||-C$ impedance matching demonstrates the highest FBW over 100%, providing a broader operation frequency range.

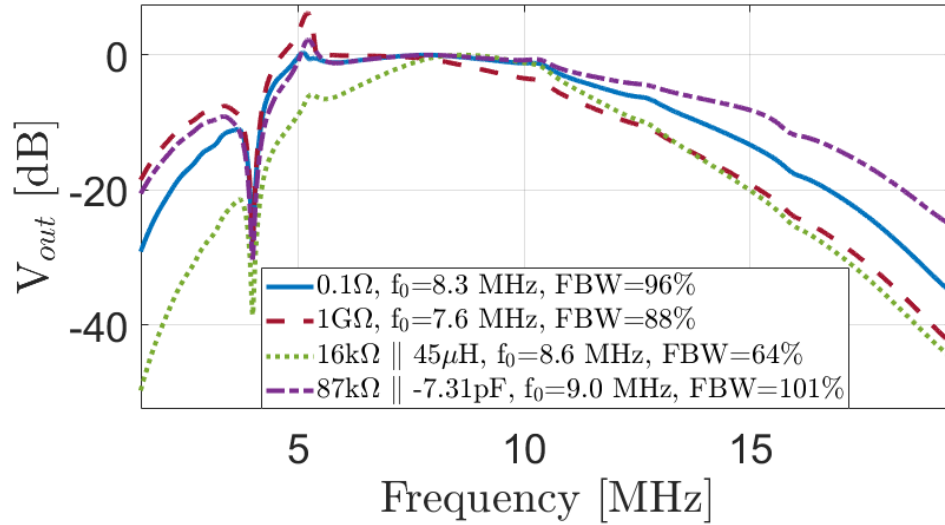


Figure 5.9: Frequency spectrum of the CMUT voltage output for different terminations.

5.4.1. Power Transfer and Reflectivity Analysis

The effect of termination on power transfer and acoustic reflectivity can be seen in Figure 5.10 and Figure 5.11 respectively. RMS power is calculated via multiplication of the voltage and current on the resistor of the receive termination, which is extracted and filtered in the range of interest (5-15 MHz). Reflectivity is calculated as the ratio of the 2nd echo power to the 1st echo power and normalized to the *SC* termination. Broadband impedance matching, through negation of the CMUT capacitance, provides better acoustic reflectivity and power transfer. However, the optimum resistive load for minimum acoustic reflectivity and maximum power transfer occur at different values. For the CMUT array geometry in our case study, minimum acoustic reflectivity is achieved at 87 k Ω , while maximum power transfer is achieved at 16 k Ω .

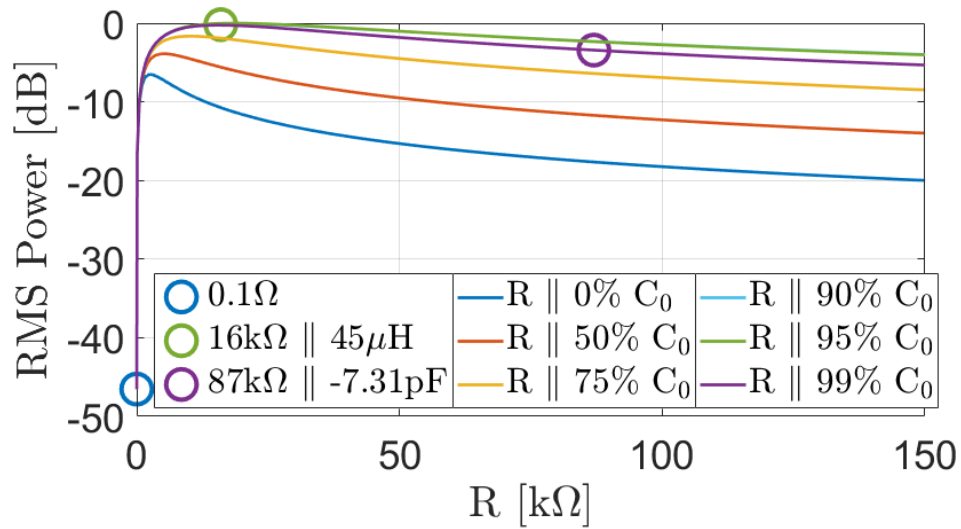


Figure 5.10: Normalized RMS power for different terminations vs. resistive load.

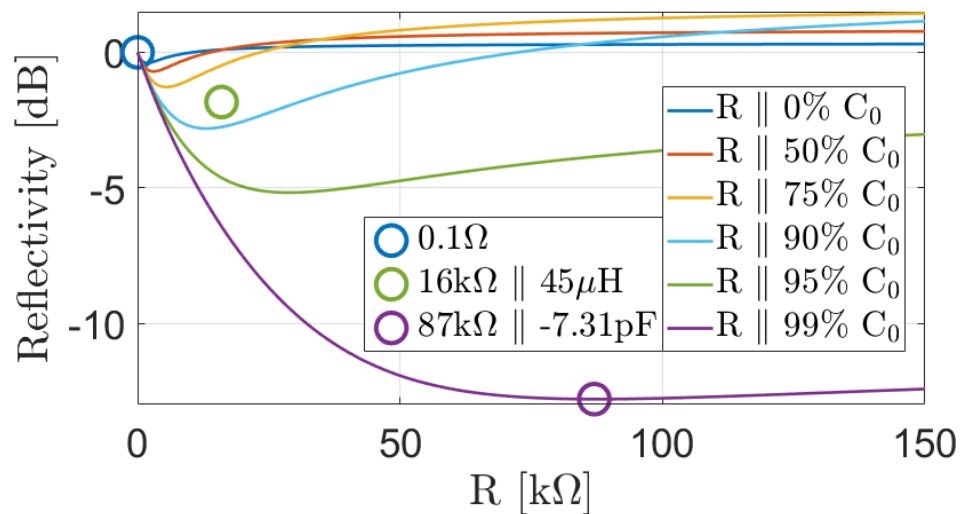


Figure 5.11: Acoustic reflectivity for different terminations vs. resistive load.

To evaluate the overall SNR, the total noise is obtained by integrating the power spectral density (PSD) of the total noise over the bandwidth of interest (5-15 MHz). The total PSD of the imaging system is the superposition of noise PSDs for two uncorrelated noise sources, the thermal-mechanical current noise of the CMUT and the input-referred noise of the front-end electronics. Figure 5.12 illustrates the overall SNR for different

values of ideal negative capacitance and optimum resistive load for minimum acoustic reflection. The overall SNR shows an improvement of 9 dB when the negative capacitor is chosen to be 99% of the CMUT static capacitance. It should be noted that an ideal negative capacitance circuitry with no noise is assumed and the CMUT current noise and resistive noise of receive circuitry is considered as the dominant noise source of the system.

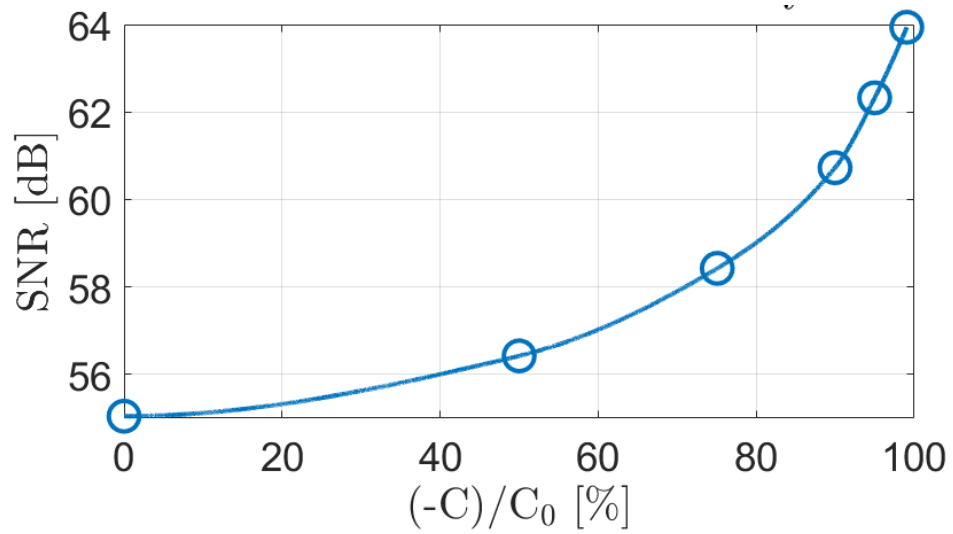


Figure 5.12: The overall SNR for different negative capacitances.

CHAPTER 6. CONCLUSIONS AND FUTURE WORK

6.1. Conclusions

High frequency ultrasound imaging arrays are important for a broad range of applications, from small animal imaging to photoacoustics. CMUT arrays are particularly attractive for these applications due to the large design space enabled by the flexibility of available fabrication processes and ease of integration with low noise receiver electronics that enables an overall improved performance. The objective of this research is to determine and verify performance limitations of high frequency CMUT arrays and develop a design methodology for specific operation requirements as well as to design, fabricate and characterize high frequency 1D CMUT array for IVUS imaging.

6.2. Contributions

6.2.1. Frequency Band Limitations and Design Methodology

We established analysis methodologies based on specific figure of merits that enable compact analysis of CMUT array's receiver, transmitter, and overall performance. We elected pressure noise spectrum as the ultimate receiver figure of merit, and pulse-echo SNR as the ultimate overall system parameter. We utilized these analysis methodologies to determine the effect of multiple design parameters on the frequency response and array performance for a case study of guidewire IVUS imaging arrays. Two vibroacoustic mechanisms were identified as frequency limiting mechanisms: Bragg scattering and crosstalk induced array modes. Based on these vibroacoustic mechanisms and the figure of merits, we established a design methodology for high frequency CMUT arrays. We

expanded the design methodology to encompass a broader frequency range and other applications.

6.2.2. Experimental Validation and Imaging System Construction

We utilized the developed design methodologies to design and fabricate two set of CMUT arrays operating in very different frequency operation ranges. Considering fabrication limitations for the different CMUT array geometries, we modified the fabrication process with respect to reliability or SNR. Using hydrophone and admittance measurement in comparison with simulations, we experimentally verified the frequency limiting mechanisms and the design methodology. We fabricated one of the analyzed guidewire IVUS array geometries and integrated it with a CMOS system-on-a-chip with transmitter and receiver electronics along with channel reduction capability. We analyzed the imaging system performance through pressure output, pitch-catch, and pulse-echo measurements. The imaging system demonstrated sufficient SNR with slightly narrower operation bandwidth.

6.2.3. Receiver Electronics Analysis

Finally, we analyzed the effect of receive electronics, focusing on impedance matching. Two impedance matching cases, narrowband inductor based and broadband negative capacitance based matching, was compared in a case study of 1D ICE imaging array. We established that negative capacitance based matching can drastically increase the power transferred from the acoustic medium to the electrical domain and significantly reduce the reflected portion of an input acoustic signal, without reducing the frequency operation bandwidth.

6.3. Future Work

The research presented in this dissertation focused on non-collapse mode operation. However, the established vibroacoustic limiting mechanisms fundamental for all flexensional transducers. Therefore, the design methodology can be extended to piezoelectric micromachined ultrasonic transducers (PMUTs) and collapsed mode operation CMUTs. The relation between frequency band and SNR of such arrays can be analyzed to establish a similar operation design guideline.

The preliminary analysis of the effect of membrane shape and array geometry on frequency band demonstrated higher operation bandwidth for circular membrane populated in a hexagonal array lattice. This increase in bandwidth makes them especially attractive for high frequency CMUT array design. However, the intrinsically lower fill factor of circular membrane arrays is expected to affect the overall SNR of the imaging system. Further analysis can be conducted to establish a similar design methodology for circular membrane arrays.

The research presented in this dissertation consider each element to operate in transmit-receiver mode, in which all elements are biased close to collapse while in transmit and receive mode. However, separating transmitter and receiver elements enable operation in different biases, which can further increase SNR. The effect of the resulting variation in single membrane dynamics across the CMUT array can be analyzed and if needed different design guidelines can be established.

A simplified assumption of CMUT impedance as a resistor and capacitor have been utilized in determining the optimum receiver electronics for impedance matching.

Coupling of the lumped nonlinear model into an electronics simulator, such as SPICE, can enable analysis of realistic complete imaging systems. As a result, realistic SNR and operation bandwidth operation can be calculated.

APPENDIX A. SAMPLE MATLAB CODES FOR RECEIVER ANALYSIS

A.1. Impedance and Thermal Mechanical Current Noise Calculation

Using transient simulation data of Gaussian input voltage pulse and output current.

```
%% Electrical Impedance and Noise Analysis

% Find peak voltage pulse and time step
% To adjust FFT time frame

del_t=(t(2)-t(1)); % Time step
V_pulse_ind=find(myvin==max(myvin),1); % Voltage pulse indice

time_window=2.5e-6; % FFT time window

ind_start=V_pulse_ind-round(50e-9/del_t);
ind_end=ind_start+round(time_window/del_t);

% Convert voltage and current to frequency domain
% Calculate the FFT of the input voltage

fs= 1/(t(2)-t(1));
y = myvin(ind_start:ind_end);
% plot(y)
mymean=myVdc(end);
y=y-mymean;
N = 16*2^nextpow2(length(y));
X = ((fft(y,N))/(length(y)));
X=2*X;
V_comp = X; % Complex voltage

% Calculate the FFT of the output current

y = Iall(ind_start:ind_end);
% plot(y)
mymean=mean(y);
y=y-mymean;
N = 16*2^nextpow2(length(y));
X = ((fft(y,N))/(length(y)));
X=2*X;
I_comp = X; % Complex current

F = linspace(0,fs,N); % Frequency

% Calculate Z_cmut
```

```

Z_cmut_comp = V_comp./I_comp;
Z_cmut_comp(1)= Z_cmut_comp(2); % CMUT element impedance

% Calculate the base impedance

Z_temp = 1./(1i*2*pi*F*Ct(length(Ct))); % CMUT capacitance impedance

% Adjust the frequency range

F_start=5e6;
F_end=200e6; % Frequency range of interest

ind1 = find(F > F_start, 1);
ind2 = find(F > F_end, 1);

Z_cmut_comp = Z_cmut_comp(ind1:ind2);

% Calculate the admittance

Y_cmut_comp = 1./Z_cmut_comp;

% Calculate thermo-mechanical noise

k_boltz = 1.3806488e-23; % Boltzmann's constant
T = 37+273.15; %[Kelvin] RT = ~25C, body temperature = 37C
I_cmut_TM_noise = 4*k_boltz*T.*real(Y_cmut_comp);
% Thermal mechanical current noise spectrum

F1 = linspace(F_start,F_end,length(I_cmut_TM_noise));

% Integrated thermal mechanical current noise

% I_cmut_noise_sq = sum(abs(I_cmut_TM_noise))*(F1(2)-F1(1));
%Rectangular estimation

I_cmut_noise_sq = trapz(F1,real(I_cmut_TM_noise));
%Trapezoidal estimation

```

A.2. Plane Wave Pressure Sensitivity and Transformer Ratio Calculation

Using transient simulation data of Gaussian input force pulse, output current, and membrane displacements.

```

%% Force to Current Analysis

del_t=(t(2)-t(1)); % Time step

app_p=App_p; % Transient applied pressure

```

```

% Calculate average velocity

patchno=2; % Number of patches
%First two are generally the electrode area

disp_ave=zeros(length(t),1);

%For calculating the average displacement of electrode area

for indec=transmitters
    for indec2=1:2
        disp_ave=disp_ave+disp(:,(indec-1)*patchno+indec2)...
            *Areas(patchno*(indec-1)+indec2);
    end
end

Area_cmut_act=0; % Active CMUT area

for indec=transmitters
    for indec2=1:2
        Area_cmut_act=Area_cmut_act+Areas(patchno*(indec-1)+indec2);
    end
end

disp_ave=disp_ave/(Area_cmut_act); % Average CMUT element displacement

if xy_sym==1
    Area_cmut_act=2*Area_cmut_act;
elseif xy_sym==2
    Area_cmut_act=4*Area_cmut_act;
end

% figure; plot(t,disp,t,disp_ave,'o')

u_ave=gradient(disp_ave,t(2)-t(1)); % Average CMUT element velocity

% Find the indices for force pulse

F_pulse_ind=find(app_p==max(app_p),1);

ind_start=F_pulse_ind-round(50e-9/del_t);
ind_end=ind_start+round(time_window/del_t);

% Check velocity with current
% figure;
% figure;
% plot(t(ind_start:ind_end),Iall(ind_start:ind_end)...
%     /max(abs(Iall(ind_start:ind_end))))
% hold on
% plot(t(ind_start:ind_end),-u_ave(ind_start:ind_end)...
%     /max(abs(u_ave(ind_start:ind_end))), 'o')

% Calculate total force

```

```

Force_tot=zeros(length(t),1);

for indec=transmitters
    for indec2=1:patchno
        Force_tot=Force_tot+app_p*Areas((indec-1)*patchno+indec2);
    end
end

if xy_sym==1
    Force_tot=2*Force_tot;
elseif xy_sym==2
    Force_tot=4*Force_tot;
end

% Convert velocity and current to frequency domain
% Calculate the FFT of the velocity
fs= 1/(t(2)-t(1));

y = u_ave(ind_start:ind_end);
% plot(y)
mymean=mean(y);
y=y-mymean;
N = 16*2^nextpow2(length(y));
X = ((fft(y,N))/(length(y)));
X=2*X;
u_comp = X; % Complex velocity

% Calculate the FFT of the current
y = Iall(ind_start:ind_end);
% plot(y)
mymean=mean(y);
y=y-mymean;
N = 16*2^nextpow2(length(y));
X = ((fft(y,N))/(length(y)));
X=2*X;
I_comp = X; % Complex current

% Calculate the FFT of the force
y = Force_tot(ind_start:ind_end);
% plot(y)
mymean=mean(Force_tot(ind_start-500:ind_start));
y=y-mymean;
N = 16*2^nextpow2(length(y));
X = ((fft(y,N))/(length(y)));
X=2*X;
Force_comp = X;
F = linspace(0,fs,N);

% Calculate I/u (transformer ratio)

phi = -I_comp./u_comp;
phi(1)= phi(2); % Complex transformer ratio

F_start=5e6;
F_end=150e6; % Frequency range of interest

```

```

ind1 = find(F > F_start, 1);
ind2 = find(F > F_end, 1);
phi = phi(ind1:ind2); %10-100MHZ
F1 = linspace(F_start,F_end,length(phi));

phi_val=real(mean(phi)); % Transformer ratio

Vdc=myVdc(length(myVdc));
isol_eps_r=15;
g_eq0=membranes{1,1}.gaps(1)+membranes{1,1}.isolation(1)/isol_eps_r;
% The equivalent gap

phi_temp=Vdc*Ct(length(Ct))/(g_eq0+disp_ave(length(disp_ave)));
% Theoretical transformer ratio

%%Calculating the I2F from the simulation

I2F=Force_comp./I_comp;
I2F(1)=I2F(2); % Complex force to current

I2F = I2F(ind1:ind2);

%%Calculating the P2I

Area_cmut=0;

for indec=transmitters
    for indec2=1:patchno
        Area_cmut=Area_cmut+Areas((indec-1)*patchno+indec2);
    end
end

if xy_sym == 1
    Area_cmut=Area_cmut*2;
elseif xy_sym == 2
    Area_cmut=Area_cmut*4;
end

P2I=abs(1./I2F)*2*Area_cmut; % Complex pressure to current

```

A.3. Pressure Noise Spectrum Calculation

Using calculated current noise and plane wave pressure sensitivity.

```

% Calculate minimum pressure from I_cmut_TM_noise

I_cmut_noise= I_cmut_TM_noise;
I2F_noise=I2F;
F_noise=F1;

```

```
Force_noise=abs(I2F_noise).*abs(I2F_noise).*I_cmut_noise;
Force_noise=sqrt(Force_noise);
pin_noise=Force_noise/Area_cmut_act; % Pressure noise spectrum
```

A.4. Ideal Piston Radiation Impedance Calculation

For a rectangular baffled piston.

```
% Using the formula from "J. Lee and I. Seo, Journal of Sound and
Vibration, vol. 198, no. 3, pp. 299-312, 1996/12/05/ 1996."
```

```
function [ result ] = xIntFun( xRange, L, W, k)
    xLen = length(xRange);
    result = zeros(1,xLen);
    for i = 1 : xLen
        x = xRange(i);
        result(i) = integral(@(y)yIntFun(y, x, L, W, k),0,L);
    end
end
function [ result ] = yIntFun( yRange, x, L, W, k)
    yLen = length(yRange);
    result = zeros(1,yLen);
    for i = 1 : yLen
        y = yRange(i);
        firstFun = @(theta,x,y,L,W,k) ...
            (exp((-1i*k*(W-x)).*sec(theta))-1);
        secondFun = @(theta,x,y,L,W,k) ...
            (exp((-1i*k*(L-y)).*sec(theta))-1);
        thirdFun = @(theta,x,y,L,W,k) ...
            (exp((-1i*k*(L-y)).*sec(theta))-1);
        fourthFun = @(theta,x,y,L,W,k) ...
            (exp((-1i*k*( x)).*sec(theta))-1);

        firstInt = integral(@(theta)firstFun...
            (theta,x,y,L,W,k),0,atan((L-y)/(W-x)));
        secondInt = integral(@(theta)secondFun...
            (theta,x,y,L,W,k),0,atan((W-x)/(L-y)));
        thirdInt = integral(@(theta)thirdFun...
            (theta,x,y,L,W,k),0,atan(( x)/(L-y)));
        fourthInt = integral(@(theta)fourthFun...
            (theta,x,y,L,W,k),0,atan((L-y)/( x)));

        result(i) = firstInt + secondInt...
            + thirdInt + fourthInt;
    end
end
```

```
% Comparison to Ideal Piston
% fluid_rho = 1940; %[kg/m^3] FC-70
% fluid_c = 691; %[m/s]
```

```
fluid_rho = 1000; %[kg/m^3] water
fluid_c = 1500; %[m/s]
```

```

%%Ideal Piston Impedance calculation

f=10e3:10e3:50e6; % Frequency range

omega=f*2*pi;
kRange=omega/fluid_c;
j=sqrt(-1);

L=2750e-6; % Piston length
W=750e-6; % Piston width

Z_rad = zeros(1,length(kRange));
parfor i = 1 : length(kRange)
    % tic;
    k= kRange(i);
    Z_rad(i)=(-fluid_rho*fluid_c/pi())...
        *integral(@(x)xIntFun(x, L, W, k),0,W);
    % fprintf('%d took %d seconds\n',i,toc);
end

% figure;plot(f,real(Z_rad),f,imag(Z_rad))

save(['Piston Radiation Impedance for '...
    num2str(L/1e-6) ' x ' num2str(W/1e-6) ' um Piston'],'-v7.3')

```

A.5. Ideal Piston Pressure Noise Spectrum Calculation

Using the radiation impedance of an ideal piston.

```

Area_pist=L*W; % Piston area
f_pist=f; % Frequency range

k_boltz = 1.3806488e-23; % Boltzmann's constant
T = 37+273.15; %[Kelvin] RT = ~25C, body temperature = 37C
F_piston_squared = 4*k_boltz*T.*real(Z_rad);
pin_piston=sqrt(F_piston_squared)/Area_pist;

```


APPENDIX B. BATCH SIMULATION OF THE NONLINEAR LUMPED LARGE SIGNAL CMUT MODEL

Membrane-type arrays such as CMUTs are particularly susceptible to acoustic crosstalk, which can impact their performance especially in terms of bandwidth. Accurate simulation of acoustic crosstalk and modeling of full arrays are therefore required to evaluate the performance of CMUT arrays. Full CMUT arrays can be comprised of several hundred to thousands of membranes, which would require considerable computational effort to simulate using standard 3-D finite element analysis (FEA). The transient nonlinear lumped large signal CMUT model reduces the complexity of these simulations by compressing the problem from three dimensions to two dimensions. The acousto-mechanical coupling is solved over a surface mesh of the CMUT array, where equilibrium for the mesh nodes are described in terms of lumped mass, damping, stiffness, and radiation impedance. After Fourier decomposition, the full mechanical system forms a matrix equation composed of frequency independent mass, damping, and stiffness matrices, and a frequency dependent mutual acoustic impedance matrix. Due to the frequency dependent nature of the matrix equation, transient performance analysis of CMUT arrays require solving the mechanical system across a range of frequencies which is then converted into multi-input multi-output (MIMO) finite impulse response (FIR) filters. Unfortunately, the lumped CMUT model suffers from unsatisfactory memory and run-time scaling due to its dependence on a fully populated mutual impedance matrix. One method that can be utilized to overcome these limiting issues is incorporating batch simulation into the simulation process.

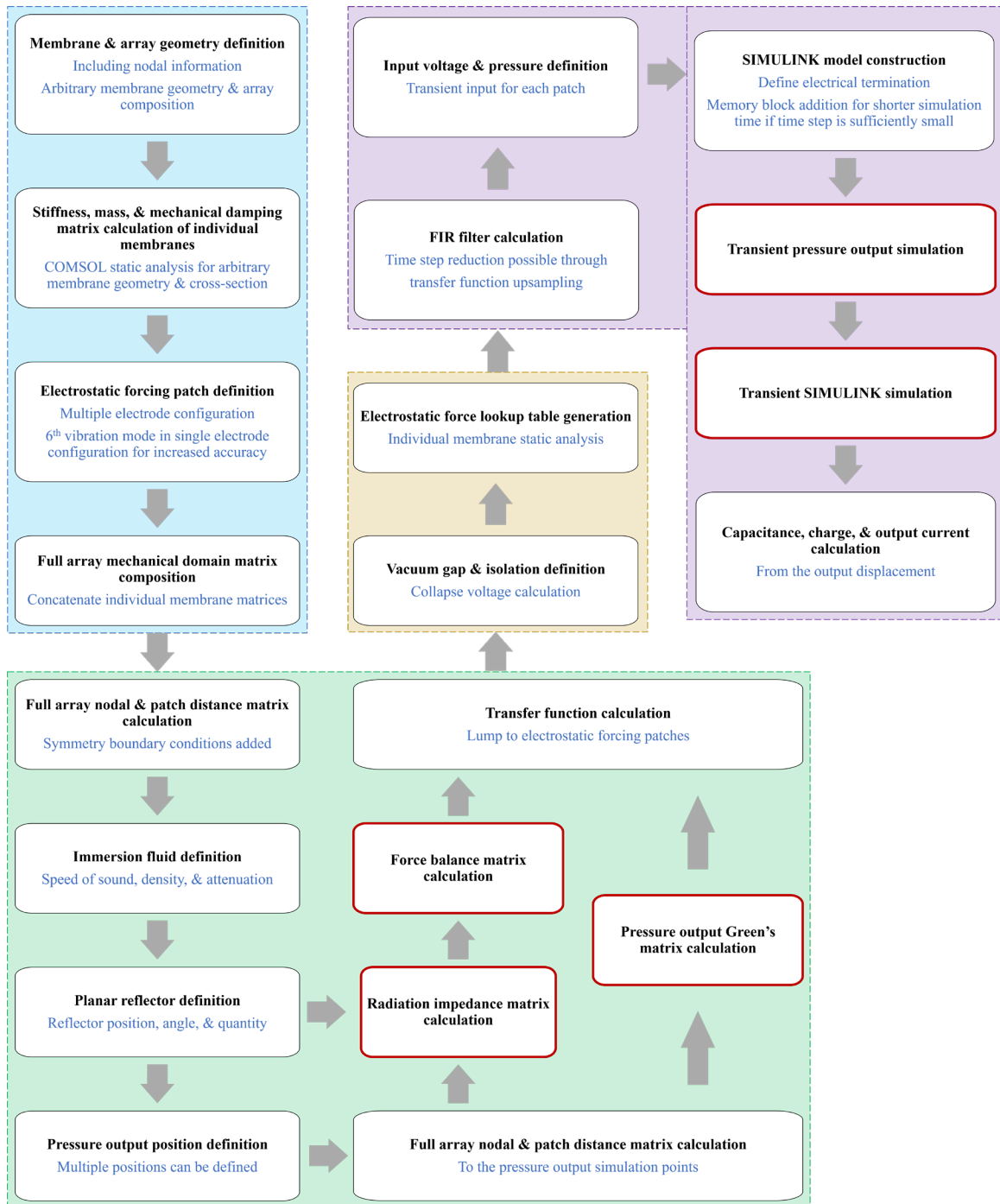
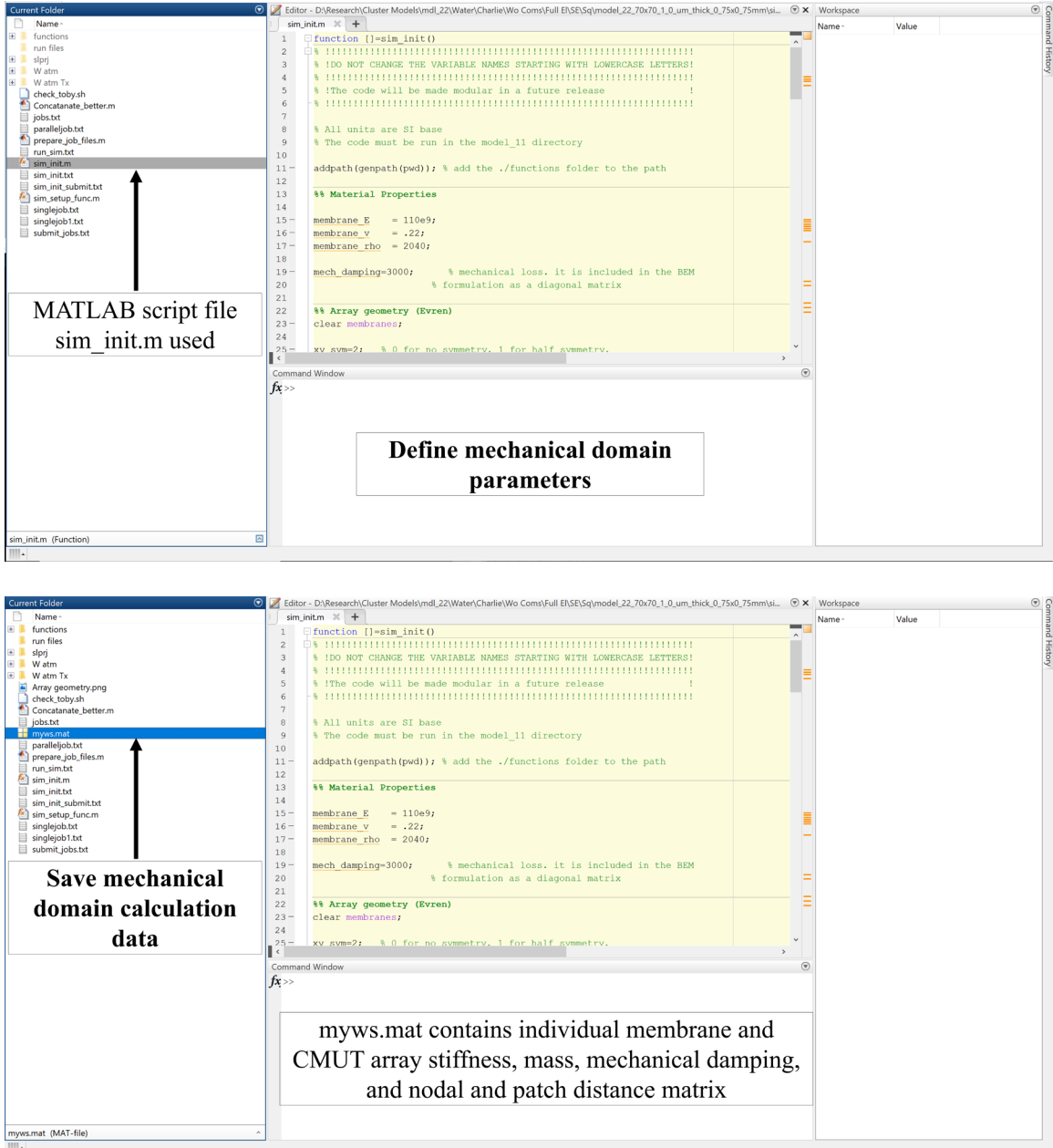


Figure B.1: Transient CMUT array modeling flow chart. Different calculation domains are highlighted in different shading. Batch simulation can be conducted on blocks with red outline.

The standard simulation process using the lumped large signal CMUT model can be observed in Figure B.1. The modeling process can be divided into the different physical domains of CMUT array operation, denoted in the figure as blue shading for mechanical domain, green shading for vibroacoustic domain, yellow shading for electrostatic domain, and purple shading for the SIMULINK simulation domain. The computation limiting issues are observed mainly in the vibroacoustic domain, where the bulk of the frequency dependent calculations are present. Computational effort and time of the complete vibroacoustic system calculation can be significantly reduced through the batch simulation of the system at different frequencies. The frequency range of interest is divided into smaller sets, and the equation of motion and pressure transfer functions are calculated in as a multiple set of simulations. Clusters provided by the Partnership for an Advanced Computing Environment (PACE) enable parallel computation of the multiple set of simulations, further reducing the computation time. The frequency dependent transfer functions are then concatenated, forming the necessary FIR filters for the transient simulation. PACE clusters also enable batch simulation of transient SIMULINK models, allowing faster optimization of CMUT array design. Through running multiple transient simulations in parallel, faster analysis of design parameters of the electrical domain, such as electrical termination, transmitter pulsing method, vacuum gap, and DC bias, can be conducted. Furthermore, the increased computational capabilities provided by PACE clusters enable simulation of larger and more complex CMUT arrays, reducing approximation in CMUT array performance analysis. Access to PACE clusters can be obtained by applying online and completing the orientation supplied once every two weeks. Afterwards, the required simulations can be uploaded to the clusters using a Secure File

Transfer Protocol (SFTP) client and submitted using a secure shell (SSH) client. To further illustrate how batch simulation and the PACE clusters are utilized, a step-by-step run-through of the CMUT modeling process is shown in Figure B.2.



Current Folder

- functions
- run files
- slprj
- W atm
- W atm Tx
- Array geometry.png
- check_toby.sh
- Concatenate_better.m
- jobs.txt
- myws.mat
- paralleljob.txt
- prepare_job_files.m
- run_sim.txt
- sim_init.m
- sim_init.txt
- sim_init_submit.txt
- sim_setup_func.m
- singlejob.txt
- singlejob1.txt
- submit_jobs.txt

Editor - D:\Research\Cluster Models\mdl_22\Water\Charlie\Wo Coms\Full EIS\ESQ\model_22_70x70_1_0_um_thick_0.75x0.75mm\sl...

```

31 %%
32 %%
33 % alpha=17*(f./1e6).^1.7; % Oil attenuation
34 % alpha=0*f; % No attenuation
35 % alpha=2.17e-1*(f./1e6).^2; % Water attenuation
36 % alpha=5.46*(f./1e6).^1.58; % Whole blood attenuation [0 70 MHz] [Treeby]
37
38 %%
39
40 lz=5e-3; % distance between CMUT array and hard reflector
41
42 wall_type=-1; % 1 for hard wall, -1 for soft wall
43
44 num_of_ref=0; % Number of reflections to be included in calculation
45 % num_of_ref=0 if there is no reflector
46
47 theta=0; %angles in beam pattern
48
49 x0s=zeros(numel(theta),3);
50 z0=2*lz;
51
52 for ind=1:numel(theta)

```

Workspace

Command Window

```
fx>>
```

sim_setup_func.m (Function)

- sim_setup_func(f_start, f_end, f_res, batchno)

MATLAB script file sim_setup_func.m used

Define vibroacoustic domain parameters

Current Folder

- functions
- run files
- slprj
- W atm
- W atm Tx
- Array geometry.png
- check_toby.sh
- Concatenate_better.m
- jobs.txt
- myws.mat
- paralleljob.txt
- prepare_job_files.m
- run_sim.txt
- sim_init.m
- sim_init.txt
- sim_init_submit.txt
- sim_setup_func.m
- singlejob.txt
- singlejob1.txt
- submit_jobs.txt

Editor - D:\Research\Cluster Models\mdl_22\Water\Charlie\Wo Coms\Full EIS\ESQ\model_22_70x70_1_0_um_thick_0.75x0.75mm\ch...

```

1 #!bin/sh
2 fend=50000000;
3 f_res=5000;
4
5 jobs_start=1;
6 jobs_end=10;
7 jobs=10;
8
9 ftemp='expr $fend / $jobs';
10
11 for (( i=jobs_start; i<=$jobs_end; i++ ))
12
13 do
14
15 fstart='expr $i \* $ftemp - $ftemp + $f_res';
16
17 fend='expr $i \* $ftemp';
18
19 file="myws$i.mat"
20
21 if [ ! -f "$file" ]
22
23 then
24
25 echo "I can not find $i ??????????"
26 #echo "Let's do it again !!!!!!!!!!!!!"

```

Workspace

Command Window

```
fx>>
```

check_toby.sh (SH File)

Portable batch system script file check_toby.sh used to check for completed simulation sets and submits the missing sets

Define and divide the frequency range of vibroacoustic domain calculations

Define PACE simulation parameters

```

1 #PBS -N paralleljob
2 #PBS -q force-6
3 #PBS -l walltime=12:00:00
4 #PBS -l nodes=1:ppn=1
5 #PBS -l mem=16gb
6 #PBS -j oe
7 #PBS -o paralleljob.$PBS_JOBID
8
9 cd $PBS_O_WORKDIR
10
11 module load matlab/r2018a
12
13 #JOBFILE, BATCHSIZE, and BATCHNUM should be set in the environment
14 #If they are not, use some defaults.
15 # By setting BATCHSIZE to a default of the length of the jobfile we only require one of these
16 # The user can submit multiple jobs and split up the batchcount to work on multiple nodes
17 matlab -nodisplay -singleCompThread -r "sim_setup_func(45005000,50000000,5000,10)"
18

```

singlejob.txt is used
A new singlejob.txt is generated for each frequency range determined by check_toby.sh

Upload files to PACE
SFTP client WinSCP connected to iw-dm-4.pace.gatech.edu

Name	Size	Type	Changed	Name	Size	Changed	Right
functions		File folder	3/27/2020 5:14:04 PM	functions	54 KB	3/27/2020 5:29:43 PM	rw-r
run files		File folder	3/25/2020 1:09:56 PM	run files	1 KB	3/27/2020 5:29:45 PM	rw-r
slipj		File folder	3/25/2020 1:09:56 PM	slipj	4 KB	3/27/2020 5:30:25 PM	rw-r
W atm		File folder	3/25/2020 1:09:56 PM	W atm	3 KB	3/27/2020 5:30:28 PM	rw-r
W atm Tx		File folder	3/25/2020 1:10:00 PM	W atm Tx	1 KB	5/4/2019 8:31:20 PM	rw-r
Array geometry.png	54 KB	PNG File	3/27/2020 5:13:48 PM	Concatenate_betterm	1 KB	3/27/2020 5:17:00 PM	rw-r
check_toby.sh	1 KB	SH File	4/6/2019 4:04:07 PM	prepare_job_files.m	4 KB	3/27/2020 4:58:46 PM	rw-r
Concatenate_betterm	1 KB	MATLAB Code	5/4/2019 8:31:20 PM	sim_init.m	3 KB	2/17/2020 6:44:11 PM	rw-r
jobs.txt	1 KB	Text Document	3/27/2020 5:17:38 PM	sim_setup_func.m	148,662 KB	3/27/2020 5:10:47 PM	rw-r
myws.mat	148,662 KB	MATLAB Data	3/27/2020 5:10:47 PM	myws.mat	54 KB	3/27/2020 5:13:48 PM	rw-r
paralleljob.txt	2 KB	Text Document			1 KB	4/6/2019 4:04:07 PM	rw-r
prepare_job_files.m	1 KB	MATLAB Code			1 KB	3/27/2020 5:17:38 PM	rw-r
run_sim.txt	1 KB	Text Document			1 KB	11/13/2014 12:25:00 AM	rw-r
sim_init.m	1 KB	Text Document			1 KB	4/10/2017 12:13:21 PM	rw-r
sim_init.txt	1 KB	Text Document			1 KB	11/11/2014 8:18:54 PM	rw-r
sim_init_submitt.txt	1 KB	Text Document			1 KB	3/27/2020 5:19:19 PM	rw-r
sim_setup_func.m	3 KB	MATLAB Code			1 KB	3/27/2020 5:23:32 PM	rw-r
singlejob.txt	1 KB	Text Document			13 KB	3/27/2020 5:17:03 PM	rw-r
singlejob1.txt	1 KB	Text Document					
submit_jobs.txt	13 KB	Text Document					

```

login-s-pace.gtm.gatech.edu - PuTTY
login as: earkan3
earkan3@login-s-pace.gatech.edu's password:
Last login: Mon Mar 16 18:45:07 2020 from me01050.me.gatech.edu
Terms of Use

This computer system is the property of Georgia Institute of
Technology. Any users of this system must comply with all Institute
and Board of Regents policies, including the Acceptable Use
Policy (AUP), Data Privacy Policy (DPP) and Cyber Security
Policy (CSP), see http://b.gatech.edu/it-policies. Users should
have no expectation of privacy, as any and all files on this system
may be intercepted, monitored, copied, inspected, and/or disclosed to
authorized personnel in order to meet institute obligations.

By using this system, I acknowledge and consent to these terms.

To see the current status of a queue, please run
"pace-check-queue <queue name>".

If you require assistance with this system, please run "pace-support.sh"

[earkan3@login-s3 ~]$ cd data
[earkan3@login-s3 data]$ cd model_22
[earkan3@login-s3 model_22]$ cd Charlie
[earkan3@login-s3 Charlie]$ ls
model_22_70x70_1_0_um_thick_0_75x0_75mm
[earkan3@login-s3 Charlie]$ cd model_22_70x70_1_0_um_thick_0_75x0_75mm
[earkan3@login-s3 model_22_70x70_1_0_um_thick_0_75x0_75mm]$ sh check_toby.sh
I can not find 1 ??????????????

28249407
I can not find 2 ??????????????

28249408
I can not find 3 ??????????????

28249410
I can not find 4 ??????????????

28249411
I can not find 5 ??????????????

28249412
I can not find 6 ??????????????

28249413
I can not find 7 ??????????????

28249416
I can not find 8 ??????????????

28249417
I can not find 9 ??????????????

28249418
I can not find 10 ??????????????

28249420
[earkan3@login-s3 model_22_70x70_1_0_um_thick_0_75x0_75mm]$

```

Submit and run the multiple set of vibroacoustic domain calculations

SSH client PuTTY connected to login-s.pace.gatech.edu

Download vibroacoustic domain calculations from PACE

mat files myws1-10 contain transfer function data in their respective frequency range

Current Folder

- functions
- run files
- slprj
- W atm
- W atm Tx
- Array geometry.png
- check_tobysh
- Concatenate_better.m
- jobs.txt
- myws.mat
- myws1.mat
- myws2.mat
- myws3.mat
- myws4.mat
- myws5.mat
- myws6.mat
- myws7.mat
- myws8.mat
- myws9.mat
- myws10.mat
- paralleljob.txt
- prepare_job_files.m
- run_sim.txt
- sim_init.m
- sim_init.txt
- sim_init_submit.txt
- sim_setup_func.m
- singlejob.txt
- submit_jobs.txt

Concatenate_better.m (Script)

F2U_TF

MATLAB script file Concatenate_better.m used

```

1 clear all
2 clc
3
4 jobno=10;
5
6 load(['myws1'])
7
8 F2U_TF_temp=cell(size(F2U_TF));
9
10 F2P_TF_temp=cell(size(F2P_TF_full));
11
12 for say1=1:size(F2P_TF_full,2)
13     F2P_TF_temp(say1)=cell(size(F2P_TF_full(1,1)));
14 end
15
16
17 for job_ind=1:jobno
18     load(['myws'+ num2str(job_ind)])
19
20
21     %%F2U_TF
22     for ind=1:size(F2U_TF,1)
23         for ind2=1:size(F2U_TF,2)
24             F2U_TF_temp(ind,ind2)=F2U_TF(ind,ind2);
25         end
26     end

```

Concatenate the multiple vibroacoustic domain calculations

Workspace

Command History

Command Window

Ln 1 Col 9

Current Folder

- functions
- run files
- slprj
- W atm
- W atm Tx
- Array geometry.png
- check_tobysh
- Concatenate_better.m
- jobs.txt
- myTF.mat
- myws.mat
- paralleljob.txt
- prepare_job_files.m
- run_sim.txt
- sim_init.m
- sim_init.txt
- sim_init_submit.txt
- sim_setup_func.m
- singlejob.txt
- submit_jobs.txt

myTF.mat (MAT-file)

Name	Value
F2P_TF_full	1x1 cell
F2U_TF	50x50 cell
f_end	50000000
f_res	5000
fluid_c	1500
fluid_rho	1000
lz	0.0050
theta	0
xbs	[0,0,0,0,100]

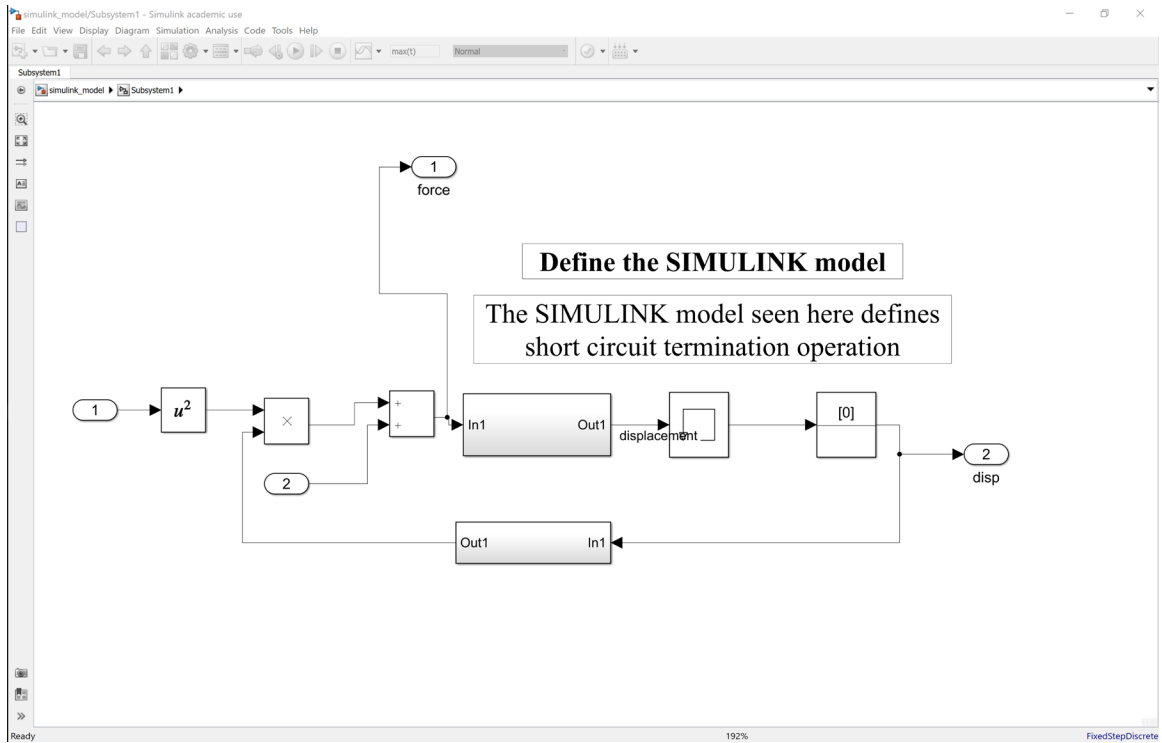
Save vibroacoustic transfer functions

myTF.mat contains CMUT array force to velocity and force to pressure output transfer functions across the complete frequency range

Workspace

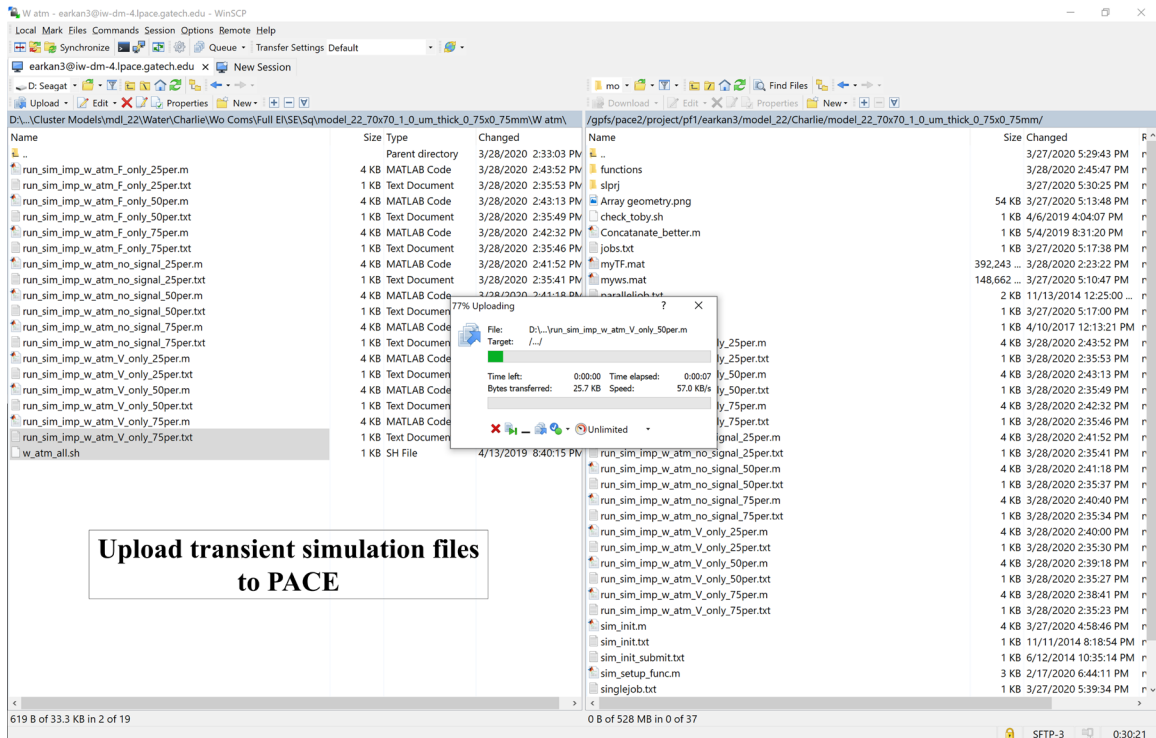
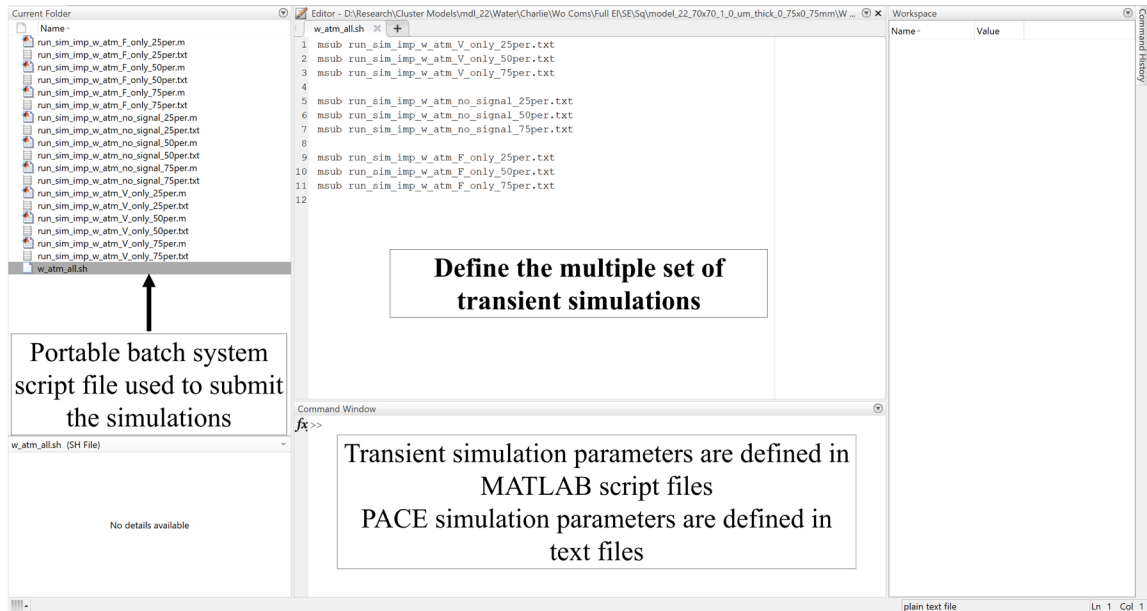
Command History

Command Window



Upload transfer functions and SIMULINK model to PACE

Name	Size	Type	Changed	Name	Size	Changed	Rights
..		Parent directory	3/28/2020 2:21:07 PM	..		3/27/2020 5:29:43 PM	rxwx
functions		File folder	3/25/2020 1:09:56 PM	functions		3/27/2020 5:29:43 PM	rxwx
run files		File folder	3/25/2020 1:05:04 PM	slprj		3/27/2020 5:30:25 PM	rxwx
slprj		File folder	3/25/2020 1:09:56 PM	Array geometry.png	54 KB	3/27/2020 5:13:48 PM	rw+
W atm		File folder	3/25/2020 1:09:58 PM	check_toby.sh	1 KB	4/6/2019 4:04:07 PM	rw+
W atm Tx		File folder	3/25/2020 1:10:00 PM	Concatenate_better.m	1 KB	5/4/2019 8:31:20 PM	rw+
Array geometry.png	54 KB	PNG File	3/27/2020 5:13:48 PM	jobs.txt	1 KB	3/27/2020 5:17:38 PM	rw+
check_toby.sh	1 KB	SH File	4/6/2019 4:04:07 PM	myws.mat	148,662 ...	3/27/2020 5:10:47 PM	rw+
Concatenate_better.m	1 KB	MATLAB Code	3/28/2020 2:23:02 PM	paralleljob.txt	2 KB	11/13/2014 12:25:00 ...	rw+
jobs.txt	1 KB	Text Document	3/27/2020 5:17:38 PM	paralleljob.txt	1 KB	3/27/2020 5:17:00 PM	rw+
myTF.mat	392,243 ...	MATLAB Data		paralleljob.txt	4 KB	3/27/2020 4:58:46 PM	rw+
myws.mat	148,662 ...	MATLAB Data		paralleljob.txt	1 KB	11/11/2014 8:18:54 PM	rw+
paralleljob.txt	2 KB	Text Document		paralleljob.txt	1 KB	6/12/2014 10:35:14 PM	rw+
prepare_job_files.m	1 KB	MATLAB Code		paralleljob.txt	3 KB	2/17/2020 6:44:11 PM	rw+
sim_init.m	4 KB	MATLAB Code		paralleljob.txt	1 KB	3/27/2020 5:39:34 PM	rw+
sim_init.txt	1 KB	Text Document		paralleljob.txt	1 KB	3/27/2020 5:40:14 PM	rw+
sim_init_submit.txt	1 KB	Text Document		paralleljob.txt	1 KB	3/27/2020 5:17:03 PM	rw+
sim_setup_func.m	3 KB	MATLAB Code					
singlejob.txt	1 KB	Text Document					
singlejob1.txt	1 KB	Text Document	3/27/2020 5:23:32 PM				
submit_jobs.txt	13 KB	Text Document	3/27/2020 5:17:03 PM				



```

login-s-space.gtm.gatech.edu - PuTTY
login as: earkan3
earkan3@login-s.pace.gatech.edu's password:
Last login: Thu Mar 5 16:06:03 2020 from me01050.me.gatech.edu
Terms of Use

This computer system is the property of Georgia Institute of
Technology. Any user of this system must comply with all Institute
and Board of Regents policies, including the Acceptable Use
Policy (AUP), Data Privacy Policy (DPP) and Cyber Security
Policy (CSP), see http://b.gatech.edu/it-policies. Users should
have no expectation of privacy, as any and all files on this system
may be intercepted, monitored, copied, inspected, and/or disclosed to
authorized personnel in order to meet institute obligations.

By using this system, I acknowledge and consent to these terms.

To see the current status of a queue, please run
"pace-check-queue <queue name>".

If you require assistance with this system, please run "pace-support.sh"

[earkan3@login-s4 ~]$ cd data
[earkan3@login-s4 data]$ cd model_22
[earkan3@login-s4 model_22]$ cd Charlie
[earkan3@login-s4 Charlie]$ cd model_22_70x70_1_0_um_thick_0_75x0_75mm
[earkan3@login-s4 model_22_70x70_1_0_um_thick_0_75x0_75mm]$ sh w_atm_all.sh

28265509
28265510
28265512
28265514
28265515
28265518
28265519
28265521
28265522
[earkan3@login-s4 model_22_70x70_1_0_um_thick_0_75x0_75mm]$

```

Submit and run the multiple set of transient simulations

The screenshot shows a Windows File Explorer window with the following details:

- Path:** Z:\home\Evren\SNR and Imp\Charlie\Imp\WoComs\SE\Ful EN70 um sq 1.0 um thick\0.75x0.75 mm\500nm gap max Si3N4 iso 63 Vcol
- Files:** A list of files including .mat files (e.g., current etc w atm 500 nm gap 16 V DC no signal up6.mat) and .txt files (e.g., run_sim_imp_w_atm_no_signal_25per.txt).
- Download Progress Window:** Shows a file named 'current etc w atm 500 nm gap 16 V DC no signal up6.mat' being downloaded from 'Z:\...500nm gap max Si3N4 iso 63 Vcol'. The progress is at 9%.
- Annotations:**
 - A box with an arrow pointing to the files: "Transient simulation output saved as mat files"
 - A box at the bottom: "Download transient simulation results from PACE"

Figure B.2: Step-by-step run-through of the CMUT array modeling process with PACE clusters.

REFERENCES

- [1] T. L. Szabo, "Chapter 1 - Introduction," in *Diagnostic Ultrasound Imaging: Inside Out (Second Edition)*. Boston: Academic Press, 2014, pp. 1-37.
- [2] C. C. Shih, C. C. Huang, Q. Zhou, and K. K. Shung, "High-resolution acoustic-radiation-force-impulse imaging for assessing corneal sclerosis," *IEEE Transactions on Medical Imaging*, vol. 32, no. 7, pp. 1316-1324, 2013, doi: 10.1109/TMI.2013.2256794.
- [3] D. Rohrbach, H. O. Lloyd, R. H. Silverman, and J. Mamou, "Fine-resolution maps of acoustic properties at 250 MHz of unstained fixed murine retinal layers," *The Journal of the Acoustical Society of America*, vol. 137, no. 5, pp. EL381-7, 2015, doi: 10.1121/1.4916790.
- [4] T. H. Bok, J. Kim, J. Bae, C. H. Lee, and D. G. Paeng, "Implementation of a rotational ultrasound biomicroscopy system equipped with a high-frequency angled needle transducer — Ex vivo ultrasound imaging of porcine ocular posterior tissues," *Sensors (Switzerland)*, vol. 14, no. 9, pp. 17807-17816, 2014, doi: 10.3390/s140917807.
- [5] R. K. Mlosek, R. M. De bowska, M. Lewandowski, S. Malinowska, A. Nowicki, and I. Eris, "Imaging of the skin and subcutaneous tissue using classical and high-frequency ultrasonographies in anti-cellulite therapy," *Skin Research and Technology*, vol. 17, no. 4, pp. 461-468, 2011, doi: 10.1111/j.1600-0846.2011.00519.x.
- [6] K. Kumagai, H. Koike, R. Nagaoka, S. Sakai, K. Kobayashi, and Y. Saijo, "High-Resolution Ultrasound Imaging of Human Skin In Vivo by Using Three-Dimensional Ultrasound Microscopy," *Ultrasound in Medicine and Biology*, vol. 38, no. 10, pp. 1833-1838, 2012, doi: 10.1016/j.ultrasmedbio.2012.05.012.
- [7] M. Maj *et al.*, "High frequency ultrasonography: a complementary diagnostic method in evaluation of primary cutaneous melanoma," *Giornale italiano di dermatologia e venereologia : organo ufficiale, Societa italiana di dermatologia e sifilografia*, vol. 150, no. 5, pp. 595-601, 2015. [Online]. Available: <http://www.ncbi.nlm.nih.gov/pubmed/26333555>.
- [8] T. Ma, M. Yu, Z. Chen, C. Fei, K. Shung, and Q. Zhou, "Multi-frequency intravascular ultrasound (IVUS) imaging," *IEEE Transactions on Ultrasonics, Ferroelectrics, and Frequency Control*, vol. 62, no. 1, pp. 97-107, 2015, doi: 10.1109/TUFFC.2014.006679.

- [9] X. Li *et al.*, "Integrated IVUS-OCT Imaging for Atherosclerotic Plaque Characterization," *IEEE Journal on Selected Topics in Quantum Electronics*, vol. 20, no. 2, 2014, doi: 10.1109/JSTQE.2013.2274724.
- [10] X. Li *et al.*, "80-MHz intravascular ultrasound transducer using PMN-PT free-standing film," *IEEE Transactions on Ultrasonics, Ferroelectrics, and Frequency Control*, vol. 58, no. 11, pp. 2281-2288, 2011, doi: 10.1109/TUFFC.2011.2085.
- [11] K. Jansen, Y. Gijss, V. Soest, and A. F. W. Van Der Steen, "INTRAVASCULAR PHOTOACOUSTIC IMAGING: A NEW TOOL FOR VULNERABLE PLAQUE IDENTIFICATION," *Ultrasound in Medicine & Biology*, vol. 40, pp. 1037-1048, 2014, doi: 10.1016/j.ultrasmedbio.2014.01.008.
- [12] O. Aristizábal *et al.*, "Simultaneous photoacoustic and high-frequency ultrasound imaging of in vivo embryonic-mouse vasculature," in *2011 IEEE International Ultrasonics Symposium*, 18-21 Oct. 2011 2011, pp. 288-291, doi: 10.1109/ULTSYM.2011.0069.
- [13] N. Q. Bui *et al.*, "Intravascular ultrasonic-photoacoustic (IVUP) endoscope with 2.2-mm diameter catheter for medical imaging," *Computerized Medical Imaging and Graphics*, vol. 45, pp. 57-62, 2015, doi: 10.1016/j.compmedimag.2015.07.008.
- [14] B. Wang *et al.*, "In vivo Intravascular Ultrasound-guided Photoacoustic Imaging of Lipid in Plaques Using an Animal Model of Atherosclerosis," *Ultrasound in Medicine & Biology*, vol. 38, no. 12, pp. 2098-2103, 2012/12/01/ 2012, doi: <https://doi.org/10.1016/j.ultrasmedbio.2012.08.006>.
- [15] G. C. Kagadis, G. Loudos, K. Katsanos, S. G. Langer, and G. C. Nikiforidis, "In vivo small animal imaging: Current status and future prospects," *Medical Physics*, vol. 37, no. 12, pp. 6421-6442, 2010/12/01 2010, doi: 10.1118/1.3515456.
- [16] S. E. Shelton, P. A. Dayton, S. R. Aylward, and F. S. Foster, "The application of acoustic angiography to assess the progression of angiogenesis in a spontaneous mouse model of breast cancer," in *2016 IEEE International Ultrasonics Symposium (IUS)*, 18-21 Sept. 2016 2016, pp. 1-3, doi: 10.1109/ULTSYM.2016.7728697.
- [17] T. Y. Liu, P. Y. Lee, C. C. Huang, L. Sun, and K. K. Shung, "A study of the adult zebrafish ventricular function by retrospective doppler-gated ultrahigh-frame-rate echocardiography," *IEEE Transactions on Ultrasonics, Ferroelectrics, and Frequency Control*, vol. 60, no. 9, pp. 1827-1837, 2013, doi: 10.1109/TUFFC.2013.2769.
- [18] L. Zhang *et al.*, "A high-frequency, high frame rate duplex ultrasound linear array imaging system for small animal imaging," *IEEE Transactions on Ultrasonics, Ferroelectrics, and Frequency Control*, vol. 57, no. 7, pp. 1548-1557, 2010, doi: 10.1109/TUFFC.2010.1585.

- [19] K. K. Shung, "High Frequency Ultrasonic Imaging," *Journal of Medical Ultrasound*, vol. 17, no. 1, pp. 25-30, 2009, doi: [https://doi.org/10.1016/S0929-6441\(09\)60012-6](https://doi.org/10.1016/S0929-6441(09)60012-6).
- [20] K. Uchino, "Piezoelectric ceramics for transducers," in *Ultrasonic Transducers*, K. Nakamura Ed.: Woodhead Publishing, 2012, ch. 3, pp. 70-116.
- [21] M. Pekař, W. U. Dittmer, N. Mihajlović, G. van Soest, and N. de Jong, "Frequency Tuning of Collapse-Mode Capacitive Micromachined Ultrasonic Transducer," *Ultrasonics*, vol. 74, pp. 144-152, 2017/02/01/ 2017, doi: <https://doi.org/10.1016/j.ultras.2016.10.002>.
- [22] M. Pekař *et al.*, "Frequency-agility of collapse-mode 1-D CMUT array," in *2016 IEEE International Ultrasonics Symposium (IUS)*, 18-21 Sept. 2016 2016, pp. 1-3, doi: 10.1109/ULTSYM.2016.7728467.
- [23] S. Olcum, F. Y. Yamaner, A. Bozkurt, H. Köymen, and A. Atalar, "CMUT array element in deep-collapse mode," in *2011 IEEE International Ultrasonics Symposium*, 18-21 Oct. 2011 2011, pp. 108-111, doi: 10.1109/ULTSYM.2011.0027.
- [24] Y. Huang *et al.*, "Comparison of conventional and collapsed region operation of capacitive micromachined ultrasonic transducers," *IEEE Transactions on Ultrasonics, Ferroelectrics, and Frequency Control*, vol. 53, no. 10, pp. 1918-1933, 2006, doi: 10.1109/TUFFC.2006.125.
- [25] K. K. Park, O. Oralkan, and B. T. Khuri-Yakub, "Comparison of conventional and collapse-mode CMUT in 1-D array configuration," in *2011 IEEE International Ultrasonics Symposium*, 18-21 Oct. 2011 2011, pp. 1000-1003, doi: 10.1109/ULTSYM.2011.0245.
- [26] K. K. Park, O. Oralkan, and B. T. Khuri-Yakub, "A comparison between conventional and collapse-mode capacitive micromachined ultrasonic transducers in 10-MHz 1-D arrays," *IEEE Transactions on Ultrasonics, Ferroelectrics, and Frequency Control*, vol. 60, no. 6, pp. 1245-1255, 2013, doi: 10.1109/TUFFC.2013.2688.
- [27] D. T. Yeh, O. Oralkan, A. S. Ergun, X. F. Zhuang, I. O. Wygant, and B. T. Khuri-Yakub, "High-frequency CMUT arrays for high-resolution medical imaging," in *Medical Imaging 2005 Conference*, San Diego, CA, 2005, vol. 5750, pp. 87-98, doi: 10.1117/12.595918. [Online]. Available: <Go to ISI>://WOS:000229069500010
- [28] J. W. Hunt, M. Arditi, and F. S. Foster, "Ultrasound Transducers for Pulse-Echo Medical Imaging," *IEEE Transactions on Biomedical Engineering*, vol. BME-30, no. 8, pp. 453-481, 1983, doi: 10.1109/TBME.1983.325150.

- [29] H. J. Lee, S. Zhang, Y. Bar-Cohen, and S. Sherrit, "High temperature, high power piezoelectric composite transducers," (in eng), *Sensors (Basel)*, vol. 14, no. 8, pp. 14526-14552, 2014, doi: 10.3390/s140814526.
- [30] T. Cummins, P. Eliahoo, and K. K. Shung, "High-Frequency Ultrasound Array Designed for Ultrasound-Guided Breast Biopsy," *IEEE Transactions on Ultrasonics, Ferroelectrics, and Frequency Control*, vol. 63, no. 6, pp. 817-827, 2016, doi: 10.1109/TUFFC.2016.2548993.
- [31] C. Liu, Q. Zhou, F. T. Djuth, and K. K. Shung, "High-frequency (>50 MHz) medical ultrasound linear arrays fabricated from micromachined bulk PZT materials," *IEEE Transactions on Ultrasonics, Ferroelectrics, and Frequency Control*, vol. 59, no. 2, pp. 315-318, 2012, doi: 10.1109/TUFFC.2012.2193.
- [32] Q. Zhou, D. Wu, C. Liu, B. Zhu, F. Djuth, and K. K. Shung, "Micro-machined high-frequency (80 MHz) PZT thick film linear arrays," *IEEE Transactions on Ultrasonics, Ferroelectrics, and Frequency Control*, vol. 57, no. 10, pp. 2213-2220, 2010, doi: 10.1109/TUFFC.2010.1680.
- [33] A. Bezanson, R. Adamson, and J. A. Brown, "Fabrication and performance of a miniaturized 64-element high-frequency endoscopic phased array," *IEEE Transactions on Ultrasonics, Ferroelectrics, and Frequency Control*, vol. 61, no. 1, pp. 33-43, 2014, doi: 10.1109/TUFFC.2014.6689774.
- [34] F. S. Foster *et al.*, "A New 15-50 MHz Array-Based Micro-Ultrasound Scanner for Preclinical Imaging," *Ultrasound in Medicine and Biology*, vol. 35, no. 10, pp. 1700-1708, 2009, doi: 10.1016/j.ultrasmedbio.2009.04.012.
- [35] D. W. Wu, Q. Zhou, X. Geng, C. G. Liu, F. Djuth, and K. K. Shung, "Very high frequency (beyond 100 MHz) PZT kerfless linear arrays," *IEEE Transactions on Ultrasonics, Ferroelectrics, and Frequency Control*, vol. 56, no. 10, pp. 2304-2310, 2009, doi: 10.1109/TUFFC.2009.1311.
- [36] K. Brenner, S. A. Ergun, K. Firouzi, F. M. Rasmussen, Q. Stedman, and Khuri-Yakub, "Advances in Capacitive Micromachined Ultrasonic Transducers," *Micromachines*, vol. 10, no. 2, 2019, doi: 10.3390/mi10020152.
- [37] K. K. Park, H. Lee, M. Kupnik, and B. T. Khuri-Yakub, "Fabrication of Capacitive Micromachined Ultrasonic Transducers via Local Oxidation and Direct Wafer Bonding," *Journal of Microelectromechanical Systems*, vol. 20, no. 1, pp. 95-103, 2011, doi: 10.1109/JMEMS.2010.2093567.
- [38] G. K. Fedder, R. T. Howe, T. K. Liu, and E. P. Quevy, "Technologies for Cofabricating MEMS and Electronics," *Proceedings of the IEEE*, vol. 96, no. 2, pp. 306-322, 2008, doi: 10.1109/JPROC.2007.911064.
- [39] D. Wildes *et al.*, "4-D ICE: A 2-D Array Transducer With Integrated ASIC in a 10-Fr Catheter for Real-Time 3-D Intracardiac Echocardiography," *IEEE Transactions*

on Ultrasonics, Ferroelectrics, and Frequency Control, vol. 63, no. 12, pp. 2159-2173, 2016, doi: 10.1109/TUFFC.2016.2615602.

- [40] V. Daeichin *et al.*, "Acoustic Characterization of a Miniature Matrix Transducer for Pediatric 3d Transesophageal Echocardiography," (in English), *Ultrasound in Medicine and Biology*, vol. 44, no. 10, pp. 2143-2154, Oct 2018, doi: 10.1016/j.ultrasmedbio.2018.06.009.
- [41] J. Song *et al.*, *Reconfigurable 2D cMUT-ASIC arrays for 3D ultrasound image* (SPIE Medical Imaging). SPIE, 2012.
- [42] I. O. Wygant *et al.*, "Integration of 2D CMUT arrays with front-end electronics for volumetric ultrasound imaging," *IEEE Transactions on Ultrasonics, Ferroelectrics, and Frequency Control*, vol. 55, no. 2, pp. 327-342, 2008, doi: 10.1109/TUFFC.2008.652.
- [43] I. O. Wygant *et al.*, "An integrated circuit with transmit beamforming flip-chip bonded to a 2-D CMUT array for 3-D ultrasound imaging," *IEEE Transactions on Ultrasonics, Ferroelectrics, and Frequency Control*, vol. 56, no. 10, pp. 2145-2156, 2009, doi: 10.1109/TUFFC.2009.1297.
- [44] A. Bhuyan *et al.*, "Integrated Circuits for Volumetric Ultrasound Imaging With 2-D CMUT Arrays," *IEEE Transactions on Biomedical Circuits and Systems*, vol. 7, no. 6, pp. 796-804, 2013, doi: 10.1109/TBCAS.2014.2298197.
- [45] O. Oralkan *et al.*, "Volumetric ultrasound imaging using 2-D CMUT arrays," *IEEE Transactions on Ultrasonics, Ferroelectrics, and Frequency Control*, vol. 50, no. 11, pp. 1581-1594, 2003, doi: 10.1109/TUFFC.2003.1251142.
- [46] A. Nikoozadeh *et al.*, "Forward-looking intracardiac ultrasound imaging using a 1-D CMUT array integrated with custom front-end electronics," *IEEE Transactions on Ultrasonics, Ferroelectrics, and Frequency Control*, vol. 55, no. 12, pp. 2651-2660, 2008, doi: 10.1109/TUFFC.2008.980.
- [47] J. H. Jang *et al.*, "Dual-mode integrated circuit for imaging and HIFU with 2-D CMUT arrays," in *2015 IEEE International Ultrasonics Symposium (IUS)*, 21-24 Oct. 2015 2015, pp. 1-4, doi: 10.1109/ULTSYM.2015.0166.
- [48] T. Ma *et al.*, "3-D Deep penetration photoacoustic imaging with a 2-D CMUT array," in *2010 IEEE International Ultrasonics Symposium*, 11-14 Oct. 2010 2010, pp. 375-377, doi: 10.1109/ULTSYM.2010.5935647.
- [49] G. Jung *et al.*, "Single-Chip Reduced-Wire CMUT-on-CMOS System for Intracardiac Echocardiography," in *2018 IEEE International Ultrasonics Symposium (IUS)*, 22-25 Oct. 2018 2018, pp. 1-4, doi: 10.1109/ULTSYM.2018.8579915.

- [50] G. Gurun *et al.*, "Single-chip CMUT-on-CMOS front-end system for real-time volumetric IVUS and ICE imaging," *IEEE Transactions on Ultrasonics, Ferroelectrics, and Frequency Control*, vol. 61, no. 2, pp. 239-250, 2014, doi: 10.1109/TUFFC.2014.6722610.
- [51] M. Hochman *et al.*, "CMUT-on-CMOS for forward-looking IVUS: Improved fabrication and real-time imaging," in *2010 IEEE International Ultrasonics Symposium*, 11-14 Oct. 2010 2010, pp. 555-558, doi: 10.1109/ULTSYM.2010.5935979.
- [52] G. Gurun, P. Hasler, and F. Degertekin, "Front-end receiver electronics for high-frequency monolithic CMUT-on-CMOS imaging arrays," *IEEE transactions on ultrasonics, ferroelectrics, and frequency control*, vol. 58, no. 8, pp. 1658-1668, 2011, doi: 10.1109/TUFFC.2011.1993.
- [53] J. Zahorian *et al.*, "Monolithic CMUT-on-CMOS Integration for Intravascular Ultrasound Applications," *IEEE Transactions on Ultrasonics, Ferroelectrics, and Frequency Control*, vol. 58, no. 12, pp. 2659-2667, 2011, doi: 10.1109/TUFFC.2011.2128.
- [54] A. Şişman *et al.*, "Evaluation of CMUT annular arrays for side-looking IVUS," in *2009 IEEE International Ultrasonics Symposium*, 20-23 Sept. 2009 2009, pp. 2774-2777, doi: 10.1109/ULTSYM.2009.5441980.
- [55] T. Xu, C. Tekes, S. Satir, E. Arkan, M. Ghovanloo, and F. L. Degertekin, "Design, modeling and characterization of a 35MHz 1-D CMUT phased array," in *2013 IEEE International Ultrasonics Symposium (IUS)*, 21-25 July 2013 2013, pp. 1987-1990, doi: 10.1109/ULTSYM.2013.0507.
- [56] Z. Xiao, F. Y. Yamanery, O. Adelegan, and O. Ö, "Design of high-frequency broadband CMUT arrays," in *2015 IEEE International Ultrasonics Symposium (IUS)*, 21-24 Oct. 2015 2015, pp. 1-4, doi: 10.1109/ULTSYM.2015.0167.
- [57] O. Oralkan, S. T. Hansen, B. Bayram, G. G. Yaralioglu, A. S. Ergun, and B. T. Khuri-Yakub, "High-frequency CMUT arrays for high-resolution medical imaging," *IEEE Ultrasonics Symposium, 2004*, vol. 1, no. c, pp. 399-402, 2004, doi: 10.1109/ULTSYM.2004.1417747.
- [58] D. T. Yeh, O. Oralkan, I. O. Wygant, A. S. Ergun, J. H. Wong, and B. T. Khuri-Yakub, "High-resolution imaging with high-frequency 1-D linear CMUT arrays," in *IEEE Ultrasonics Symposium, 2005.*, 18-21 Sept. 2005 2005, vol. 1, pp. 665-668, doi: 10.1109/ULTSYM.2005.1602940.
- [59] S. D. Senturia, "Lumped-element System Dynamics," in *Microsystem Design*: Springer, Boston, MA, 2002, ch. 7, pp. 149-180.
- [60] I. Ladabaum, J. Xuecheng, H. T. Soh, A. Atalar, and B. t. Khuri-Yakub, "Surface micromachined capacitive ultrasonic transducers," *IEEE Transactions on*

Ultrasonics, Ferroelectrics, and Frequency Control, vol. 45, no. 3, pp. 678-690, 1998, doi: 10.1109/58.677612.

- [61] G. G. Yaralioglu, A. S. Ergun, B. Bayram, E. Haeggstrom, and B. T. Khuri-Yakub, "Calculation and measurement of electromechanical coupling coefficient of capacitive micromachined ultrasonic transducers," *IEEE Transactions on Ultrasonics, Ferroelectrics, and Frequency Control*, vol. 50, no. 4, pp. 449-456, 2003, doi: 10.1109/TUFFC.2003.1197968.
- [62] S. Satir, "Modeling and optimization of capacitive micromachined ultrasonic transducers," Doctoral Dissertation, Electrical and Computer Engineering, Georgia Institute of Technology, 2014. [Online]. Available: <http://hdl.handle.net/1853/54303>
- [63] E. F. Arkan and F. L. Degertekin, "Analysis and Design of High-Frequency 1-D CMUT Imaging Arrays in Noncollapsed Mode," (in English), *IEEE Transactions on Ultrasonics, Ferroelectrics, and Frequency Control*, vol. 66, no. 2, pp. 382-393, Feb 2019, doi: 10.1109/Tuffc.2018.2887043.
- [64] S. Satir, J. Zahorian, and F. L. Degertekin, "A large-signal model for CMUT arrays with arbitrary membrane geometry operating in non-collapsed mode," *IEEE Transactions on Ultrasonics, Ferroelectrics, and Frequency Control*, vol. 60, no. 11, pp. 2426-2439, 2013, doi: 10.1109/TUFFC.2013.6644745.
- [65] A. Boulmé and D. Certon, "Design of broadband linear micromachined ultrasonic transducer arrays by means of boundary element method coupled with normal mode theory," *IEEE Transactions on Ultrasonics, Ferroelectrics, and Frequency Control*, vol. 62, no. 9, pp. 1704-1716, 2015, doi: 10.1109/TUFFC.2015.006986.
- [66] S. Satir and F. L. Degertekin, "A nonlinear lumped model for ultrasound systems using CMUT arrays," *IEEE Transactions on Ultrasonics, Ferroelectrics, and Frequency Control*, vol. 62, no. 10, pp. 1865-1879, 2015, doi: 10.1109/TUFFC.2015.007145.
- [67] M. Hery *et al.*, "Broadband vs. Sensitive CMUT Linear Array: A Comparative Study from Bare Chip Up to Image," in *2018 IEEE International Ultrasonics Symposium (IUS)*, 22-25 Oct. 2018 2018, pp. 1-4, doi: 10.1109/ULTSYM.2018.8579976.
- [68] S.-R. Kothapalli, T.-J. Ma, S. Vaithilingam, O. Oralkan, B. T. Khuri-Yakub, and S. S. Gambhir, "Deep Tissue Photoacoustic Imaging Using a Miniaturized 2-D Capacitive Micromachined Ultrasonic Transducer Array," *IEEE TRANSACTIONS ON BIOMEDICAL ENGINEERING*, vol. 59, no. 5, 2012, doi: 10.1109/TBME.2012.2183593.
- [69] S. Lani, S. Satir, G. Gurun, K. G. Sabra, and F. Levent Degertekin, "High frequency ultrasonic imaging using thermal mechanical noise recorded on capacitive

- micromachined transducer arrays," *Applied Physics Letters*, vol. 99, no. 22, pp. 224103-224103, 2011, doi: 10.1063/1.3664775.
- [70] C. D. Arvanitis, C. Crake, N. McDannold, and G. T. Clement, "Passive Acoustic Mapping with the Angular Spectrum Method," *IEEE Transactions on Medical Imaging*, vol. 36, no. 4, pp. 983-993, 2017, doi: 10.1109/TMI.2016.2643565.
- [71] G. Gurun, M. Hochman, P. Hasler, and F. L. Degertekin, "Thermal-mechanical-noise-based CMUT characterization and sensing," *IEEE Transactions on Ultrasonics, Ferroelectrics and Frequency Control*, vol. 59, no. 6, pp. 1267-1275, 2012, doi: 10.1109/TUFFC.2012.2317.
- [72] E. M. Arase, "Mutual Radiation Impedance of Square and Rectangular Pistons in a Rigid Infinite Baffle," *The Journal of the Acoustical Society of America*, vol. 36, no. 8, pp. 1521-1525, 1964, doi: 10.1121/1.1919236.
- [73] G. Gurun, J. Zahorian, P. Hasler, and L. Degertekin, "Thermal mechanical noise based characterization of CMUTs using monolithically integrated low noise receiver electronics," in *2010 IEEE International Ultrasonics Symposium*, 11-14 Oct. 2010 2010, pp. 567-570, doi: 10.1109/ULTSYM.2010.5935987.
- [74] P. B. Dattilo, A. Prasad, E. Honeycutt, T. Y. Wang, and J. C. Messenger, "Contemporary Patterns of Fractional Flow Reserve and Intravascular Ultrasound Use Among Patients Undergoing Percutaneous Coronary Intervention in the United States," *Journal of the American College of Cardiology*, vol. 60, no. 22, p. 2337, 2012, doi: 10.1016/j.jacc.2012.08.990.
- [75] N. W. Shammass, Q. Radaideh, W. J. Shammass, G. E. Daher, R. J. Rachwan, and Y. Radaideh, "The role of precise imaging with intravascular ultrasound in coronary and peripheral interventions," (in eng), *Vasc Health Risk Manag*, vol. 15, pp. 283-290, 2019, doi: 10.2147/VHRM.S210928.
- [76] T. Xu, C. Tekes, and F. L. Degertekin, "CMUTs with high-K atomic layer deposition dielectric material insulation layer," *IEEE Transactions on Ultrasonics, Ferroelectrics, and Frequency Control*, vol. 61, no. 12, pp. 2121-2131, 2014, doi: 10.1109/TUFFC.2014.006481.
- [77] Y. Pennec and B. Djafari-Rouhani, "Fundamental Properties of Phononic Crystal," in *Phononic Crystals: Fundamentals and Applications*, A. Khelif and A. Adibi Eds. New York, NY: Springer New York, 2016, pp. 23-50.
- [78] A. Atalar, H. Köymen, and H. K. Oğuz, "Rayleigh–bloch waves in CMUT arrays," *IEEE Transactions on Ultrasonics, Ferroelectrics, and Frequency Control*, vol. 61, no. 12, pp. 2139-2148, 2014, doi: 10.1109/TUFFC.2014.006610.
- [79] S. Lani, K. G. Sabra, and F. L. Degertekin, "Modal and transient analysis of membrane acoustic metasurfaces," *Journal of Applied Physics*, vol. 117, no. 4, p. 045308, 2015, doi: 10.1063/1.4906549.

- [80] S. W. Lani, M. W. Rashid, J. Hasler, K. G. Sabra, and F. L. Degertekin, "Capacitive micromachined ultrasonic transducer arrays as tunable acoustic metamaterials," *Applied Physics Letters*, vol. 104, no. 5, p. 051914, 2014, doi: 10.1063/1.4864635.
- [81] B. Shieh, K. G. Sabra, and F. L. Degertekin, "Efficient Broadband Simulation of Fluid-Structure Coupling for Membrane-Type Acoustic Transducer Arrays Using the Multilevel Fast Multipole Algorithm," *IEEE Transactions on Ultrasonics, Ferroelectrics, and Frequency Control*, vol. 63, no. 11, pp. 1967-1979, 2016, doi: 10.1109/TUFFC.2016.2591920.
- [82] S. Satir, T. Xu, and F. L. Degertekin, "Model based drive signal optimization of CMUTs in non-collapse operation and its experimental validation," in *2013 IEEE International Ultrasonics Symposium (IUS)*, 21-25 July 2013 2013, pp. 295-298, doi: 10.1109/ULTSYM.2013.0076.
- [83] B. E. Treeby, E. Z. Zhang, A. S. Thomas, and B. T. Cox, "Measurement of the Ultrasound Attenuation and Dispersion in Whole Human Blood and its Components From 0–70 MHz," *Ultrasound in Medicine & Biology*, vol. 37, no. 2, pp. 289-300, 2011, doi: <https://doi.org/10.1016/j.ultrasmedbio.2010.10.020>.
- [84] C. Tekes, T. Xu, and F. L. Degertekin, "Investigation of dual mode side and forward looking IVUS using a dual ring CMUT-on-CMOS array," in *2012 IEEE International Ultrasonics Symposium*, 7-10 Oct. 2012 2012, pp. 1572-1575, doi: 10.1109/ULTSYM.2012.0393.
- [85] B. Bayram *et al.*, "Finite element modeling and experimental characterization of crosstalk in 1-D CMUT arrays," *IEEE Transactions on Ultrasonics, Ferroelectrics, and Frequency Control*, vol. 54, no. 2, pp. 418-430, 2007, doi: 10.1109/TUFFC.2007.256.
- [86] S. Lani, M. W. Rashid, K. G. Sabra, and F. L. Degertekin, "Investigation of slow evanescent waves at the surface of immersed micromachined membrane arrays," in *2013 IEEE International Ultrasonics Symposium (IUS)*, 21-25 July 2013 2013, pp. 717-720, doi: 10.1109/ULTSYM.2013.0185.
- [87] T. L. Christiansen, J. A. Jensen, and E. V. Thomsen, "Acoustical cross-talk in row-column addressed 2-D transducer arrays for ultrasound imaging," *Ultrasonics*, vol. 63, pp. 174-178, 2015/12/01/ 2015, doi: <https://doi.org/10.1016/j.ultras.2015.07.008>.
- [88] B. Shieh, K. G. Sabra, and F. L. Degertekin, "A Hybrid Boundary Element Model for Simulation and Optimization of Large Piezoelectric Micromachined Ultrasonic Transducer Arrays," *IEEE Transactions on Ultrasonics, Ferroelectrics, and Frequency Control*, vol. 65, no. 1, pp. 50-59, 2018, doi: 10.1109/TUFFC.2017.2772331.
- [89] S. Yoshizawa, T. Ikeda, A. Ito, R. Ota, S. Takagi, and Y. Matsumoto, "High intensity focused ultrasound lithotripsy with cavitating microbubbles," *Medical &*

Biological Engineering & Computing, vol. 47, no. 8, pp. 851-860, 2009/08/01 2009, doi: 10.1007/s11517-009-0471-y.

- [90] J. M. Stephen, F. K. Neal, G. Oded, and H. Sagi, "Transcranial MR-guided focused ultrasound sonothrombolysis in the treatment of intracerebral hemorrhage," (in English), *Neurosurgical Focus FOC*, vol. 34, no. 5, p. E14, 2013, doi: 10.3171/2013.2.FOCUS1313.
- [91] B. Rifai, C. D. Arvanitis, M. Bazan-Peregrino, and C.-C. Coussios, "Cavitation-enhanced delivery of macromolecules into an obstructed vessel," *The Journal of the Acoustical Society of America*, vol. 128, no. 5, pp. EL310-EL315, 2010/11/01 2010, doi: 10.1121/1.3496388.
- [92] C. Coviello *et al.*, "Passive acoustic mapping utilizing optimal beamforming in ultrasound therapy monitoring," *The Journal of the Acoustical Society of America*, vol. 137, no. 5, pp. 2573-2585, 2015/05/01 2015, doi: 10.1121/1.4916694.
- [93] C. D. Arvanitis and N. McDannold, "Integrated ultrasound and magnetic resonance imaging for simultaneous temperature and cavitation monitoring during focused ultrasound therapies," *Medical Physics*, vol. 40, no. 11, p. 112901, 2013/11/01 2013, doi: 10.1118/1.4823793.
- [94] J. S. Zahorian, "Fabrication technology and design for CMUTS on CMOS for IVUS catheters," Doctoral Dissertation, Electrical and Computer Engineering, Georgia Institute of Technology, 2013. [Online]. Available: <http://hdl.handle.net/1853/51730>
- [95] A. Pirouz and F. L. Degertekin, "Low Temperature CMUT Fabrication Process with Dielectric Lift-off Membrane Support for Improved Reliability," *J Micromech Microeng*, vol. 28, no. 8, Aug 2018, doi: 10.1088/1361-6439/aabe0c.
- [96] J. Lim, C. Tekes, A. Rezvanitabar, E. F. Arkan, F. L. Degertekin, and M. Ghovanloo, "Highly-integrated guidewire vascular ultrasound imaging system-on-a-chip," in *2018 IEEE Custom Integrated Circuits Conference (CICC)*, 8-11 April 2018 2018, pp. 1-4, doi: 10.1109/CICC.2018.8357032.
- [97] J. Lim, C. Tekes, E. F. Arkan, A. Rezvanitabar, F. L. Degertekin, and M. Ghovanloo, "Highly Integrated Guidewire Ultrasound Imaging System-on-a-Chip," *IEEE Journal of Solid-State Circuits*, pp. 1-14, 2020, doi: 10.1109/JSSC.2020.2967551.
- [98] J. Lim, "Reduced-wire readout systems-on-chip for high-frequency intravascular ultrasound imaging," Doctoral Dissertation, Electrical and Computer Engineering, Georgia Institute of Technology, 2017. [Online]. Available: <http://hdl.handle.net/1853/59800>
- [99] A. S. Savoia, M. La Mura, B. Mauti, N. Lamberti, and G. Caliano, "Reverberation Reduction in Capacitive Micromachined Ultrasonic Transducers (CMUTs) by

Front-face Reflectivity Minimization," *Physics Procedia*, vol. 70, pp. 941-944, 2015/01/01/ 2015, doi: <https://doi.org/10.1016/j.phpro.2015.08.195>.

- [100] M. La Mura, N. A. Lamberti, B. L. Mauti, G. Caliano, and A. S. Savoia, "Acoustic reflectivity minimization in Capacitive Micromachined Ultrasonic Transducers (CMUTs)," *Ultrasonics*, vol. 73, pp. 130-139, 2017/01/01/ 2017, doi: <https://doi.org/10.1016/j.ultras.2016.09.001>.
- [101] K. Kurokawa, "Power Waves and the Scattering Matrix," *IEEE Transactions on Microwave Theory and Techniques*, vol. 13, no. 2, pp. 194-202, 1965, doi: [10.1109/TMTT.1965.1125964](https://doi.org/10.1109/TMTT.1965.1125964).